Imaging Multi-Particle Atomic and Molecular Dynamics in Dissociative Electron Attachment to CF_4 and Double Photoionization of NH_3 Molecules

by

Richard Andrew Strom

A dissertation submitted to the Graduate Faculty of
Auburn University
in partial fulfillment of the
requirements for the Degree of
Doctor of Philosophy

Auburn, Alabama
May 1, 2021

Keywords: Dissociative Electron Attachment, Photoionization, Electron Dynamics

Approved by

Dr. Allen Landers, Professor and Chair of Physics, Experimental AMO Physics
Dr. Michael Fogle, Howard Carr Professor of Physics, Experimental AMO Physics
Dr. Joshua Williams, Affiliate Professor of Physics, Experimental AMO Physics
Dr. Stuart Loch, Professor of Physics, Theoretical AMO Physics
Dr. David Maurer, Professor of Physics, Experimental Plasma Physics

Abstract

The experimental process and scientific study of two molecular interactions is presented. The first experiment consist of the phenomenon of dissociative electron attachment, (DEA), to Carbon Tetrafluoride, CF_4, with the second experiment consisting of single Photon Double Ionization, (PDI), of Ammonia, NH_3. These two experiments, along with their respective experimental setups, calibration, analysis and results are detailed within this work.

The initial experiment, the DEA to Carbon Tetrafluoride, CF_4, is a scattering process where a free electron of low energy, typically under 20eV, collides with a molecule and is either coupled to the molecule and forms a negative ion, or is trapped in a potential minimum. These two processes are known as either *Shape*, or *Feshbach* resonances, and will be discussed in depth within this work. This experiment also works to explain the dissociation process and gives evidence of a sequential breaking of the C – F bonds through an intermediate $CF_3{}^{-*}$ electronically excited anion. This intermediate step forms near-zero energy F^- anions as confirmed by isotropic angular distributions as well the presence of a heavy $CF_3{}^-$ anion imprinted onto the F^- fragment distribution.

Following the success of the DEA experiment introduced above, a new energy source involving linearly polarized photons was used to ionize atomic molecules. In this project,

we measure the fragmentation channels following direct single Photon Double Ionization of NH_3 where two photoelectrons and two protons are measured in coincidence using Three-Dimensional imaging.The breakup process following photoionization seeks to uncover the dication electronic states that correspond to either a sequential or concerted process by calling upon theoretical reports utilizing calculations on multi-reference configuration interactions of the dication potential energy surfaces. Evidence is given that the neutral NH fragment is ro-vibrationally excited, yielding much higher internal energy. Additionally, the energies of both the cations and electrons are measured, along with angular distributions in an effort to explain the energy sharing, bond angle breaks and symmetric behavior of the Ammonia molecule.

The common denominator with these two experiments is the capture technique known as COLTRIMS, which stands for COLd Target Recoil Ion Momentum Spectroscopy. This approach provides a deep insight into the physics and chemistry of the fundamental interactions that drive the chemical process in molecular systems. The emphasis of this scientific branch is centered around low-energy dissociative electron attachment and multiple-ionization dynamics of small molecular targets. The dissociative electron attachment experiment took place at Auburn University whereas the Double Photoionization experiment was performed at the Advanced Light Source synchrotron in Berkeley, California and analyzed at Auburn University. The main goal for these experiments is to pursue the understanding of a new molecular species, building on prior work with other molecules utilizing similar techniques. This, in part with previous theoretical findings, seeks to pursue the research in this field and usher in new understanding for the scientific community.

Dedicated to my father William,

my mother Karin,

and my sister Rebekka.

"The first gulp from the glass of natural sciences will turn you into an atheist, but at the bottom of the glass God is waiting for you."

—Werner Karl Heisenberg

$Ps19:1 and Rm1:20$

Acknowledgments

There are a tremendous amount of people I must acknowledge from my high school physics teacher Mr. Derek Owens, and to my undergraduate advisor and mentor Dr. Vola Andrianarijaona, who instilled in me the passion for not only science, but research and discovery. I would also like to thank my family, both of my parents for instilling in me the proper values and morals to not only be passionately curious in science, but also to honor and glorify my Heavenly Father in the process. I would also like to give a special thanks to my older sister, Rebekka, for always being there with advice, wisdom, common sense and hard truths. I would not be where I am today without her. During the time I worked toward this thesis I met and received assistance from a variety of people in some capacity. I thank you all for your assistance, guidance and patience.

Allen Landers, for his advising and mentorship during my graduate research tenure, Joshua Williams and the entire team at the University of Nevada, Reno for supporting me through both the experiment and dissertation, Thorsten Weber and the group at the Lawrence Berkeley National Laboratory for their expertise, Michael Fogle for his advice and knowledge during the analysis, as well as those I worked with and spent time with during the writing of this dissertation: David Maurer, Stuart Loch, Guillaume Laurent, Chad Rose, David Patrick, Dylan Reedy, Averell Gatton, Kirk Larsen, Ahmed Nemer, Spenser Burrows, and Stephen Williams.

Contents

List of Figures

List of Tables

Chapter 1

Molecular Dynamics Following Dissociative Electron Attachment of CF_4, Carbon Tetrafluoride

1.1 Introduction

The main idea behind this research is the concept of dissociative electron attachment, or DEA, that comprises roughly half of this thesis. DEA is the process of a low-energy incoming free electron attaching to a molecule and causing fragmentation. This interaction produces a transient negative ion (TNI) that yields a neutral fragment and an anion, the latter we will study in depth. This process can be expressed schematically as:

$$\mathrm{AB} + \mathrm{e}^- \longrightarrow (\mathrm{AB}^-)^* \longrightarrow \mathrm{A}^- + \mathrm{B} \text{ or } \mathrm{A} + \mathrm{B}^- \tag{1.1}$$

This process is also known as a *resonance*, due to the specific nature of the attachment. There are two types of resonance, *Feshback* and *shape*, and given the ground electronic and vibrational states of our target molecule, the resonance should be of these two types. Specifically, the resonance of the target molecules should be a *single-particle Shape* resonance or a *core-excited Feshbeck* resonance. These subgenres will be discussed more in depth in the following subsections; but in generic terms, a *Feshbeck* resonance occurs when the incident electron scatters off a bonding electron in the molecule, allowing both electrons to be trapped in a bound state of the now-excited molecule. The other, *shape*, resonance is one which is not turned into a bound state and the electron is trapped due to the shape of the potential barrier. In this case, the internal state of the system remains unchanged after disintegration into fragmentation. The neutral molecule has an attractive potential with a repulsive barrier surrounding it. This combination allows for the electron to tunnel through and become bound to the molecule, which is due to the incoming electron's attractive potential and the repulsive pseudo-potential of its angular momentum as seen by the following effective potential equation:

$$V_{eff}(r) = \frac{\hbar l(l+1)}{2m_e r^2} - \frac{\alpha e^2}{2r^4} \tag{1.2}$$

When an incident electron becomes trapped in this barrier due to the molecular potential, the electron coupling occurs to the parent molecule. In the case of the molecule we are studying, CF_4, the resonance state is metastable, thus a neutral and anion fragment are produced via the interaction in one of two observable channels:

$$CF_4 + e^- \longrightarrow CF_3^- \ + \ F \tag{1.3}$$

$$CF_4 + e^- \longrightarrow CF_3 \ + \ F^- \tag{1.4}$$

During the dissociative electron attachment process electrons couple to the system via the resonances discussed above, and it is known this only occurs over specific energy ranges for the incident electron. The wave function of the incoming electron couples to the molecular system, thus driving the dissociation process. To see the *shape* resonance at play, the electron configuration of a ground state neutral Carbon is shown below:

$$\text{Carbon: } 1s^2 2s^2 2p^2 \qquad \text{Florine: } 1s^2 2s^2 2p^5 \tag{1.5}$$

Now, in order to look at the CF_4 molecule in question, the method of *Molecular Orbital Theory* is needed, which is a branch of Group Theory to describe the electronic structure with Quantum Mechanics and further analyze the symmetry of the molecule.

1.1.1 Molecular Orbital Group Theory and Point Group

When examining a molecule that does not follow a simple linear or diatomic structure that is rotationally symmetric about the central axis, a more thorough inspection of the symmetry of the molecular structure is needed. This is aided with group theory, a method that allows the experimentalist to define the electronic structure, the symmetry operations and any transitional activity. Since the bond structure of our CF_4 molecule is known, the various specific symmetry operations such as rotation, inversion, and reflection can

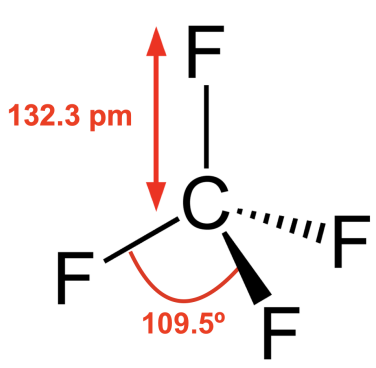

(a) Skeletal structure of the CF_4 molecule[12]

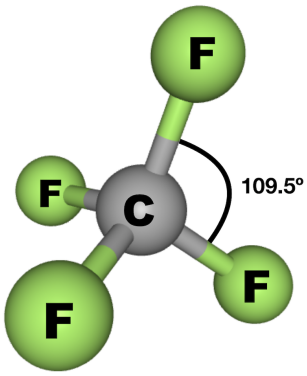

(b) Ball & Stick model of the CF_4 molecule

Figure 1.1: Some three-dimensional views of the Carbon Tetrafluoride molecule, highlighting the tetrahedral geometry as well as the terminal atom bond angles and C – F bond length.

be determined, and thus be assigned a *point group*. A point group is a specific set of symmetry processes that leave at least one point fixed and does not modify that point, thus leaving the origin unaltered and allow a place to perform these symmetry operations. The CF_4 structure follows a tetrahedral symmetry, known as T_d, which features four rotational axes. Such examples of point group operations would be a rotation through an angle as a fraction of the full 2π circle, then an angle $\frac{2\pi}{n}$, where "n" is some integer value. This is then labeled point group C_n. Next, a reflection through either the horizontal or vertical plane is known via a σ notation, with σ_h or σ_v respectively, as well as along the diagonal, σ_d . Next, a symmetry operation for an improper axis of rotation, sometimes referred to as a rotation reflection, which consists of a rotation like C_n, followed by a mirror reflection σ also exists for these types of molecules. The combination of rotation and reflection always gives the same result regardless of the order in which they are performed. This is known as S_n and use the same "n" integer as the C_n rotation, with the addition of the reflection

operation. Some other symmetry operators include an inversion *i*, where a point x, y, z becomes $-x, -y, -z$, and lastly the identity operator *E*. These operations aid in assigning symmetry groups to the molecule, and allow for referencing how atoms are arranged prior to fragmentation.

1.1.2 Molecular Structure and Symmetry of Carbon Tetrafluoride

Carbon Tetrafluoride, CF_4, follows the T_d point group along with other tetrahedral molecules such as CH_4, Methane or SiH_4 Silane. CF_4 is unique in the sense that each of the individual fluorines are indistinguishable from one another. This fact allows for several symmetry operations to be noted. Foremost, CF_4 features three C_2 axes, indicating $n = 2$, that is a π angle rotation along each axis, where each rotation is orthogonal to one another. This "natural" orientation will aid significantly during analysis in the next chapter. Secondly, four C_3 axes, indicating $n = 3$, with a $\frac{2\pi}{3}$ or 120° angle rotation along each axis, located along each of the four C – F bonds. The last symmetry operation is six mirror planes along the diagonal, σ_d. This concludes the point groups of CF_4 and aid in determining the configuration of the molecule before dissociation occurs. Shown in Figure 1.2 and Figure 1.3 is a collection of diagrams highlighting the various symmetry operators and gives a clearer picture to how CF_4 is arranged in three dimensions.

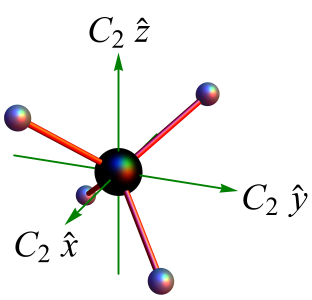

(a) C_2 axes of rotation for the CF_4 molecule

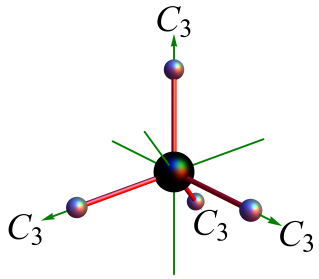

(b) C_3 axes along each terminal Fluorine atom

Figure 1.2: Point Group rotational axis views of both C_2 and C_3 for the Carbon Tetrafluoride molecule. Note the four rotations along each Fluorine as well as each x, y, z planes covering all seven indistinguishable rotations.

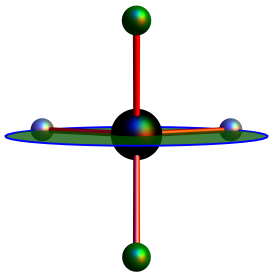

(a) A single reflection along a mirror plane, one of six possible configurations

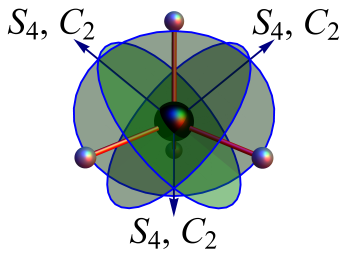

(b) CF_4's improper symmetry axes

Figure 1.3: Point Group reflection and improper axis of rotation, showing one possible reflection along Fluorine radically in sub-figure (a), with both C_3 and improper S_4 operations overlaid in sub-figure (b). These symmetric operations allow for a more complete view of the CF_4 molecule.

1.1.3 Previous Experiments of Dissociative Electron Attachment to CF_4

Now with a knowledge of the Carbon Tetrafluoride molecule and its symmetry, we can now delve into the experiment of dissociative electron attachment and previous measurements involving using this process. DEA is a scattering collision, particularly an electron-molecule collision, which invokes a conversation of kinetic energies. We seek to understand the coupling of the kinetic energy of the system, and the partitioning of the incident electron's kinetic energy into the molecular system. A collection of Theoretical Physics papers were published discussing this concept and will be referenced in this section. The earliest reports of the breakup of the CF_4 molecule comes from a paper published in 1974 by P.W. Harland and J.L. Franklin.[9] Within the scope of this paper is the kinetic energy measurements for various trigonal and tetrahedral molecules, including the CF_4 molecule studied within this portion of the thesis. The incoming kinetic energy from the incident electron is distributed along translational, vibrational, and electronic degrees of freedom in the intermediate molecular ion. Harland and Franklin deduced that this distribution of energy can vary within a specific molecule depending on which fragment traps the additional electronic charge. This is especially true in the case of our CF_4 molecule, which not only has a heavier Carbon atom in the center, but four equal terminal atoms of Fluorine that could gain the additional charge. We saw back in Equations 1.3 and 1.4 the two possible fragments following dissociation, but the pathway leading to these fragment outcomes was of interest for P.W. Harland and J.L. Franklin.[9] For the first pathway, the F^- channel as seen in Equation 1.4, there are two possible outcomes regarding energy distribution. The first, the anion F^- fragment is the result of a reaction that yields three

fragments, with two other neutrals as shown below:

$$e^- + CF_4 \longrightarrow F^- + F + CF_2 \tag{1.6}$$

Harland and Franklin deduced this triple fragment product is the result of one of two paths, citing energy requirements for each:[9]

$$CF_4 + e^- \longrightarrow {F_2}^{-*} + CF_2 \longrightarrow (F^- + F) + CF_2 \tag{1.7}$$

$$CF_4 + e^- \longrightarrow F + {CF_3}^{-*} \longrightarrow (F^- + CF_2) + F \tag{1.8}$$

Within the paper, it was determined that in order for mechanism 1.7 to occur, roughly one-third of the excess energy required is in translational energy, with the remaining two-thirds going into internal energy of the CF_3^-. This is not sufficient energy for a production of $CF_2 + F^-$; therefore, not a possible pathway for the production of the triple fragmentation. Similarly, considering the energy requirements for mechanism 1.8, it was determined that all internal energy in the second step was shy of the required internal energy for the production of F and F^-. If all the required energy went into the F_2^- term alone, the decomposition is endothermic and thus, energetically forbidden from occurring. Thus, it was determined the production of the F^- anion is formed in the second step, and yield the following reaction, with no triple fragmentation produced.

$$CF_4 + e^- \longrightarrow F^- + CF_3^* \tag{1.9}$$

Here we see the our F^- fragment, with nearly zero translational energy. This is most likely due to a resonance where all the incident electron energy goes into the vibrational degrees of freedom of the CF_3 fragment. Alas, the authors were not able to identify the electronic states of the neutral CF_3 term but determined this to be the most probable reaction for the molecule regarding low energies. This concludes the process of the first channel, referred to as the F^- channel or low energy channel in the rest of this thesis.

Table 1.1: Harland and Franklin's Resonance Energy Levels for each fragment.

Ion	**Appearance Energy (eV)**	**Resonance Energy (eV)**	$\frac{KER}{E_{electron}}$ *
F^-	4.65 ± 0.1	6.15 ± 0.1	0.40
F^- (Thermal)	6.35 ± 0.15	7.5	0.46
$CF_3{}^-$	5.4 ± 0.1	6.9 ± 0.1	0.33

*The ratio of KER to Electron Energy, ($\frac{KER}{E_{electron}}$), is often referred to as the slope "α" in literature.

The second channel, yielding the $CF_3{}^-$ fragment, is much more straightforward and results from the incident electron bounding to the heavier fragment following dissociation with a single Fluorine as the neutral term. This will be known as the $CF_3{}^-$ channel or high energy channel. Harland and Franklin then measure the kinetic energy release (E_R) of the CF_4 fragments as a function of incident electron energy (E_e) and found the slope, $\frac{dE_R}{dE_e}$, to be single valued for all values of E_e. Another paper, published in 1994 by Y. Le Coat *et al*,[3] discusses a range of energies for both channels, and specifically focuses on the DEA resonances of CF_4. Le Coat uses the symmetry point group T_d discussed in section 1.1.2, and specifically claims the two fragment channels are due to the $^2T_2$ shape resonance, with

no evidence for a $^2A_1$ shape resonance that would indicate another fragmentation pathway.

Table 1.2: Le Coat's data of anion kinetic energies for a range of incident electron energies.

Electron Energy (eV)	**F^- Fragment (eV)**	**CF_3^- Fragment (eV)**
5.0	0.648	0.138*
5.5	0.841	0.201
6.0	1.024	0.261
6.5	1.210	0.344
7.0	1.403	0.393
7.5	1.598	0.493
8.0	1.789	0.529
8.5	1.975	0.599
9.0	2.165*	0.658

*These two data points are produced via a least squares line and not experimentally measured points.

The authors also stated no evidence of any spontaneous symmetry breaking, a mechanism known as the *Jahn-Teller Effect* that has been referenced in prior publications. Harland *et al* and other early experiments by Illenberger *et al* and Scheunemann *et al*[13,25] used time-of-flight mass spectrometer configurations to measure the kinetic energy release (E_R) of the CF_4 fragments as a function of incident electron energy (E_e). This method was an effective genesis but did not allow for a full capture, thus the need for a way to capture the angular distribution of the anions. Later experiments by Le Coat *et al*[3] used a turntable style mass spectrometer and energy analyzer array to collect a portion of the angular distribution of the CF_3^- ions, from 20^o to 115^o as measured from the direction of the incident electron beam. Le Coat found $\frac{dE_R}{dE_e}$ to be single valued as well, in agreement with the

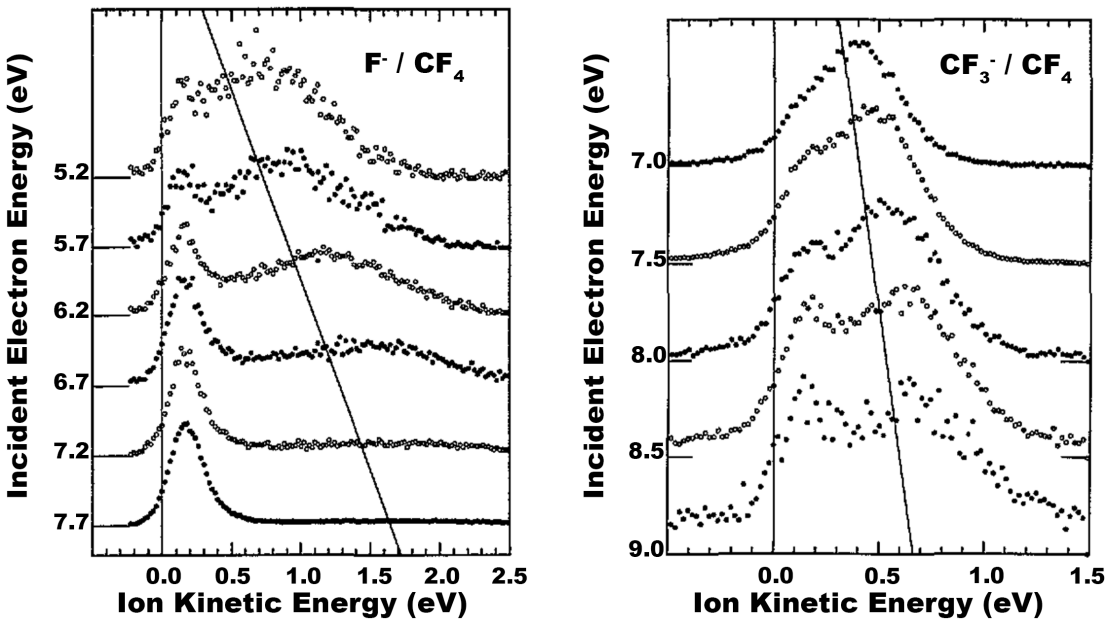

(a) Kinetic Energy Distributions of F^- Ions

(b) Kinetic Energy Distributions of $CF_3{}^-$ Ions

Figure 1.4: Kinetic energy distributions captured by Le Coat *et al* for both F^- fragments as well as $CF_3{}^-$ fragments following DEA of the CF_4 molecule at several incident electron energies. The vertical lines indicate the zero kinetic energy for comparison with the energy of the low energy ion peak; the other negatively-sloped lines is drawn through the maxima of the fast anion peaks. The observation angle is 90^o.[3]

experiments of Illenberger, Harland, and Scheunemann. Additionally, Le Coat *et al* was able to partially observe the angular distribution of the ions within the operational range of the turn-table style experiment. More recently, Xia *et al*[30] and Ómarsson *et al*[22] have used a more sensitive technique, velocity slice imaging (VSI), to collect a section of the Newton sphere normal to the incident electron beam, producing 360^o angular resolution in the place of the detector. This VSI technique offers improvement to the turn-table style like Le Coat *et al*[3] used, and improves upon the limitations of isolating a section of the

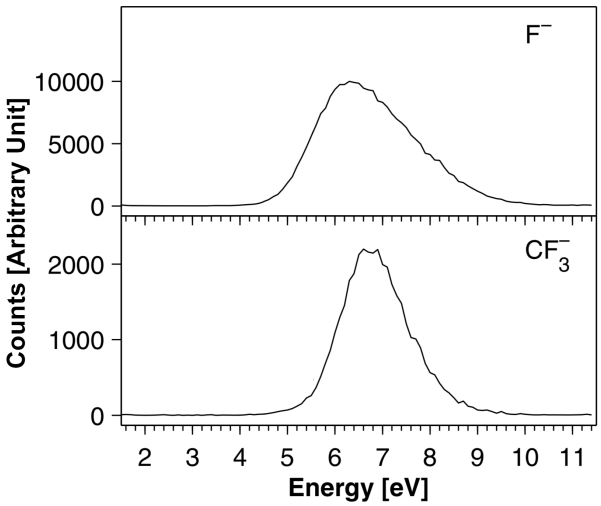

Figure 1.5: Ion fragment yield as a function of the incident electron energy as reported by Ómarsson *et al.*[22–24] The F^- fragment yield (upper) shows the existence of two, partly overlapping, resonances. These high and low KER resonance findings were partial motivation for this work.

angular distribution. In contrast with recent experiments, Ómarsson observed a distinct increase in $\frac{dE_R}{dE_e}$ near the center of the DEA resonance. It is primarily the observation of this "kink" that motivates the current experiment, to challenge the constant value of the fragment ratio throughout the energy ranges seen in prior research. We discuss these results as well as further kinetic energy studies in the following chapter for the Carbon Tetrafluoride molecule analysis.

1.2 Experimental Apparatus

Now that the reader has a clearer picture of the target species, the Carbon Tetrafluoride, now the task of how to study the dissociation is posed. In order to most accurately measure the fragment energies of CF_4, a more precise method than a turn-table style or

even a VSI was desired. The best method chosen was that of a Cold Target Recoil Ion Momentum Spectroscopy (COLTRIMS)[28,36] experimental apparatus to measure dissociative electron attachment in the Atomic and Molecular laboratory in Auburn, Alabama. The specific apparatus used for this study has been described in greater detail in an earlier publication by Moradmand *et al*,[20] but will be over-viewed for the purpose of the experiment within this thesis. The Auburn DEA experiment, in short, involves a cold supersonic molecular beam crossed by a low energy electron beam inside a spectrometer. The electron pulse is allowed to exit the interaction region, followed by a delay time during which the Newton sphere is allowed to expand. A uniform electric field is pulsed in the direction perpendicular to the plane defined by the molecular and electron beams to guide the ion fragments to a detector. The detector is both a time-sensitive and position-sensitive combination multichannel plate (MCP) and delay-line anode (DLA). Each of these components are discussed in depth in the following subsections.

1.2.1 Vacuum System

The apparatus that is utilized for the COLTRIMS technique requires a high level of vacuum to operate, both to ensure an elimination of unknown particles from the atmosphere, as well as to protect the equipment, specifically the detectors, from any damage. To achieve this, a variety of vacuum pumps, broken into four regions, are in place to keep the chamber pumped down during the experiment. Each region features its own dedicated turbomolecular pump, all of which are networked to three roughing pumps. The roughing pumps begin the initially pre-pump down from the atmosphere to roughly a Torr, to a point where the turbos take over primary pumping duty. The vacuum system, seen in Figure 1.7

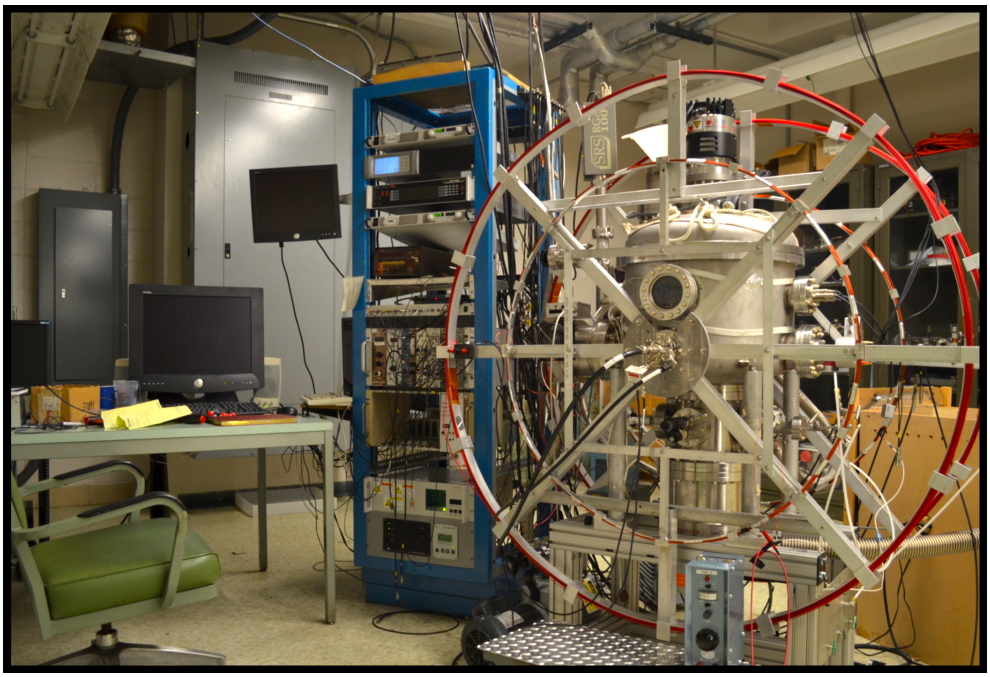

Figure 1.6: Photograph of the experiment. Seen from the left is the data acquisition workstation with analysis computer. In the center is the electronics rack, including pump and gauge controllers, power supplies, and logic modules for signal processing. On the right is the vacuum chamber including the spectrometer, gas jet, electron gun and Helmholtz coils (external).[38]

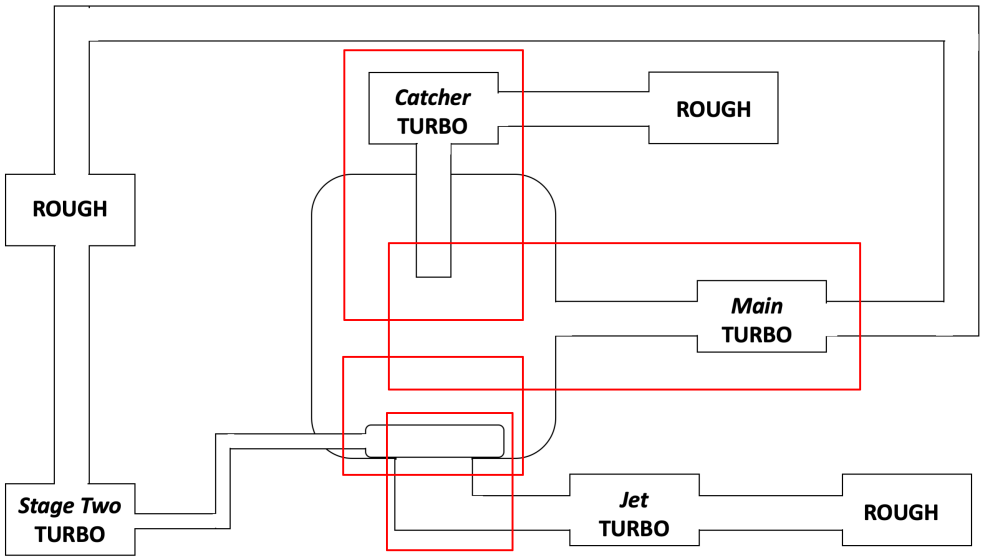

Figure 1.7: Each of the four regions, highlighted in red, feature a turbo pump, whilst the main chamber and second state, which sees minimal usage, sharing a roughing pump. Each region can be opened independently to protect vacuum during short repairs.

features a Pfeiffer Model TMH 521 for the main chamber, with a flow rate of $520\,\mathrm{L/s}$ capable of achieving a consistent vacuum of 5×10^{-8} Torr, and can increase closer to 10^{-9} Torr with the addition of a liquid nitrogen cold trap. Within the jet region, we are using a Pfeiffer Model TMU 1600 C, with a much higher flow rate of $1500\,\mathrm{L/s}$, capable of vacuums up to 10^{-8} Torr without the jet, and around 10^{-5} Torr with the jet. Before and after a data acquisition run, the gas line leading to the jet aperture, discuss in depth in Section 1.2.3 is pumped out to insure against target contamination and virtual leaks resulting from trapped gas in the jet region.[38] Lastly, a Leybold Model Turbovac TW 300 H turbomolecular pump flowing at $240\,\mathrm{L/s}$ is utilized in the catcher to keep the pressure in the detector region close to its base pressure during jet operation.

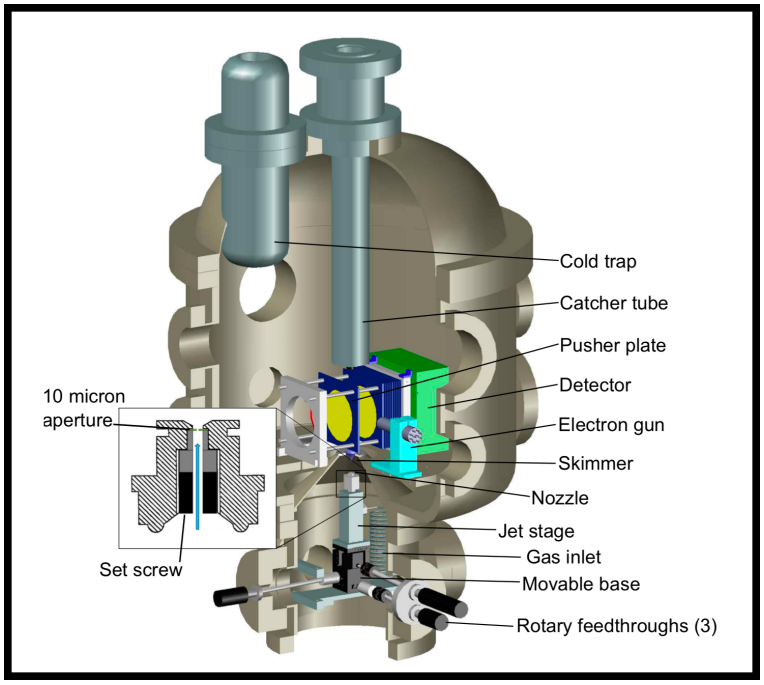

Figure 1.8: Cutaway of the experimental apparatus. The chamber bottom separates the jet region from the main chamber above, which houses the spectrometer and electron gun. A gas inlet feeds into the jet stage, which is movable in three dimensions by three rotary adjustment screws. The jet aperture is housed in a screw-on Swagelok VCR fitting situated atop the jet stage, and the skimmer sits directly above it. The electron-molecule interaction occurs in-between the two spectrometer plates near the center of the figure.

1.2.2 Electron Gun Source

The apparatus setup here, COLTRIMS, relies on a source to produce the free electrons needed to study Dissociative Electron Attachment (DEA), the specific type of electron-driven process that this thesis is based upon. For the data and molecules studied in the following chapter, a commercial unit from Kimball Physics was utilized. A model ELG-2 gun was put into place allowing us to produce an electron beam of narrow, collimated electrons with a precise kinetic energy down to a few eV. This is seen in Fig. 1.9. for a

typical electron gun design, highlighting the ability to "focus" the beam using a charged plate. Despite the technological advances within production of commercial electron guns, issues still arise with optimizing the pulse width of the electron beam to both maintain high time resolution as well as increased current for high fragment production. This chapter will discuss some of these challenges and explain the methods used to produce and capture these fragments following the DEA process. The electron gun is mounted on a six-inch flange into the chamber side, with the gun head inside, with data and power wires exiting via a custom 18-pin feedthrough for connection to the Kimball Physics power supply and pulse controller. The gun head features a tantalum disc cathode filament that undergoes thermionic emission after receiving low amounts of voltage in the range of 1.1 V to 1.6 V. In addition to the emitter itself, the gun head has an anode plate to accelerate the electrons away from the filament, as well as a negatively-biased grid, which suppresses the electrons from being emitted from the head of the gun and is pulsed up to 0 V, allowing for a pulsed beam of electrons of controllable width in time. This grid's primary function is to control the release of the electrons, and interrupt the stream of continuous electrons. This is needed so that free electrons are not in the interaction region during the time the electric field is turned on, thus to avoid the electrons being accelerated toward the detector by the pulses of the spectrometer itself and reflected off the surfaces within the chamber, which will produce unaccounted signals on the detector, that is, false and undesirable signals. This is why a pulsed scheme is needed, to limit the electron beam to only when the electric field is turned off. The electron bunches can be pulsed with a width as short as 30 ns, while the usual operating bunch width is around 100 ns. This bunch mark initiates the beginning of the time of flight (*TOF*) measurement in the experiment and interactions can occur from

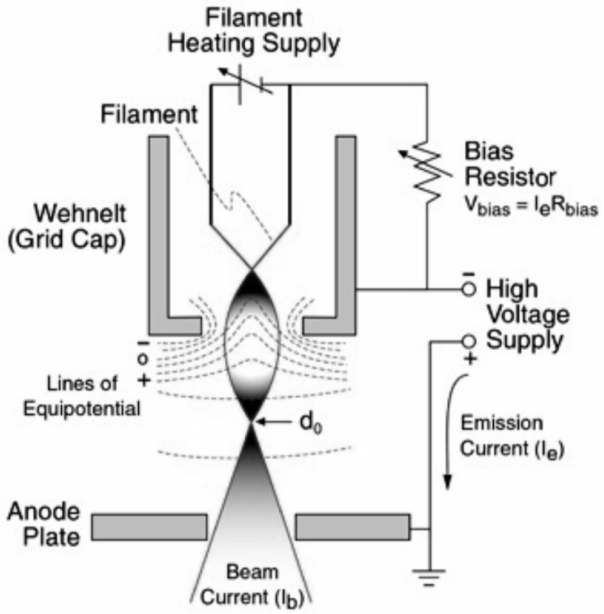

Figure 1.9: This is a typical design of an electron gun. Once a voltage is applied across a cathode, causing it to heat to over 1000 K and thermally emit the electrons which are focused by a cylindrical electrode and extracted by an anode plate to form a collimated beam.[6]

electrons anywhere within that bunch, so in order to ensure a high momentum resolution we limit the width to a relatively short acquisition times. Lastly, to ensure we have a properly calibrated electron gun, the energy was measured by locating the cross-sectional area (σ) of the known resonance of O^-, the negative fragments of O_2, as a function of the incoming electron energy.[37]

1.2.3 Gas Jet

In an effort to localize the interaction region within the chamber, a supersonic jet is utilized to confine the target spatially within a region we can control with the electric and magnetic fields, as well as to reduce the initial kinetic energy of the incoming molecules of CF_4. The species source with a gauge pressure of $\sim$ $25\,\mathrm{psi}$ enters into the gas manifold, which sends the gas column through a $10\,\mu\mathrm{m}$ aperture. Once the gas exits the aperture, a commercially acquired skimmer manufactured by Beam Dynamics which features a $0.3\,\mathrm{mm}$ exit hole to capture the center of the distribution and allows for a low energetic, cold gas stream to enter into the spectrometer region. Molecules from the column of gas that do not interact with the spectrometer pass through into a catcher tube, ensuring the interaction region is unaffected. The aperture itself, seen in Figure 1.11 is mounted on a pedestal that sits atop three translatable optical stages that can be controlled by rotary feedthroughs. This allows for the jet aperture to move in three dimensions in reference to the skimmer, ensuring any minor misalignment during assembly can be quickly remedied whilst under vacuum. Additionally, these optical stages allow for distance adjustments to the skimmer, ensuring that the skimmer can always in the overexpanded zone of the jet's silence region, that is, where no background gas is present to interfere with the interaction. Lastly, the aperture is mounted on a commercially available Swagelok seal fitting, outfitted for an electron microscope, and secured with a set screw. This style ensures a solid mount for the jet under vacuum and gas pressure, with the ability to quickly modify and upgrade the aperture once vented. Aligning the jet via the aperture is mainly done in the x and y axis, with the z axis determined by the size of the nozzle, and only adjusted during

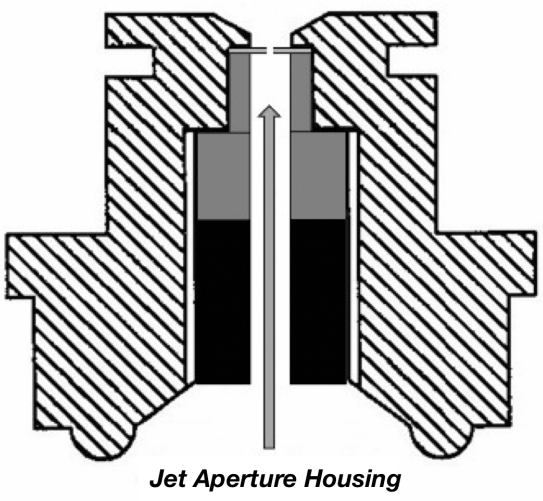

Figure 1.10: This is a diagram of the aperture housing, featuring the stream of CF_4 molecules entering up vertically, and through the $10\,\mu\mathrm{m}$ slit on top. This mounts to the three dimensional optical stages for alignment.

install of the aperture housing. To align the coplanar values, we use two different diagnostic criteria, the catcher pressure, as well as the partial pressure of the test gas, viewed using a residual gas analyzer (RGA) model RGA100 manufactured by Stanford Research Systems. We additionally use the RGA to test for contamination by high-mass species, such as water vapor from the ambient air or hydrocarbons present within the chamber. Monitoring a rise in catcher pressure to a maximum value ensures we have an aligned jet, whereas if it is unaligned, extraneous gas will leak past into the surrounding chamber area, and eventually hit on the RGA as a mass value relating to the CF_4 atomic weight of $\sim 88\,\mathrm{g\,mol^{-1}}$. Therefore, it is ideal to maximize the catcher pressure output and minimize the RGA partial pressure to guarantee the best positioning for the nozzle relative to the skimmer.

1.2.4 Magnetic Field

A magnetic field is produced to move the anions after the collision, and is done via a pair of concentric Helmholtz coils. We use two vertical coils, thus to produce a magnetic field along the horizontal direction, perpendicular to the gas jet so the ionized fragments move together in a helical trajectory and remain confided towards the anion detector. This uniformed field is generated via 132 turns of 14 gauge wire that carry $\sim$ 6 A of current via the following equation:

$$B = \left(\frac{4}{5}\right)^{\frac{2}{3}} \frac{\mu_0 N I}{R} \tag{1.10}$$

Where *R* is our radius of $0.75\,\mathrm{m}$, *N* our 132 turns of wire, and the current *I* is variable by a TKD-Lambda GEN100-7.5 power supply, allowing to adjust the field strength as deemed from the simulations, discussed in the following section. For the CF_4 molecule at the studied energies the B Field contribution from these coils is $\sim$ 10 G. To increase the field strength at the interaction region, a secondary pair of coils were added, with a radius of $0.51\,\mathrm{m}$, and running a current of $\sim$ 5.1 A. This coupled with the field of the outer coils yields a usable field strength of $\sim$ 25 G. The field is primarily used to collimate the electron beam and to control any stray electrons. In principle, the path of any negativity charged fragment will be affected-not just the stray electrons-so we need to calculate the cyclotron frequency that the B field produced:

$$T = \frac{2\pi m}{Bq} \tag{1.11}$$

Where *B* is the magnetic field of both coils, *q* the fundamental charge of the anion, and *m* the atomic mass. Using a field strength of $\sim$ 25 G, for both anion fragments of

Figure 1.11: A view of the pair of Helmholtz coils on the COLTRIMS apparatus, in black. These are mounted to the camber roughly coaxial to the electron beam via an aluminum structure mounted to the electron gun feedthrough. The smaller coils (not pictured) mount to the same frame within the outer coils seen here.

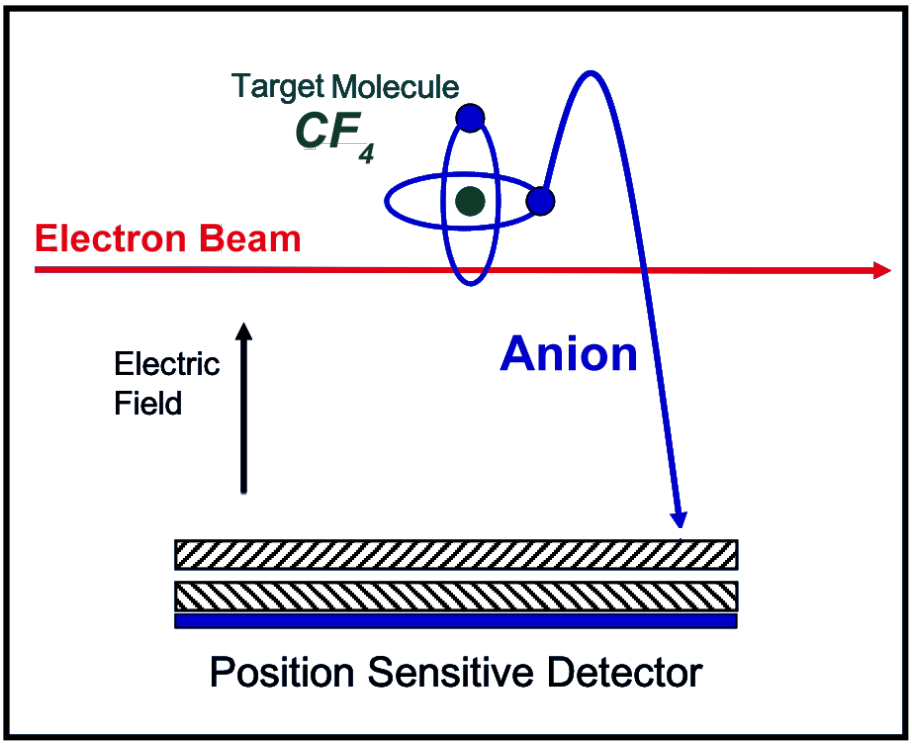

Figure 1.12: A simplistic diagram of the COLTRIMS apparatus with a single position sensitive detector setup. Free electrons are generated via an Electron Gun producing the horizontal beam (red). A static electric field within the interaction region (black) points opposite the anions to direct the fragments towards the MCP detector.

CF_4: CF_3^- and F^-, we can calculate their inverse gyrofrequencies to be $\sim 1800\,\mu s$ and $\sim 500\,\mu s$ respectively. These values far exceed the typical flight times of the fragments to the detector, under $10\,\mu s$ so the effects from the field can be regarded as negligible.

1.2.5 Spectrometer and Timing

The spectrometer used in the DEA CF_4 experiment is configured to specifically measure anions, without the production of electrons or positive ions, like in photoionization, which will be discussed a later chapter. To cater to this specific type of measurement, the spectrometer must be configured for an electron as the incident reaction particle. This is accomplished with both an electric field region of $40\,mm$, as well as a $142\,mm$ region to allow the parties to expand to the full area of the detector, see Figure 1.13. We define the coordinates of the spectrometer as the incoming electron beam in the x axis, the gas molecule jet is in the y axis, leaving the z axis coaxial with the spectrometer. This allows the dissociated fragments to travel along "z", which we refer to as the "t" axis, for the time-of-flight direction. Most notation throughout will refer to this direction as the "t" axis. The spectrometer itself consists of several parallel plates with $80\,mm$ holes that allow for the anions to pass through. These plates represent a somewhat capacitor-style geometry and can be modeled as such. Each is biased at either a negative voltage or ground, to accelerate the anions towards the detectors, with a field-free drift region at the end, allowing the particles to reach the detector without an external force. The main component of the spectrometer is the detector itself, a commercially available microchannel plate (MCP) setup from RoentDek - Handels GmbH (RoentDek). The MCP setup for the DEA experiment is a chevron style, consisting of two $80\,mm$ diameter detectors capable of electron multiplier

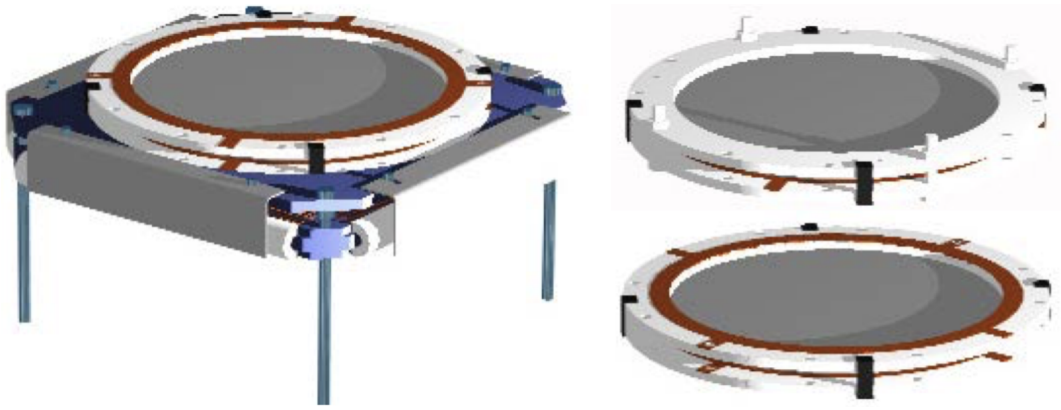

Figure 1.13: Assembly of the two microchannel plates (MCP's) with the delay-line anode detector. The MCP's attach to the grid via non-conductive ceramic clips to allow for a floating voltage difference on each plate. This is the detector housing for the experiment and sits vertically along four ceramic rods.[20]

gain on the order of 10^4 - 10^7. Each MCP features a 8° biased channels of diameter $25\,\mu\mathrm{m}$. When an anion is incident on the front of the MCP stack, a large emission of electrons are produced on the back MCP, leading to a cascade of electron-producing current that triggers a signal on the delay-line anode (DLA), another product from Roentdek, model DLD80. The DLA consists of copper wires wrapped in a helical fashion in each direction, both horizontal "*x*" and vertical "*y*" that then detects a pulse and propagates down the length of the wire to the delay-line detector. This allows for not only arrival time information, but position data as well, using software to calculate the exact position on the MCP depending on time discrepancies within the "*x*" and "*y*" DLA signals. More on the DLA process and other fast electronics is discussed in the next section. The MCP detectors in use are known as "chevron" style due to the V shaped angle that one detector makes with the other, with each channel opposing of the other. This forms the specific shape utilized for this type of experiment.

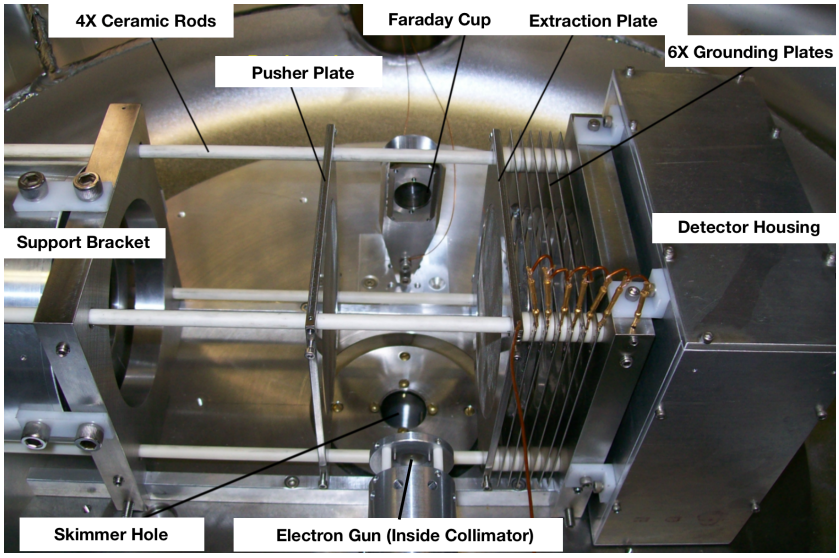

Figure 1.14: Photograph of the spectrometer housing assembly within the vacuum chamber. The left-to-right orientation towards the detector is our *TOF* direction, with the electron gun laying perpendicular (bottom of image), as well as gas jet aperture mounted into page (center of image.)

A large voltage difference of $\sim 2200\,\mathrm{V}$ is maintained between the plates, with the high potential on the back plate, and a large resister ($3.7\,\mathrm{M\Omega}$) on the front plate to ground in order to accelerate the electrons toward the back of the MCP. This continues until cascading electrons leave the channel and strike the back plate, allowing for the amplification of up to 10^7 for a single incident anion, enough for detection via the delay-line anode detector. The DLA detector has the potential to achieve a capture rate of up to $1\,\mathrm{MHz}$, but for this experiment, detection rates are well under $500\,\mathrm{Hz}$. For our specific molecule of CF_4 we capture at roughly $300\,\mathrm{Hz}$. Given a typical value of the pulsing magnitude of the spectrometer of $70\,\mathrm{V}$, and the length of the acceleration region at $40\,\mathrm{mm}$, we have an electric field strength of roughly $18\,\frac{\mathrm{V}}{\mathrm{cm}}$. In order to calculate other field parameters as well as a pulsing scheme, we call upon a highly-regarded commercial simulation software, SIMION, that

calculates electric fields and models the trajectories of charged particles, given a specified energy, voltage and other initial conditions for the particle. SIMION achieves this by solving a boundary value problem of a specific differential equation, known as Laplace's Equation, shown below in cylindrical coordinates:

$$\nabla^2\phi = \frac{1}{r}\frac{\partial}{\partial r}\left(r\frac{\partial\phi}{\partial r}\right) + \frac{1}{r^2}\frac{\partial^2\phi}{\partial\theta^2} + \frac{\partial^2\phi}{\partial z^2} \tag{1.12}$$

The software begins by finding the electric field values, needed to set on our pulsing plates in the spectrometer. Once this is achieved, the trajectory of the anions within these fields can be modeled by finding the forces felt by the anions in three dimensions, and through numerical integration, the subsequent velocity and position information. This allows for the modeling of the fragment's paths en route to the detector, and helps aid in how the fragments move along the *xy*-plane while traversing along the *TOF* direction. This is especially important to allow for even spread across the detector, which minimizes false events, as well as restricting the Newton sphere from over-expanding, and clipping past the detector. See Figure 2.2 for a visual representation on the Newton sphere expanding via simulation. This term is in reference to the anion fragments being released and traveling as a "sphere" rather than a "mass," as they are no longer bounded and can move freely, invoking a Coulomb repulsion in the presence of an electric field. This is a term we will use throughout this thesis when referring to the cluster of anion fragments moving towards the detector. From this simulation information we can form the pulse scheme needed to allow a free path for the post collision fragments.

1.2.6 Signals and Data Acquisition

The incident particle in the experiment, an electron, responds to electric fields within the spectrometer. To ensure this does not disrupt the travel of the fragments, the electron gun is pulsed with a duration of $50\,\mathrm{ns}$, followed by a fixed delay of $1\,\mu\mathrm{s}$ of the electric field to allow the Newton sphere to expand. Lastly, a positive potential of $+70\,\mathrm{V}$ is applied to the left grid of the generating field, this ensures the fragments stay within the region after the initial pulse and allows for the energy impacted from the field to be calculated during the next chapter. The data signals leave the spectrometer in five pulses, a pair for each

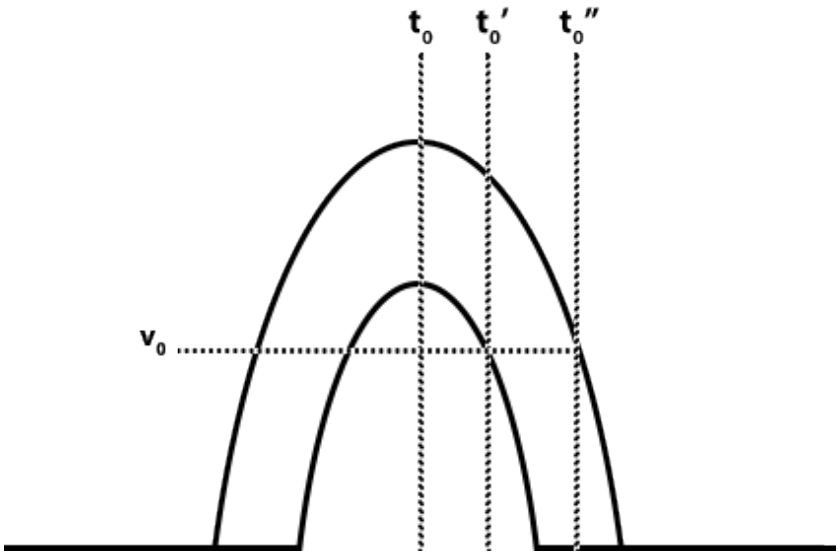

Figure 1.15: The TDC triggers on threshold, yielding a time difference if the pulse height varies, despite pulses arriving simultaneously. The CFD solves this by normalizing the pulse, allowing the TDC to trigger a pulse when it reaches a fraction of its total height.

axis, both *x* and *y*, and then a pulse from the MCP itself. These pulses are quite small, so amplification is needed via fast electronics. The four position pulses from the DLA exit through a feedthrough manufactured by RoentDek in pairs, each within shielded Ethernet

cables to a constant fraction discriminator (CFD). A constant fraction discriminator utilizes electronic comparisons followed by a logic AND gate to trigger a pulse based on a fraction of the original amplitude, rather than just relying on the time of signal arrival. The CFD we use is a commercially available Phillips 715 model that begins taking in an analog pulse, and splitting into two pulses. The second pulse is then inverted, delayed a fixed amount, and recombined with the first. See Figure 1.16 for a diagram of the process. This

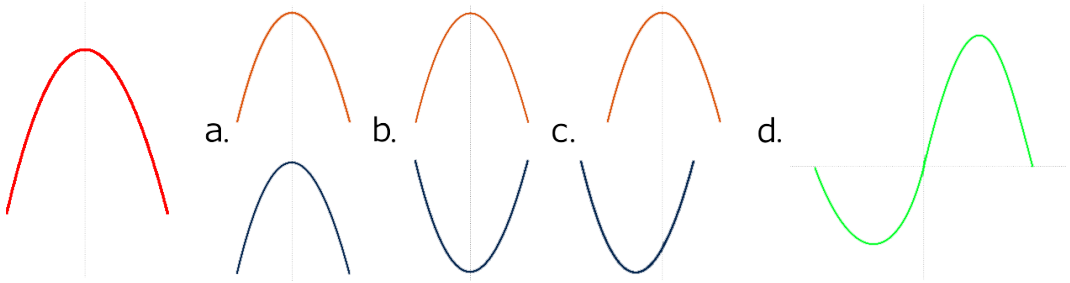

Figure 1.16: The Constant Fraction Discriminator operates by taking a pulse, (red), then (a) splitting the pulse, (b) inverting one of the pulses, (c) delaying one of the pulses, (d) recombining the pulses (green.)

creates a wave packet that is semi-sinusoidal, crossing at zero that is independent of the original pulse amplitude. This solves the dilemma of having pulses with varying heights, and normalizing the time discrepancy seen in Figure 1.15 that goes along with varying amplitudes. This resolved pulse is then sent on to a time-to-digital converter (TDC) in the acquisition computer. Now, the TDC sees normalized pulses with no time resolution issues, thus minimizing noise and maximizing good events.

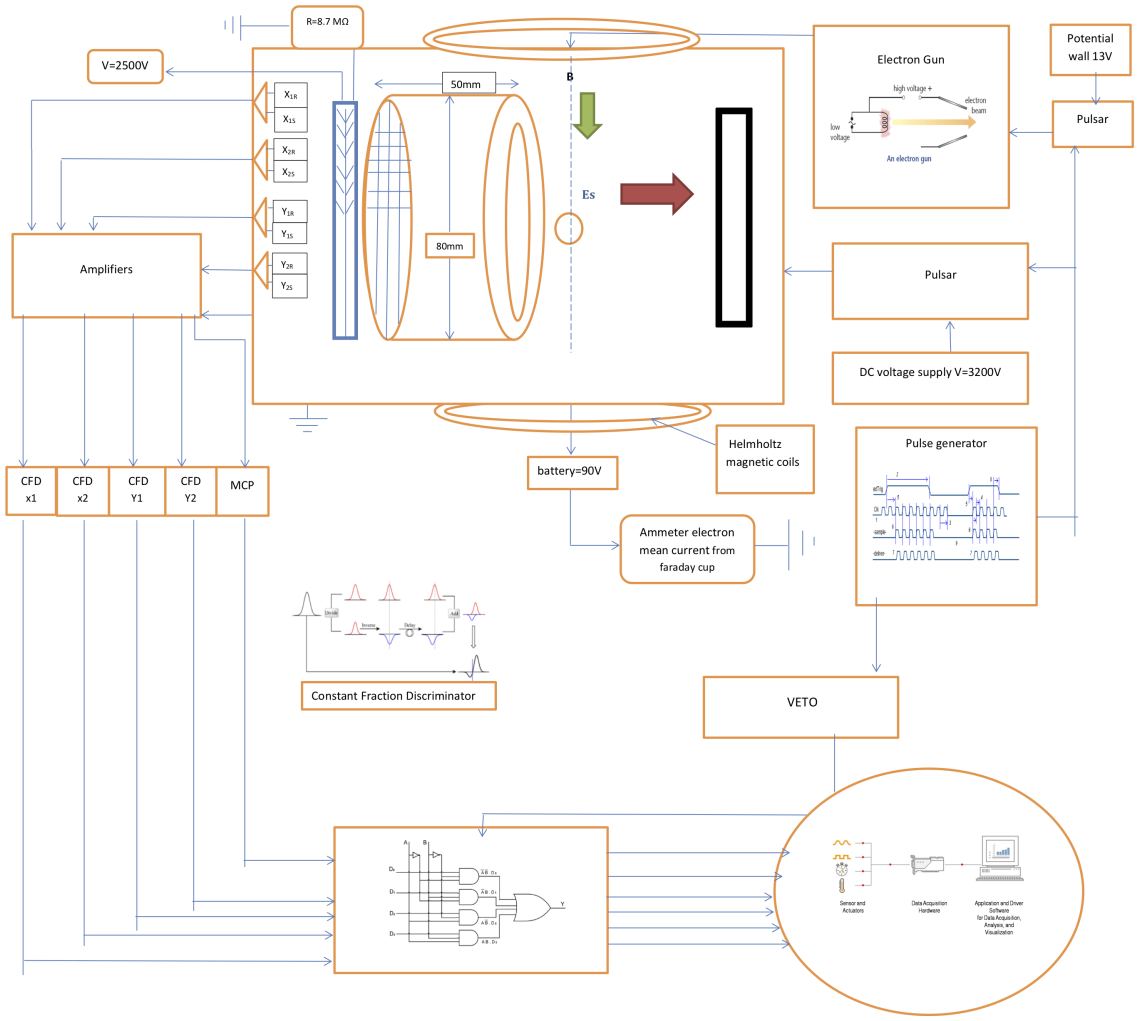

Figure 1.17: Block diagram of the COLTRIMS electronics setup. In addition to the electric and magnetic fields, a collection of fast electronics are used for acquisition and pulse generation as shown here. Pulse scheme and timing is discussed in Section **??**

Chapter 2

CF_4 Simulation and Analysis

2.1 Introduction

The Carbon Tetrafluoride molecule requires careful and precise attention during simulation, calibration and analysis to ensure results are both clear and accurate. The CF_4 molecule during DEA produces a singly charged anion, known as the negative fragment, that we will study. This is either a CF_3^- anion or F^- anion as discussed in the previous chapter. These channels will be the results garnished from the DEA process, and analyzed across a range of incident electron energy. The output from the previous section can be best described as a collection of time values, or timing signatures as they are known. These "hits" can be converted into useful physical quantities such as fragment position, time of flight, time delay and input/out detector coincidence using software analysis. From this basic values we can use both classical and quantum physics to generate additional quantities, such as energy, momentum, angular distribution and electronic dynamics in molecular

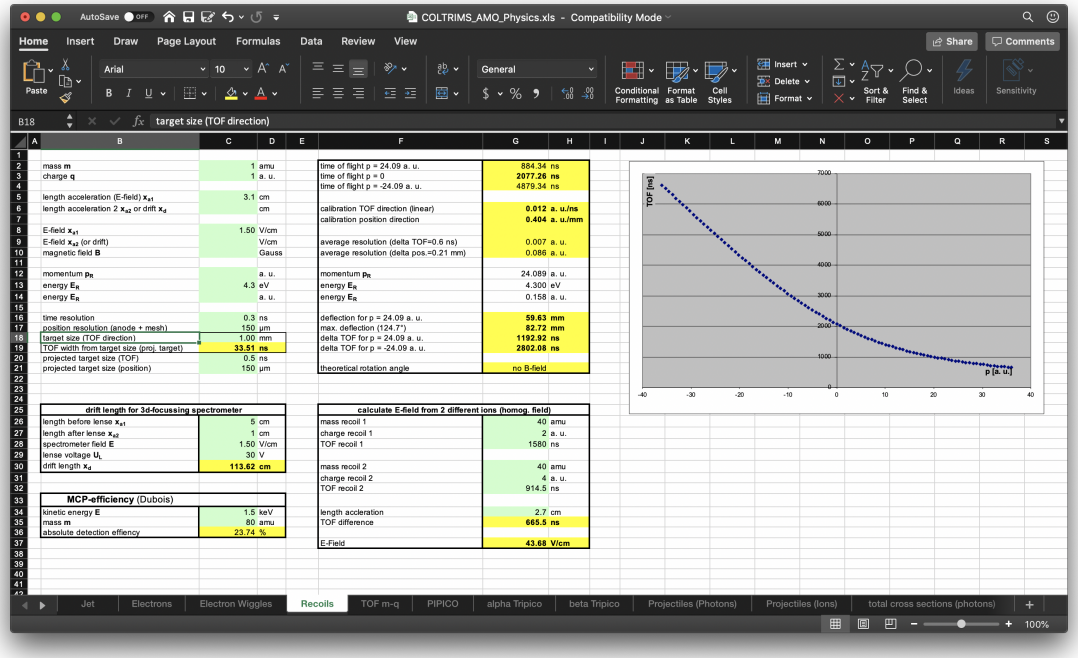

Figure 2.1: A view of the custom spreadsheet designed to coarsely calculate ion time of flight and electric field parameters for a given molecule input.

frame that aid in discovering molecular statistics. These results, and the process leading to producing these results, will be the primary subject of this chapter and hope to highlight some never before seen information on the CF_4 molecule that can be used for future experiments. The analysis portion of any experimental is typically the most strenuous and time consuming portion, but the most rewarding in being able to uncover the intertwined motion of electrons inside unperturbed atoms and molecular systems, and to see the molecules illuminated from within.

2.2 Particle Simulation

The task of discovering which parameters are required for the CF_4 molecule is a tedious one and requires a plethora of simulation and calculation. Determining correct parameters vary with the ion's kinetic energy, mass, time of flight, pulsing time scheme and target size. Each parameter must be set for that specific particle, and what works for a certain fragment may not work for another. To determine how to tune for this, we use a variety of simulation software, beginning with Excel, part of the Microsoft Office suite, and SIMION, an ion-optics simulation software package briefly discussed in section 1.14 that calculates electric fields and trajectories of charged particles by solving boundary value problems in three dimensions. It is here we can discover the necessary configuration that produces a viable flight path for the particles. It is very possible that *no* configuration works for the given spectrometer orientation, and the geometry of the spectrometer must be physically changed, requiring a time consuming job breaking vacuum and modifying the spectrometer arrangement. This method of spending a few minutes of trial and error simulating, rather than several hours or days tearing down the chamber for a guessing approach, is of great importance for efficient research.

Excel is first used to perform ion flight times and positions. This is done via a custom spreadsheet, developed by a former Auburn AMO researcher, and calculates the electric field given molecule parameters, as well as the resulting force every $0.5\,\mathrm{ns}$ via classical physics. This gives a mapping of the particles in flight to give a rough idea of the trajectory en route to the detector. The spreadsheet ignores a full three-dimensional environment and works with a basic geometry of the spectrometer to allow for a general direction for

the next step in the simulation process, using the superior simulation properties within SIMION.

SIMION is then used to create a simulated spectrometer environment, accurately scaled to our physical spectrometer within the chamber. The particular simulation environment was created previously by a former Auburn AMO student that was the basis for the CF_4 simulation, possessing the same basic geometry. This configuration was used to simulate the time of flight (*TOF*) z-axis for the CF_3^- and F^- fragment anions. It is here that we can both ensure the particles reach the detector unaltered by the external forces, that is no external force to accelerate the particle, as well as ensure a maximum spread for the detector is utilized. This simulation, unlike with the coarse tools provided by Excel does take into account the full three-dimensions, and allow for each component of the spectrometer to be included: the extraction plate and pusher plates, drift region, grounded mount for the detector, electron gun frontal face as well as the Faraday cup and catcher tube. All of these metallic objects effect the particle flight, either by charged positively or negatively, or by being grounded conductors. As briefly touched on within the last chapter, SIMION solves Laplace's equations given these entries as potential surfaces, or bounded values for the differential equation. All of this results in a flight path for the particles, broken into time steps usually of the order of 1. Smooth, concentric circles as the Newton sphere expands post-interaction are achieved in a good simulation, see Figure 2.2a. An incorrect pulsing scheme can allow for not enough delay in the pulsed electric field, which in turn keeps the particles from spreading out and bunch up non-uniformly, causing erroneous hits on the detector. A quick determination of this phenomenon occurring is when the Newton sphere is inverted along its leading edge, see Figure 2.2b, which

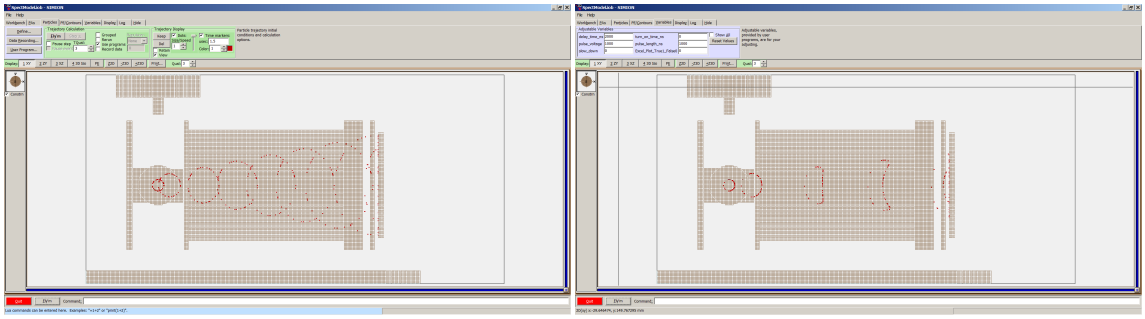

(a) An adequate simulation of the CF_3 anion flight path, with even expansion of the Newton sphere

(b) An ineffective simulation path of the CF_3 anion, with an inversion of the Newton sphere's leading edge.

Figure 2.2: An example of the simulations produced from SIMION. Sub-figure (a) highlights a successful simulated flight path, with a $1\mu s$ time difference between rings. (b) displays an inadequate simulated path, with particles stalling in the center and increasing the *TOF*.

will have hits restricted, lengthening the *TOF*. Once a smooth simulation is acquired, the spectrometer pulse settings determined by the sim are then set into place via the Stanford Research DG535 pulse generator to ensure particles arrive at the detector for capture. This is repeated again during the calibration phase, after capturing a small portion of events, the SIMION simulation is compared to results in the actual experiment for accuracy and improvement. The calibration of the spectrometer involves looking at the *TOF* direction, deemed the *t*-axis, which is along the *z*-axis along the chamber, leaving the *x,y* plane as the face of the detector, and will be used for position information in the coming sections. Finally, the *TOF* is then used to calculate the subsequent momentum for the given anion, explained below.

2.2.1 Calibrations

In order to calculate the momentum we must see how the the electric field applied following the interaction comes into play. This electric field has a force on the anions, driving them into the detector and is given by the Coulomb force equation:

$$\vec{F} = q\vec{E} \tag{2.1}$$

This force can be related to the momentum via it's time derivative:

$$\vec{F} = \frac{dp}{dt} \tag{2.2}$$

Thus, we can now take the appropriate integral to find the change in momentum along the physical z axis, or "time" t axis as it is known:

$$\Delta\vec{p_t} = p_{t_f} - p_{t_i} = \int_0^t \vec{F}dt = \int_0^t q\vec{E}dt \tag{2.3}$$

Now we can reduce this integral, given that the electric field is constant throughout the interaction region, it is then time independent, thus the force is constant. Additionally, with our precise spectrometer orientation, the initial momentum, p_{t_i}, is equal to zero:

$$p_f = \Delta\vec{p} = q\vec{E}\Delta t_{field} \tag{2.4}$$

Where Δt_{field} is the time the field is on, or the pulse "width" of the field. This value is known from the simulation and fed into the pulse generator for the spectrometer. Via

classical physics we can relate the velocity to the pulsed electric field:

$$\vec{p_t} = m\vec{v_t} = q\vec{E}\Delta t_{field} \tag{2.5}$$

Here, v_i, is the initial velocity of the negative fragment following the electric field force applied in the interaction region. Now we can calculate one of the main recorded parameters, the *TOF*, or time of flight of the particle. The *TOF* is the time of the particle once the electric field pulse is off, and the fragments drift towards the detector. This is measured from the time the spectrometer pulse is turned off, until the particle "hits" the detector and is recorded. This time is easily calculated given the known initial velocity as the rate of change of position with respect to velocity:

$$TOF = \frac{\Delta x_t}{v_t} \tag{2.6}$$

Δx_t is the length the particles move along the field-free drift region, their position on the physical z axis we call the time axis, and v_t is the velocity derived above, which is constant along the drift region negating the effects of gravity, this will come into play later with delay adjustments. Finally we can relate Eq: 2.5 and Eq: 2.6 to see the impact the negative fragment has on the *TOF*:

$$TOF = \frac{\Delta x_t}{v_t} = \frac{m\Delta x_t}{q\vec{E}\Delta t_{field}} = \frac{\Delta x_t}{\vec{E}\Delta t_{field}}\left(\frac{m}{q}\right) \tag{2.7}$$

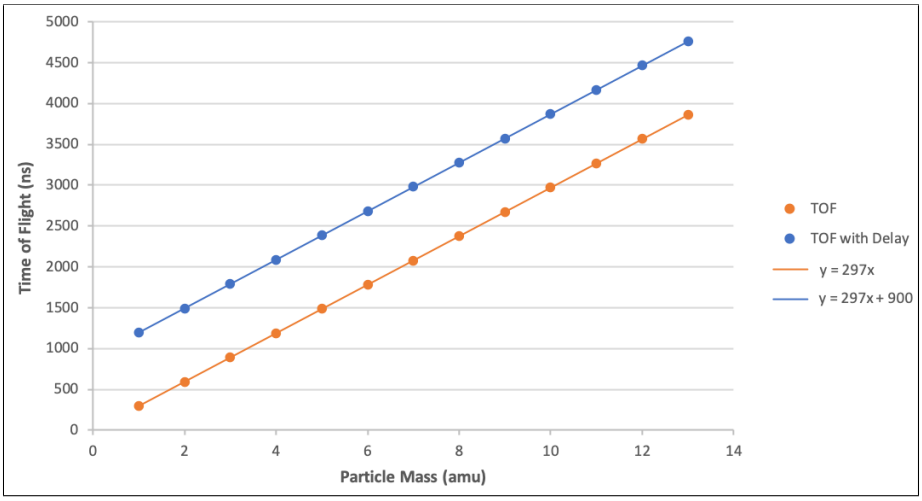

Figure 2.3: *TOF* vs mass plot, with the pulse delay to the spectrometer moving the *y* values upwards, but maintaining the same slope, ensuring a fixed delay throughout a given mass range.

Here we see the *TOF* is directly related to the mass-to-charge ratio. More on this calculation can be seen in the photoionization chapters, see Chapter 3. For a DEA experiment with a fixed single negative charge, the time of flight scales linearly with the particle's mass. A fact that aids in being able to scale delays between theoretical calculations and experimental values recorded.

Given the array of cables between the pulse generator to the spectrometer, as well as the cabling from the MCP detector back to the acquisition machine, we can expect some finite delay, albeit constant, for every particle. This delay can be calculated as a shift via the spreadsheet, as shown in Figure 2.3. To achieve these results, we first look at the *TOF* values experimentally with some known masses, H_2, He, N_2 and O_2 to name a few. Once the values are plotted, we then return to SIMION to adjust field and drift parameters to match the slope seen experimentally. This accomplishes two things, first ensures the

particles are not being "accelerated" towards the detector by outside forces and allowed to drift as designed, and secondly ensure we maintain a linear relationship to adjust for the line delay in controlling the pulse. Once the slope is matched, the task of adjusting the recorded *TOF* values with a shift, is accomplished in the acquisition software, known as CoboldPC 2011.[11]

2.2.2 Acquisition

The *TOF* value is just one of many parameters measured following the interaction. The output from the MCP detector is of equal importance in discovering the fragment's properties. The bridge between raw signals and our acquisition software, CoboldPC is a time-to-digital converter, or TDC card that interprets the electrical signals from the MCP and spectrometer respectively. This data is processed as *list mode* file, with raw values being passed into CoBoldPC, which will then produce histograms as seen in Figure 2.4. Each value in the *list mode* file is what we refer to as an *event*, as it contains the travel time of the fragment, as measured from a time of zero when the electron gun triggers to when it hits the detector, known as the MCP signal, as well as the fragment's position data on the MCP via a series of four anode signal wires. Each of these valued combine as an *event* for a single ion incident on the detector. The MCP signal is used to calculate the *TOF* as discussed above, and the four anode signals arrive at slightly delayed times after the MCP signal, with the time discrepancies allowing for a reconstruction of the position. This is done by letting the MCP signal be a reference point, and recording the following times of the four anode signals, to give a time value for each x_1, x_2, y_1 and y_2 position wires. Thus, t_{x1} is the time, measured in nanoseconds, for the x_1 signal to arrive after the initial MCP

signal, and so on for the other three anode signal values. To see the true position of the hit, we can calculate the *x* and *y* position of an event via a fundamental physics formula under constant velocity:

$$x = v_{drift}\,(t_{x1} - t_{x2}) \quad \text{and} \quad y = v_{drift}\,(t_{y1} - t_{y2}) \tag{2.8}$$

Here, the two times producing the time difference for each position corresponds to a position anode signal either from the negative end or the positive end of the detector, respectively, using the center as the origin. Technically, since we know the width and height of the detector to be $80\,\mathrm{mm}$, only one time value per direction is necessary, but two times per axis serves as a redundancy check to ensure no false hits or noise in the signal propagation. The variable v_{drift} corresponds to the signal propagation speed across the anode wire grid. Given the known width of the detector of $80\,\mathrm{mm}$, and that the wire mesh has a pitch of $1\,\mathrm{mm}$, along with the rated propagation of a single pitch is $1.95\,\mathrm{ns}$, the v_{drift} is roughly $80\ \frac{\mathrm{mm}}{\mathrm{ns}}$. Thus, a signal can travel $0.5\,\mathrm{mm}$ across the face of the detector every nanosecond, allowing for the exact position on the detector with the origin at the center. Lastly, we use the difference of t_1 and t_2 for each axis to calculate the position, but their *sum* should be a fixed constant, regardless of where the fragment strikes the MCP. These time sums depend only on the length of wire from the MCP back to the TDC. Since it is constant, this helps determine if it is a real *event* or random noise from an errant fragment. Given that a fragment could, in theory, travel the full diameter of the detector in roughly 40 nanoseconds, based on our v_{drift} value, we expect the time sums to be in the neighborhood of just under 50 nanoseconds, this yields a rather tight window of time values, which is helpful to gate out noise hits that lie outside of this range. Now, of

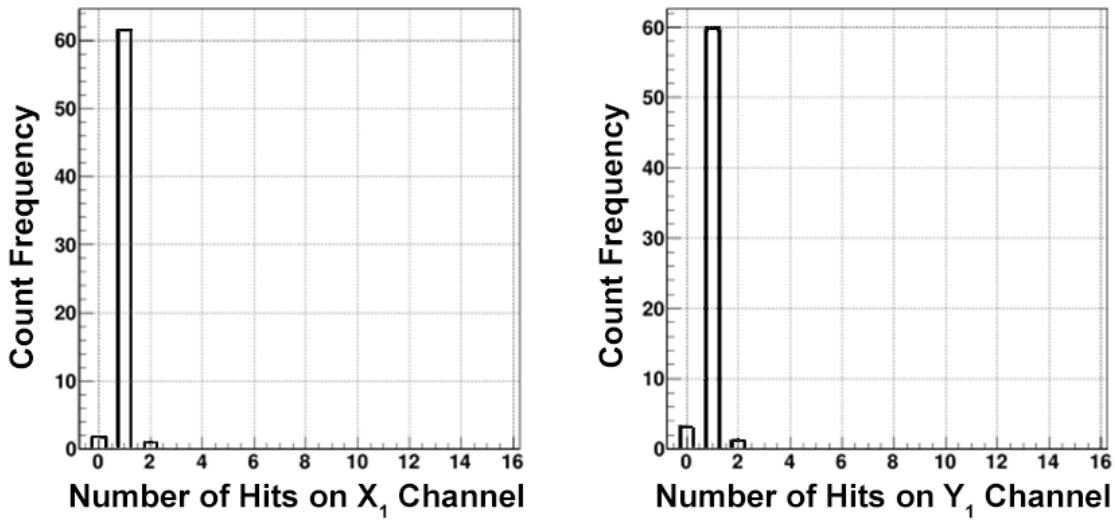

Figure 2.4: Histograms for the hits on each position channel, x_1 and y_1. The horizontal axis is the number of "hits" recorded by the MCP, with the corresponding vertical axis the frequency in which a particular hit count occurs. Theoretically all events would occur as a single hit across each anode signal, but double-triggering and noise can cause multiple hits. This serves as a diagnostic to ensure each signal is working and triggering correctly. Similar histograms for the redundant x_2 and y_1 channels are also used during acquisition.

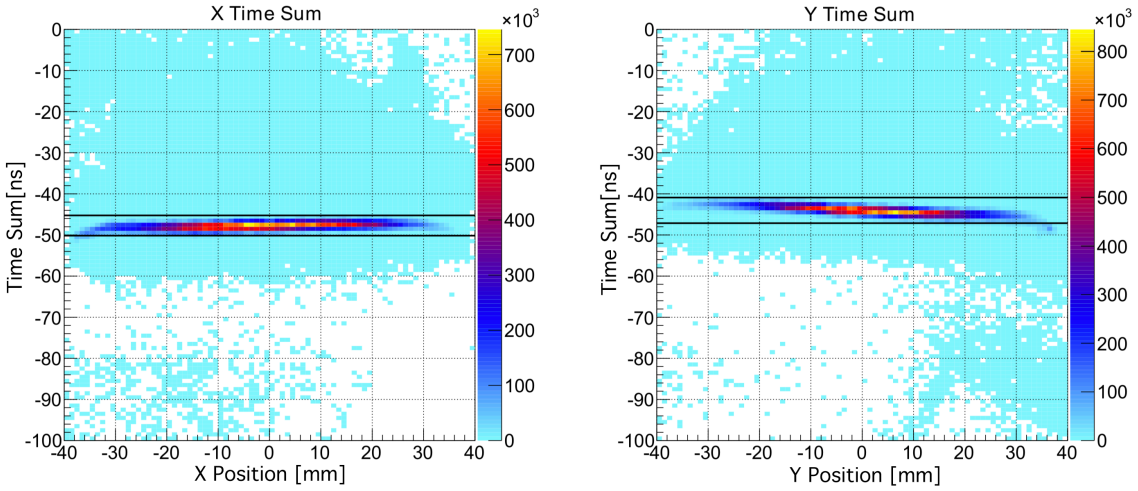

Figure 2.5: Time Sum plots for both position axes, x and y. The sum of the two times for a given axis should be the same across the entire face of the detector for *real* events, as the total travel time is equal after factoring out constants like cable length and interface connections. The time sum axis reads negative as we are looking back in time in reference to the initial MCP signal. Data inside the horizontal bars are kept during analysis, which allows for gating out non-uniform time sums, and serve as an additional diagnostic tool.

course the actual recorded value of the time sums is much greater as it includes the wire propagation time and is dependent on the wire length back to the TDC, but this is also a fixed value and can be easily subtracted off from our true time sum values. In order to ensure we capture real events during acquisition, close attention must be paid to each signal channel independently, to sure random signals and noise is kept to a minimum. Filtering is required to expose true data from erroneous signals. This is partially accomplished with a constant fraction discriminator, or CFD, that was first mentioned back in section 1.2.6. The CFD allows for pulses of different heights to be normalized and trigger at the same time, regardless of the size of that pulse. Properly tuning their triggering thresholds is pivotal to exclude noise within the line and any random signals that when once run through the logic

gating, are proven as false events; whilst keeping real events passing through to the TDC. This step of the acquisition is of immense importance to the overall analysis work, saving countless hours of guessing and trying gates on the software side. As mentioned above, we treat each of the four anode signals and the MCP reference signal as five independent channels, to both ensure no mixing of the signals and to pinpoint errors quickly on a certain line. Now that we have adjusted *TOF* values from the SIMION simulations, as well as adjusted pulse thresholds, the specific data for the experiment can be captured. In a DEA style experiment with a single anion fragment, the data is typically histograms of the *TOF*, position on the detector and momentum across the detector plane (x,y) relating the position to the flight times. For a more complicated experiment like that found in Chapter 4, additional data for each fragment correlating one to another is important and will be discussed further in this thesis.

In order for accurate momentum and energies to be calculated, we must be certain which fragment we are working with at all times, as there are two possible dissociation paths and channels as discussed back in section 1.1.3. This is done by plotting the entire *TOF* path and analyzing peaks, which correspond to specific channels occurring much more often than back-scattering or other noise that did plague this experiment. As seen in Figure 2.6 we see two distinct peaks, one roughly $4900\,\mathrm{ns}$ and another at roughly $16\,000\,\mathrm{ns}$. These correspond to the F^- and $CF_3{}^-$ fragments respectively. To double check these times, we can reference the linear relationship to the fragment's mass, with the lighter Fluorine anion arriving first, following by the heavier fragmentation channel. In order to isolate a specific channel, a gate is set around a tight range for the given *TOF* that is used in the subsequent plots as input for both momentum and energy density plots. The *TOF* is

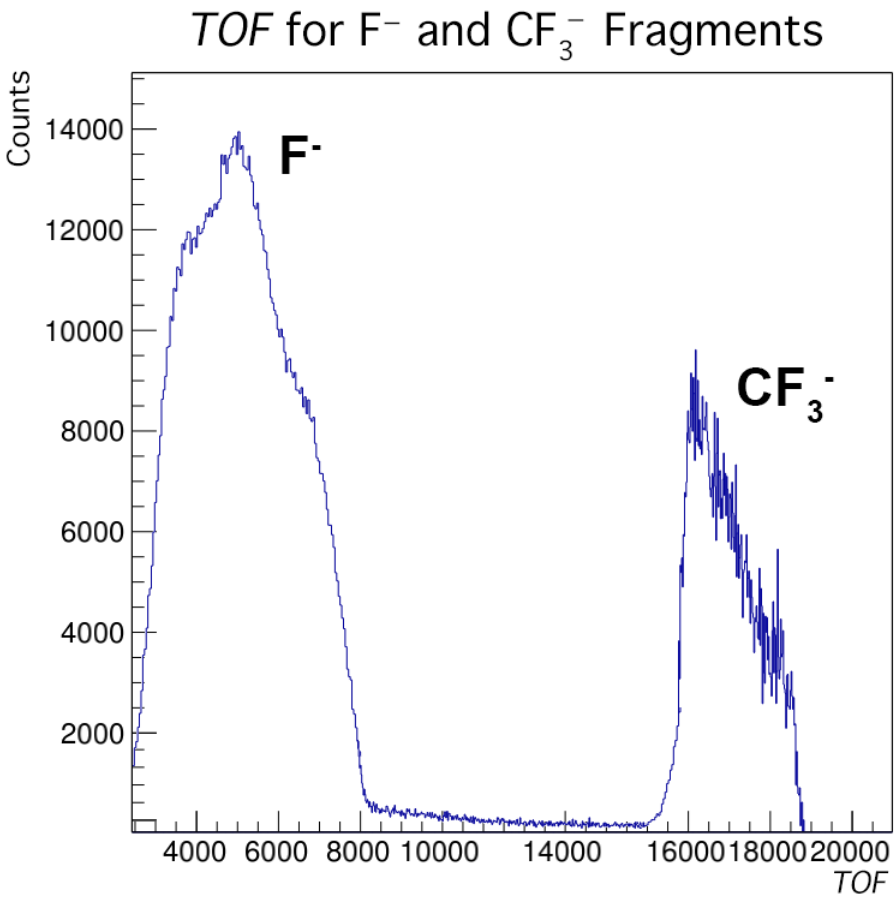

Figure 2.6: Time of Flight for both channels, the F^- and $CF_3{}^-$ anions respectively. A modified time *x-axis* is used to display both *TOF* peaks; individual plots were used to set time ranges for subsequent parameter calculations.

not perfect and features noise, which appears even after gating. To combat this, another restriction is put into place that seeks to ensure the fragment satisfies the conservation of momentum, since an ion following dissociation of a molecule would have momentum conserved, while a random hit on the detector from a stray ion would have no correlation to our initial momentum. This can be seen below on how the momentum is used for each axis of the detector face.

Next, the momentum can be calculated via the previous *TOF* ranges for each channel, with subsequent momentum density plots across the position axes for the fragment's incident momenta.

Using the time-of-flight information, the momentum is calculated for the detector plane:

$$\vec{p_x} = \frac{m\Delta x}{TOF} \quad \text{and} \quad \vec{p_y} = \frac{m\Delta y}{TOF} \tag{2.9}$$

Here we see the calculation for a fragment's momentum, given the *TOF* as well as the exact position on the detector. These two equations are run through some *C++* code to produce momentum density plots, as seen in Figure 2.7. This is accomplished with some custom software, LMF2ROOT[45] developed by a collaborative group in Frankfurt, Germany in association with RoentDek, designed to convert our TDC data files to the data visualization framework of ROOT, developed by the European Organization for Nuclear Research, also known as CERN. This object-oriented programs allows the multitude of events in list mode filed to be parsed and modified with restrictions, further parameters calculated and subsequently outputted as two and three dimension graphical plots. It is here we get our first glimpse of the post-interaction anion activity. Whilst the scale of both p_x and p_y in the figures are mostly accurate to actual values, the exact location of

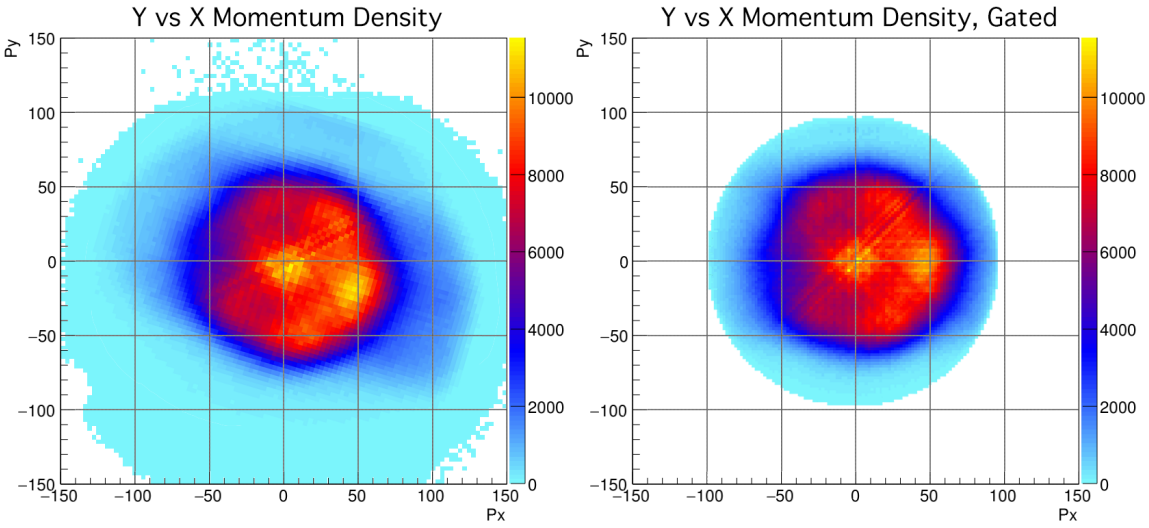

Figure 2.7: Momentum density plots of an F^- fragment at 7.5eV incident electron energy. In order to calculate accurate KER, the momentum must be centered relative to the origin by shifting and gating on only real events.

interaction is not necessarily at $x, y = (0, 0)$. This is due to the fact that the gas jet in the *y-axis* and the electron beam in the *x-axis* do not cross in the exact center of the spectrometer, causing the momentum density plot to not be perfectly centered at the origin. This is easily correct via software post-capture by shifting and rotating the incoming events, as well as "gating" out false events that do not correspond to proper momenta values. This is necessary before the next step of calculating the kinetic energy release, or KER, is performed. In addition to centering the momentum density plot, it is also necessary to ensure the magnitude of the momenta is constant for all directions. This must be true given that the dissociation fragments post-interaction are isotropic. This tells us the momentum density plots should be "round" in the figures. This is usually achieved after the capture during analysis using the same code as above, by performing a series of basic transformations to stretch or squeeze the event set to achieve a circular momentum plot. At this point the data

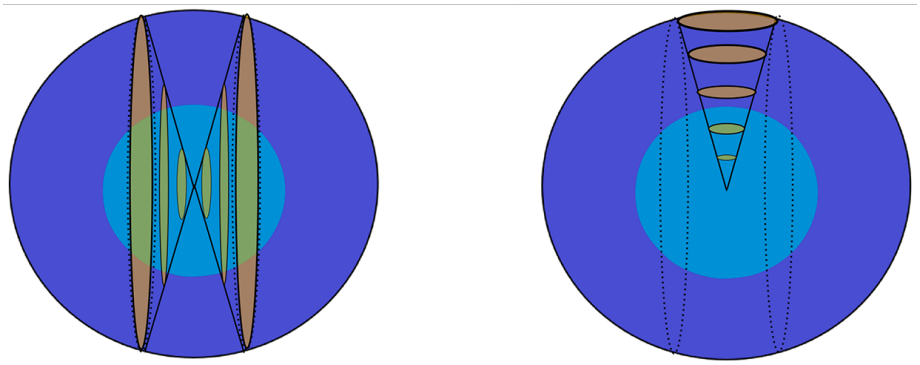

Figure 2.8: Collar gating (left) and cone gating (right) preserve the angular statistics of Newton spheres with different KER's. The full solid angle of the inner (light blue) will be kept, whereas only a fraction of the outer (dark blue) sphere will remain.

can be observed as the captured events are saved to an acquisition and analysis computer. The remaining parameters can be calculated offline, yet these simple histograms of count frequency and time sums ensure we have a clean signal that is accurately portrayed during the experiment.

2.3 CF_4 Dissociation Results

Each of the two possible channels following dissociation of the CF_4 molecule will be examined, with the CF_3^- fragment and high energy channel being reported first. In order to accurately understand the underlying mechanisms of the molecular breakup, appropriate representation of the dissociating Newton sphere is crucial. Experiments that rely on velocity slice imaging, or VSI, for capture, can only collect events for a specific *TOF*, thus only fixed width slices of the the Newton sphere. Projecting these equal thickness "slices" of the Newton sphere does not maintain the appropriate solid angle for all data across the range of ion energies. Projecting the entire Newton sphere, on the other hand,

obfuscates detail. COLTRIMS experiments do not have this problem, as we can capture the entire 4π solid angle, and as such, we then present a thin wedge of the Newton sphere that maintains solid angle for all values of $|\vec{p}|$, in a so-called "collar gate." Collar gates take a slice of data within a fixed angular distance from a certain plane, preserving the solid angle. This is necessary given that a fixed width slice of the sphere does not capture a fixed amount of the low KER, given that a low KER Newton sphere features a smaller radius in the so-called momentum space, resulting in clipping of the corresponding KER, this is seen during the F^- fragment results in section 2.3.2. Given that COLTRIMS provides fully resolved 3D momenta, a similar gate is also used, known as a cone gate. These gated work the same way as collars, but instead of using a given plane as reference for the fixed angular distance, a specific *axis* is used, thus resulting in conical slices moving along the Newton sphere, shown in Figure 2.8. For the high KER channel the F^- fragment utilized 5° and 10° collar gates, whereas the $CF_3{}^-$ channel used a 10° collar gate that showed all data within the given angle of the lab frame in the *x-t* plane. That is, the plane that is includes both the electron beam path (*x-axis*) and the *TOF* path (*t-axis*). These two gates produced the cleanest images, shown in figures 2.12 and 2.15.

2.3.1 $CF_3{}^-$ High Energy Channel Results

The higher energy channel, the $CF_3{}^-$ fragment, was analyzed in depth during this thesis work. Attachment along the direction of a C_2 symmetry axis' between the C-F bonds orients the CF_4 molecule in such a fashion that following dissociation of the molecule, the $CF_3{}^-$ negative anion is pushed at a roughly 35° angle from the *y-t* plane perpendicular to the incident electron beam. This push yields anion positions at approximately 70°, 120°,

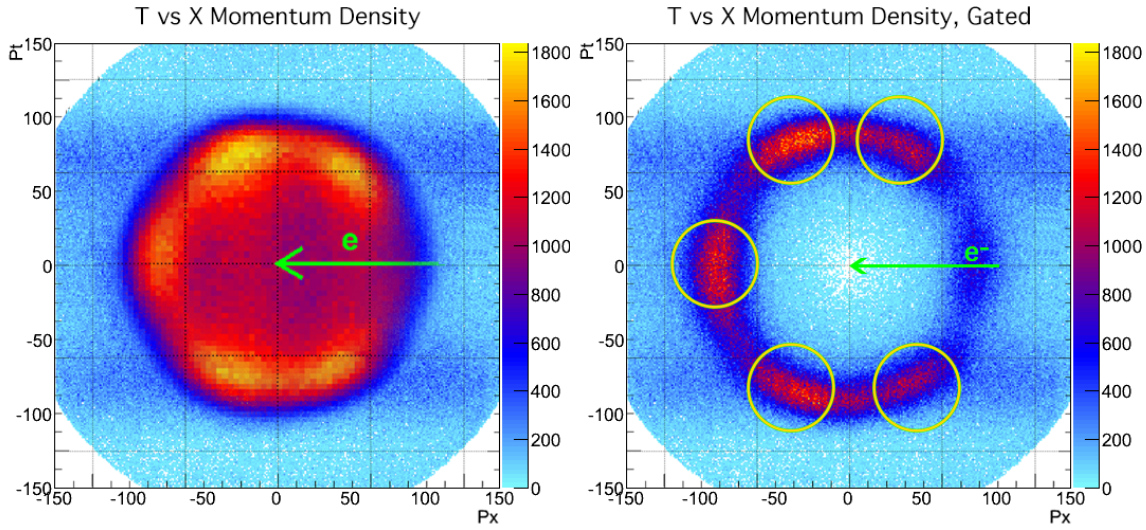

(a) Projections of the Newton sphere along the *x*-*t* plane for the CF_3^- fragment at 7eV.

(b) Same event data after an appropriate cone gate, the five islands are now clearly visible.

Figure 2.9: CF_3^- channel momentum density plots for 7eV incident energy without (left) and with (right) a conical gating. Although plotting all of P_t vs P_x yields cylindrical symmetry, gating on thin slices of the Newton sphere captures angular distributions cleanly. Background noise was minimal and kept in many of the momentum density plots.

240°, and 290° measured off the incident electron beam when viewing in the *x*-*t* momentum plane. A clearer picture of these four islands can be seen in the above Figure 2.9. To understand precisely why these four ion clusters appear at these approximate angles, we must analyze the angular distributions. Lastly, if attachment is along the direction of the C-F bond plane, regardless of any rotations about the bond, yields a CF_3^- ion that travels in the same direction as the incident electron, producing a peak directly across at 180°. This is the fifth island seen in the momentum density plots. These clusters of ions follow the symmetry discussed above regarding breaking along the C-F bond. This is sufficient for an angular distribution along one dimension to be studied, see Figure 2.11. Additional

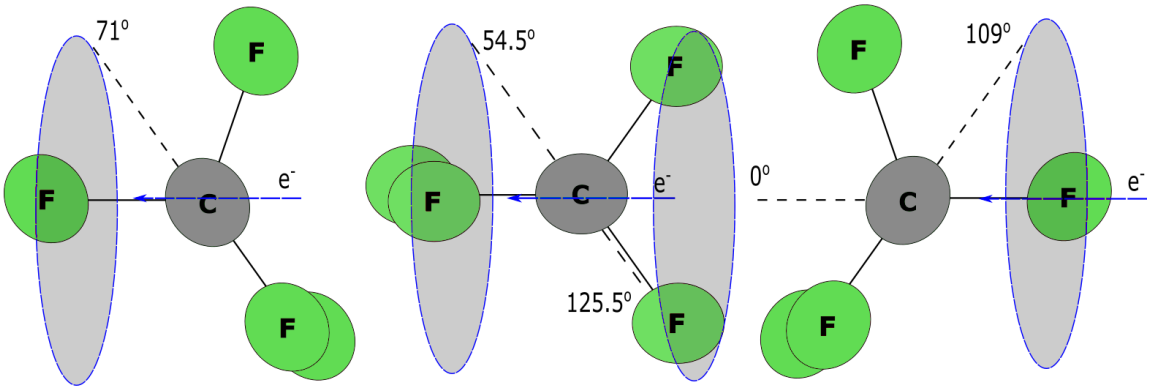

Figure 2.10: Attachment diagram showing the various possible orientations during dissociation. Electron attachment opposite of a C-F bond (left), between adjacent C-F bonds (center), and directly along a C-F bond (right).

energy levels were measured, ranging from 5ev upwards to 10eV. These high channel density plots can be seen on a dedicated page, see Figure 2.12. One of the main goals when investigating this fragment was to first, ensure similar results to previous experimental data by both Le Coat *et al*[3] and that of Ómarsson *et al*[22] regarding the momenta and angular distribution. This high KER channel is also the source of the claim by Ómarsson *et al* for the CF_3^- fragment that was touched on in section 1.1.3. This claim of an abrupt change in the rate of KER with respect to the incident electron energy was attempted to be reproduced by calculating the KER across the incident energy range, reference Figure 2.13. In analyzing the angular distribution plots, information is gleamed from the electron beam's incident angle in reference to the various covalent bonds. When the incident electron is along the axis of a C-F bond, the dissociation cross sectional area is quite large, leading to a break of the bond and the spike in the angular distribution at the origin at 0°. Whereas, if the incident electron is directly down the C-F bond path, or directly opposing it, it is unlikely that particular bond will break, instead the non-coaxial C-F bonds are subject to

breaking, yielding anion fragments at roughly 71° and 109° on the angular distribution. A final symmetric orientation of the molecule is where the incident electron arrives directly between two C-F bonds. Given each Fluorine is separated by an angle of 109°, the middle angle of 54.5° for the electron yields just an anion angle of also 54.5°, and across at 124.5°. Diagrams of these molecule orientations can be found in Figure 2.10. These angles show up in our one-dimensional angular distribution plots, shining light on the island placement in the momentum density figures. Our estimates of ≈70 ° and 120°, and the subsequent mirror below the *t-axis* for "rings" of ions in the momentum density plots are mostly highlighted in the angular distribution, but once vector arrows are added, it becomes evident what attachment orientation from Figure 2.10. We clearly see peaks resulting from an attachment between adjacent bonds, as well as directly along a bond. Additional angular plots were not utilized during the analysis given the attachment angles were discovered with a simple one-dimensional plot. Attention was shifted to momentum density figures over the energy range to highlight capture and yield based upon incoming energy to gain a better understanding of the KER, and attempt to reproduce Ómarsson *et al*'s claim.

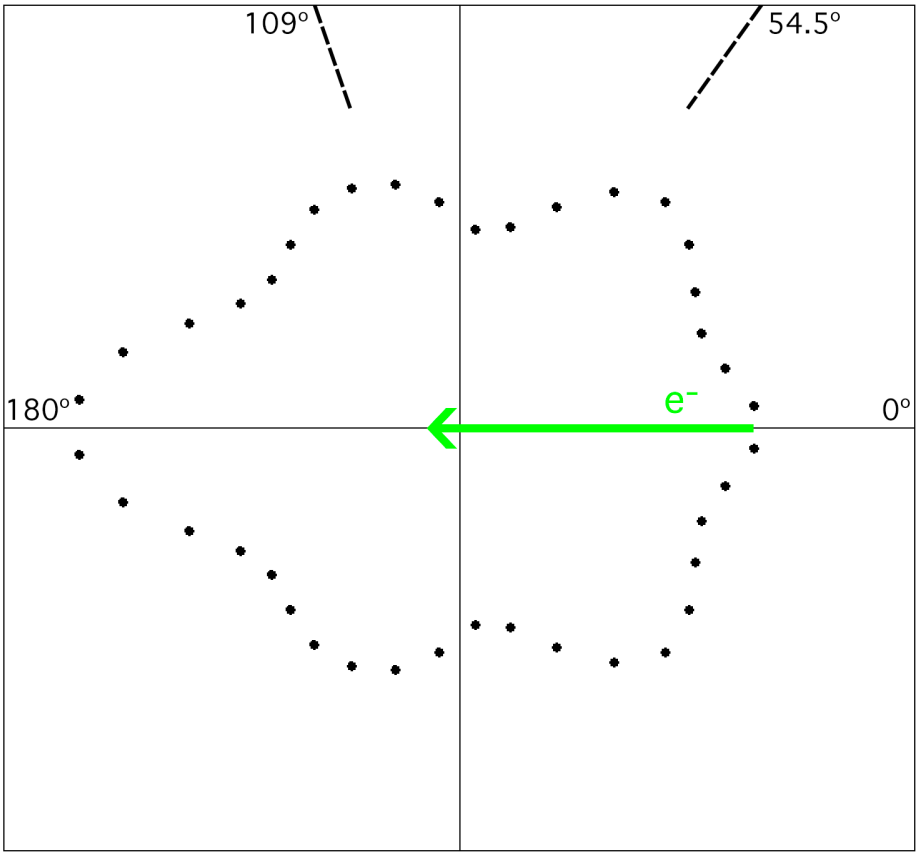

Figure 2.11: Angular distribution for the CF_3^- fragment with 8eV of incident energy. Reference angles marked clearly show attachments between adjacent bonds (54.5°), as well as directly along a bond (109°). A collar gate was applied in momentum space prior to the angular distribution.

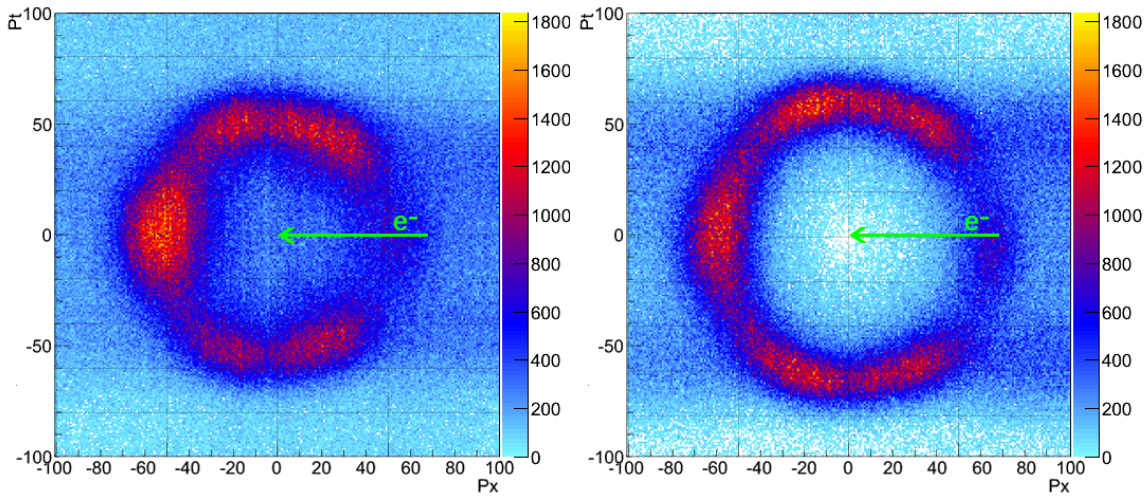

(a) 5eV Incident Energy (b) 6eV Incident Energy

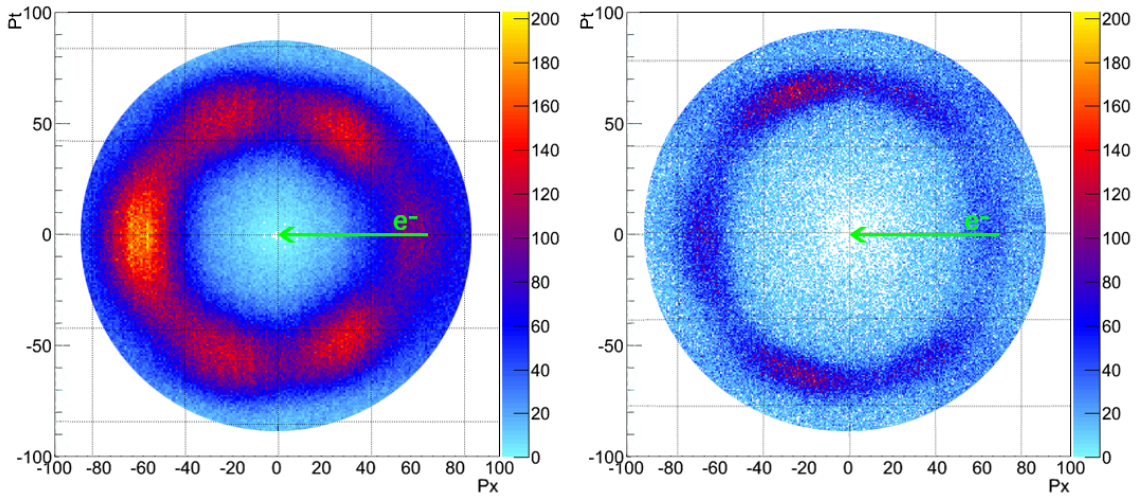

(c) 8eV Incident Energy (d) 9eV Incident Energy

Figure 2.12: Gated T-X momentum density plots for the CF_3^- channel across the incident energy range of 5eV to 9eV. The threshold incident energy, 7eV, was seen prior in Figure 2.9. Above threshold, the event count drops significantly, thus a background suppression was done to enhance statistics.

The last piece of the puzzle to understanding the dissociation process is the Kinetic Energy Release (KER) of the fragment post-dissociation. This was of large importance to uncover both the foundation of the channel, but also to aid in explaining the unique signature found by a previous experiment by Ómarsson *et al*.[22] This was done by comparing the KER generated via DEA for the incident energy ranges used above. These results, along with previous experiments by and that of Le Coat *et al*[3] and Ómarsson *et al* can be seen in Figure 2.13. This unusual result appears with an abrupt shift in energy around the 6.5eV electron energy, causing an increase in the $\frac{dE_{KER}}{dE_{electron}}$, whereas our data, as well as Le Coat *et al*'s experiment have found this energy rate to be single-valued. At this time, the Auburn group chooses not to comment on the cause of the nonlinearity in the KER rate found by the Ómarsson group.

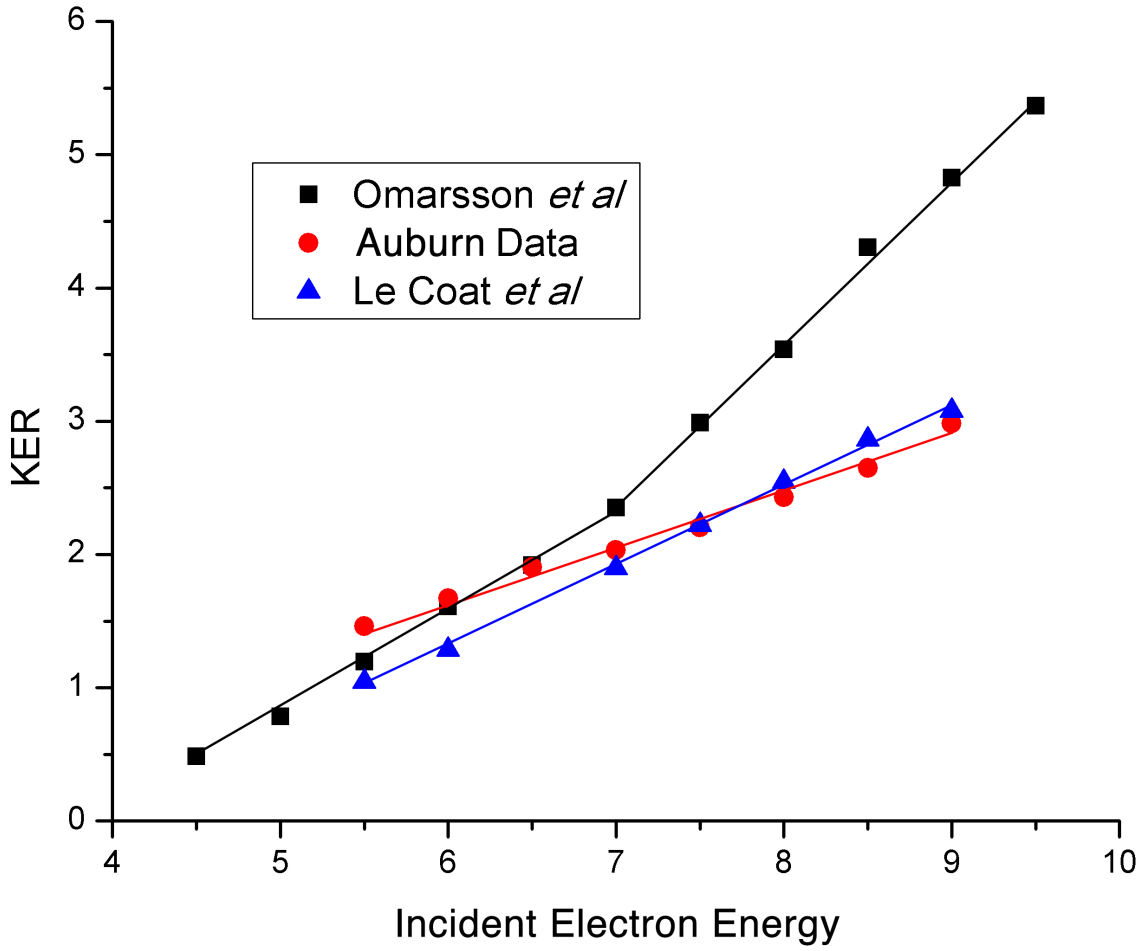

Figure 2.13: Kinetic Energy Release as a function of the incident energy for the CF_3^- fragment along with experimental data from Le Coat and Ómarsson.

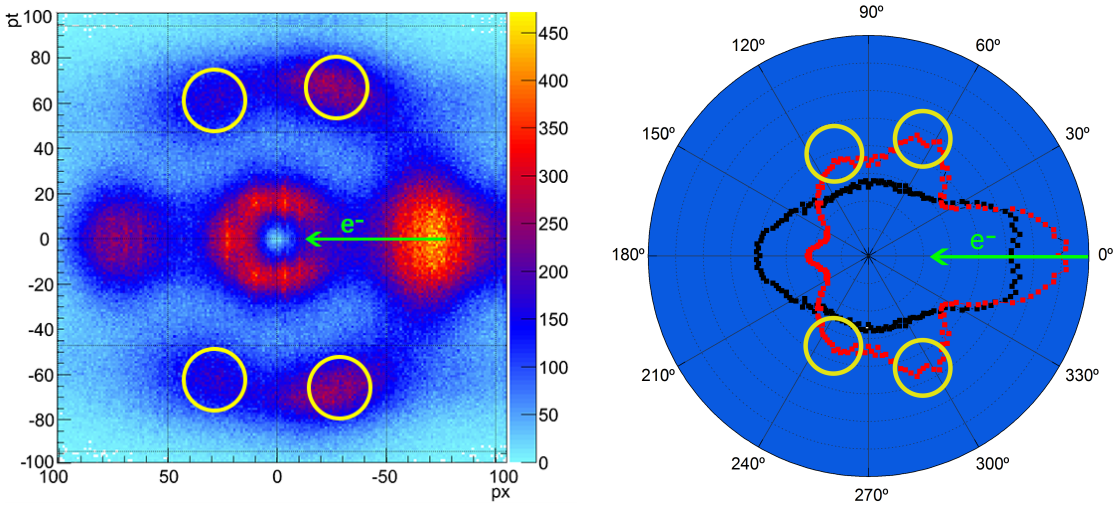

(a) P_t vs P_x momentum density plot with collar gating for the F^- fragment at 8eV incident electron energy. Outer lobes represent the high KER, inner is the low KER.

(b) Angular Distribution of F^-. Angles are measured off of the incoming electron. Outer Lobes are represented in **red** whereas inner lobe statistics are in **black**.

Figure 2.14: F^- channel momentum density and subsequent angular plot for 6eV incident energy. Only a cone gate was applied to the momentum density events. The islands represent the high energy channel of the F^- fragment, seen clearly in the angular plot. The center section is the low KER channel of the fragment, exclusive to the lighter F^- anion.

2.3.2 F^- Channel with High-and-Low KER Results

The second channel, the F^- fragment, was also measured by the Auburn group following in the heels of previous work to expand the knowledge of the Carbon Tetrafluoride molecule. In analyzing both channels, it was found that two resonances exist for the molecule, one centered at $\sim$ 6.8eV that yields high kinetic energy fragments of $CF_3{}^-$ and F^-, as well as as second resonance at $\sim$ 7.7eV yielding low kinetic energy release F^- fragment.[22,23] This second resonance is seen clearly during the F^- momentum density plots, seen on the next page. When plotting our usual P_x vs P_t we see the islands, or clusters, of

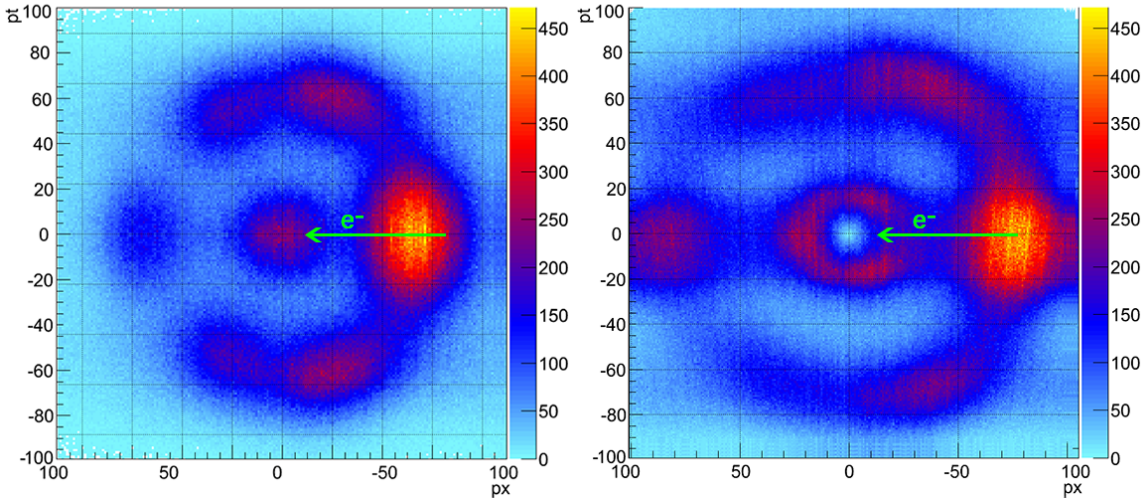

(a) 5eV Incident Energy (b) 7eV Incident Energy

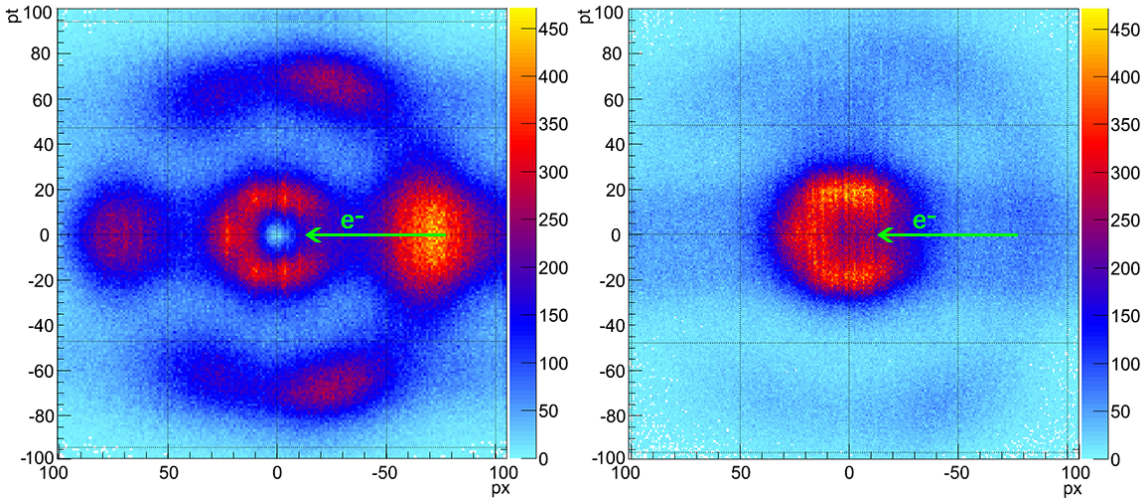

(c) 8eV Incident Energy (d) 9eV Incident Energy

Figure 2.15: Gated T-X momentum density plots for the F^- channel across the incident energy range of 5eV to 9eV. The low kinetic energy can be seen present above 7eV, with the high kinetic energy disappearing above the second resonance above 8eV. With limited counts for the F^- channel, we kept the background with only collar gating for uniform statistics.

ions similar to the ones featured in the CF_3^- plots, indicative of the high kinetic energy resonance. The symmetric distribution in the center that appears around an incident electron energy of 7eV is the other CF_4 resonance, the low KER channel. This resonance yields the F^- fragment seen in the center. Given that this resonance appears at a higher incident electron energy, we do not see much evidence of the center distribution in the 5eV or 6eV measurement, and likewise, at higher incident electron energies, we also see the absence of the high KER channel and a dominance of low KER events for the corresponding F^- fragment, as seen in Subfigure 2.15d. Thus, we see the evidence of a second resonance at play, highlighting just the low kinetic energy F^- fragment. In the middle at 8eV, we see both resonances, low energy F^- in the inner ring, as well as high energy F^- in the outer islands. This is nicely exposed during an angular distribution plot, see Figure 2.14. This clearly shows both energies as well as the impact angle, which exposes the symmetry group and bond breaking behavior at play.

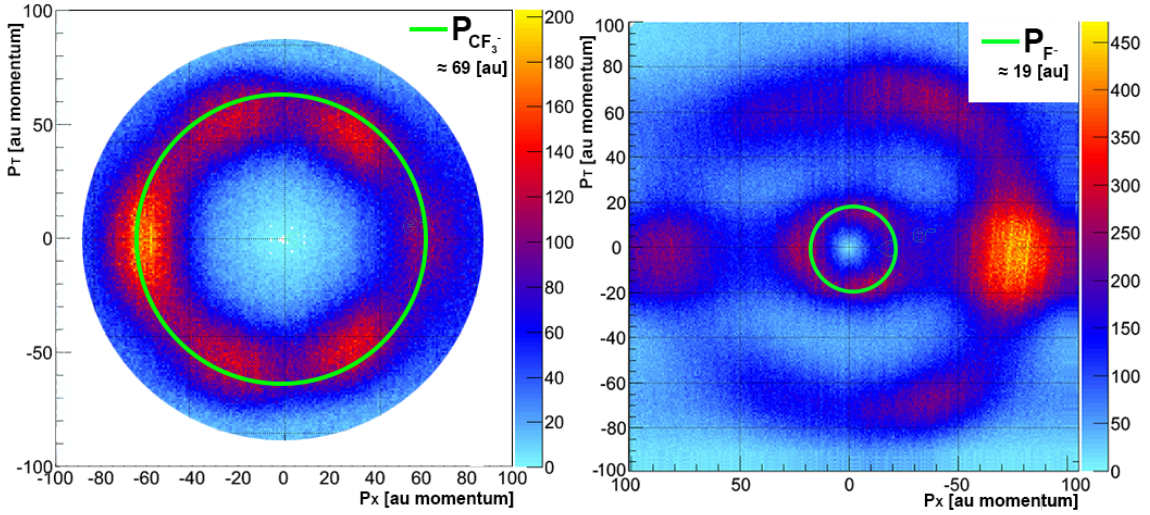

(a) CF_3^- channel with the momentum radius centered around the islands (green circle.) This momentum radius is equal to the mass of the CF_3^- fragment, ≈ 69 a.u.

(b) F^- channel with the momentum radius centered around the inner structure (green circle.) This momentum radius is equal to the mass of the F^- fragment, ≈ 19 a.u.

Figure 2.16: The ratio of $\frac{P_{F^-}}{P_{CF_3^-}}$ is equal to the ratio of their masses, $\frac{19}{69} \approx 27.5\%$. This ratio relates the two channels in momentum density, with the corresponding islands existing at these mass ratios.

Unlike the heavier CF_3^- fragment and subsequent high kinetic energy, the symmetry of this lighter F^- ion at low kinetic energy is not well-defined. Given this, we cannot determine the symmetry in regards to the angular distribution and cannot comment on any reflection along the incident beam axis as analyzed in the high kinetic energy cluster. Thus, we called upon the measurements by Le Coat *et al* that fitted a T_d point group symmetry to the low KER F^- fragments using p, d and f partial waves.[3] This allows for some insight into the underlying resonance, stemming from a core-excited shape resonance of T_1 symmetry, as proposed by Tronc *et al*[34] utilizing a diatomic model. This is mostly accurate, but conflicts with the reports of F. H. Read[32] that a T_1 symmetry within the T_d

point group is not allowed to have contributions from *p* and *d* partial waves. Therefore, we concluded the low kinetic energy contribution is due to a core-excited shape resonance of T_2 symmetry, still within the T_d point group.

In order to capture this lighter fragment accurately, a lower incident energy and subsequent pulse scheme was required. This posed a challenge for the electron gun used in the Auburn DEA experiment, as seen back in section 1.2.2. More noise is found during the low KER data, contributing to a reduced electron gun energy resolution, as well as a larger chamber background. This makes ensuring clean statistics a challenge, and is seen when calculating the kinetic energy release across the incident energy range. Nevertheless, one dimensional energy plots were created of the F^- fragment for completeness, but the accuracy below the threshold energy of $\sim$ 7eV cannot be verified.

2.3.3 Carbon Tetrafluoride Analysis Summary

The planning, setup, calibration and analysis of any of this type of experimental research is exhaustive yet rewarding. This was particularly the case with this particular molecule, and ushered in a better understanding of the fundamental processes. During the tasks of scientific research, the ability to not only produce new science but reproduce existing results is pivotal. As was the case with this experiment, we attempted to reproduce some obscure data on the dissociative electron attachment of Carbon Tetrafluoride with slightly conflicting results. The Auburn experiment mostly aligned with several prior measurements, including the locations of the angular distributions and momentum density plots, with some small discrepancies on amplitude. However, the kinetic energy calculations of the Auburn group did not coincide with the challenged experiment, indicating a

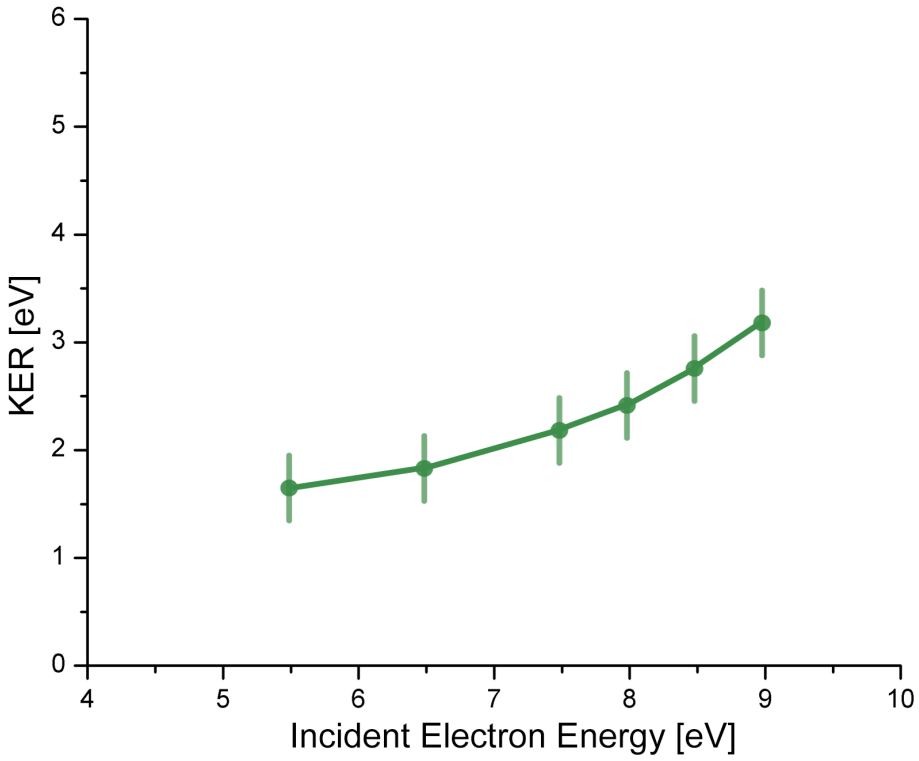

Figure 2.17: Kinetic Energy Release as a function of the incident energy for the F^- fragment. Error bars are placed at 0.3eV to account for the electron gun energy resolution. We cannot comment on the shift in $\frac{dE_{KER}}{dE_{electron}}$ below the threshold resonance at 7.5eV. This plot is shown for educational purposes and should be used as guidance rather than fact.

need for further scrutiny as we refine the experimental process to improve understanding of this complex system.

Chapter 3

Molecular Dynamics Following Double Photoionization of NH_3, Ammonia

3.1 Introduction to Photoionization

The primary experiment presented in this thesis examines the molecular dynamics of a triatomic molecule, NH_3, following core ionization of the molecule. This is accomplished via a photoionization process, with the absorption of a soft X-Ray photon that is produced via the synchrotron at the Advanced Light Source (ALS), discussed within the next section.

$$\gamma + \mathrm{NH_3} \longrightarrow {\mathrm{NH_3}}^{+*} + \mathrm{e}^{-}_{\gamma} \tag{3.1}$$

Here, we see the soft X-Ray excite the stable molecule to yield an excited and positive molecule with a photoelectron, both fragments we can study with a dual detector setup. To measure these fragments and subsequent photoelectron, we need a more complex dual

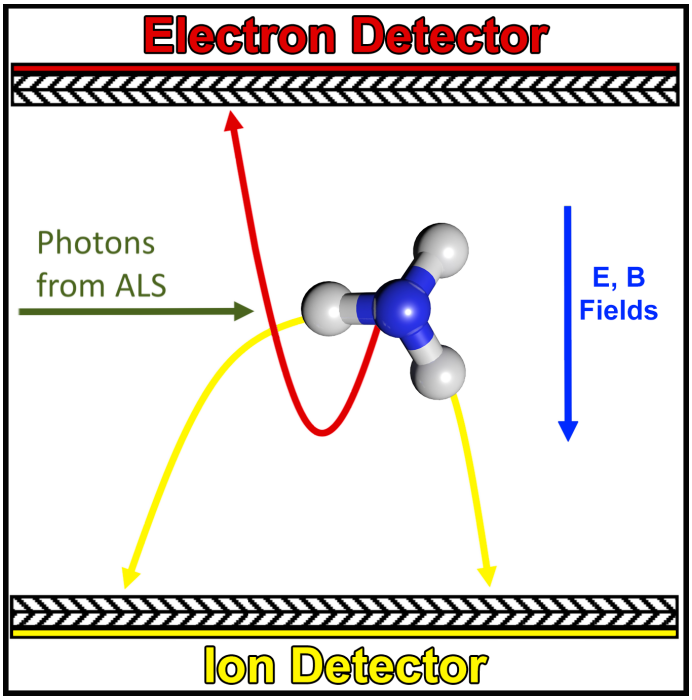

Figure 3.1: A simplistic diagram of the COLTRIMS apparatus with a dual detector setup. A static electric field exists within the interaction region that directs the fragments to their respective MCP detectors.

detector setup than the electron detector used for the Dissociative Electron Attachment experiment discussed previously. In order for photoionization to occur, a soft X-Ray photons must collide with a neutral molecule via a gas jet. The NH_3 molecule consists of both two and three body breakups following ionization, with several possible breakup pathways involving both negative and positive ions. The specific ionization process studied for this experiment is known as single-photon double-ionization (PDI),[41] a process in which two electrons are removed simultaneously from the molecule by a single photon is a clear signature of electron correlation. Thus, we have two electrons to be measured on an anion

detector along with any ions on a positive ion detector. This complex process of dual detectors following ionization requires a great deal of experimental and calibration prowess, and is more in depth in understanding the molecule than the single electron DEA process. The workings and process of PDI will be the main focus of this chapter.

In investigating the Ammonia molecule, the challenge of discerning all the possible fragmentation channels produced in this experiment quickly arose. As seen below, following ionizing with a soft X-Ray photon, γ, we have several possible fragments, both two and three body channels.

$$\gamma + \mathrm{NH_3} \longrightarrow {\mathrm{NH_3}}^{2+*} + 2\,\mathrm{e}^-_\gamma \begin{cases} \rightarrow \mathrm{NH_2^+} + \mathrm{H^+} + 2\,\mathrm{e^-} & (3.2a) \\ \rightarrow \mathrm{NH^+} + \mathrm{H^+} + \mathrm{H} + 2\,\mathrm{e^-} & (3.2b) \\ \rightarrow \mathrm{N^+} + \mathrm{H^+} + \mathrm{H_2} + 2\,\mathrm{e^-} & (3.2c) \\ \rightarrow \mathrm{NH^+} + \mathrm{H_2^+} + 2\,\mathrm{e^-} & (3.2d) \\ \rightarrow \mathrm{NH} + \mathrm{H^+} + \mathrm{H^+} + 2\,\mathrm{e^-} & (3.2e) \end{cases}$$

Of these five channels only two have been observed in our PDI experiment, namely, one two-body, (3.2a), and one three-body, (3.2e), breakup. It is worth noting that in the three-body case, the third fragment, NH, is neutral, and is not captured in the COLTRIMS experiment directly. To combat this, the neutral fragment is found via three-dimensional momentum reconstruction during analysis. In the case of 3.2e, we rely on the two ions and the subsequent two removed anions following ionization. Identifying the specific channel being captured is aided by a few analysis tools, one of which is via a Photoion-Photoion

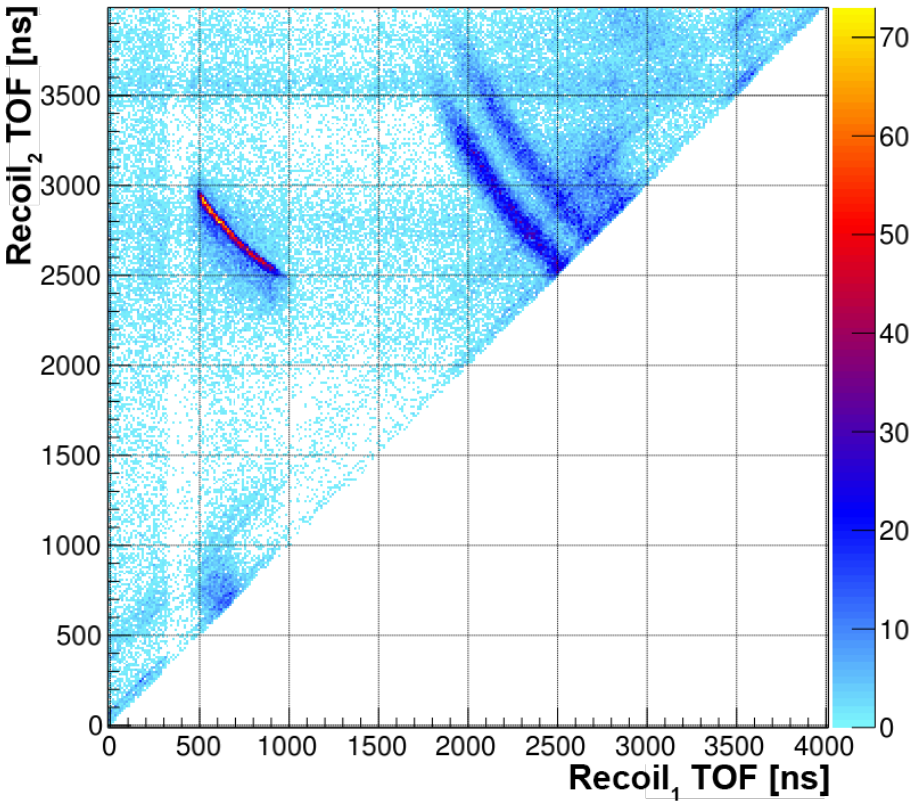

Figure 3.2: A quick pass PIPICO Histogram featuring the PDI of NH_3, with emphasis on a single proton channel breakup such as $NH_2^+ + H^+$. The heavier ion, the NH_2^+ fragment, arrives later around 2500ns, with the lighter proton seen around 500ns. Evidence of dual proton three-body stlye channel, H^++H^+, at a low *TOF* is also present. This quick pass is used to identify channels for later presorting.

Time of Flight (TOF) Coincidence, or PIPICO, plot. A PIPICO plot is a two-dimensional histogram of the TOF of the first ion to strike the recoil detector, verses the TOF of the second ion to strike. This mainly allows for the correlation between the recoils, but also helps separate the specific fragment channels, aiding in discovering the breakup pathway. A PIPICO for the recoils is seen in Figure 3.2 and clearly features the NH_2^+ (Equation 3.2a) channel, highlighting the conserved momentum along the parabolic path. Later, specific

gates based upon TOF for the recoils in coincidence and paired electrons can be used on the PIPICO to ensure good data is parsed and successfully eliminate background noise. These PIPICO plots are used during initial data capture to align the fragments on the detector and adjust field strength in addition to post analysis for background suppression. Additional methods of data presorting is discussed in Section 4.1.1.

Following channel identification, the actual recoils and accompanying electrons must also be properly measured, to ensure valid hits on each detector. This is done in a similar fashion as the DEA experiment using the TOF for each fragment. A nice method exists for the positively charged ions, given that the recoils vary in both mass and charge, their flight times are not constant and change with field strength unlike the fixed mass and charge electrons. The method to find the recoil acceleration due to the electric field can be found via by relating the Lorentz Force equation for an electric field to that of Newton's Second Law of motion:

$$\vec{F_{field}} = q\vec{E} = m\vec{a} = \vec{F}_{motion} \tag{3.3}$$

Thus we see the acceleration of the ions as a function of the electric field within the spectrometer:

$$\vec{a_{ion}} = \frac{q\vec{E}}{m} \tag{3.4}$$

Now, given that the ion's motion is time-dependent, we can invoke a Taylor Series expansion for the particle beginning at some arbitrary initial time, $t_\circ$, up to some time t, our TOF:

$$\begin{aligned} x(t) &= \sum_{n=0}^{\infty} \frac{x^{(n)}(t_\circ)}{n!}(t-t_\circ)^n \\ &= x(t_\circ) + \frac{x'(t)}{1!}(t-t_\circ) + \frac{x''(t_\circ)}{2!}(t-t_\circ)^2 + \frac{x'''(t_\circ)}{3!}(t-t_\circ)^3 + \cdots \end{aligned} \tag{3.5}$$

Given the time derivatives of position correspond to velocity and acceleration, coupled with a change in position:

$$\begin{aligned} x' = \frac{dx}{dt} = v_\circ = &\quad \text{velocity} \\ x'' = \frac{dx}{dt} = a = &\quad \text{acceleration} \\ x(t) - x(t_\circ) = \Delta x = &\quad \text{change in position} \end{aligned}$$

The Taylor Series cleans up into a very familiar kinematic equation:

$$\Delta x = v_\circ t + \frac{1}{2} v_\circ t^2 + \cdots \tag{3.6}$$

Lastly, assuming an initial velocity of zero, and solving Equation 3.6 for time, we can substitute in the particle-dependant acceleration from Equation 3.1 to see the effect of

mass and charge on the fragment TOF:

$$t = \sqrt{\frac{2\Delta x}{a}} = \sqrt{\frac{2m\Delta x}{q\vec{E}}} = \sqrt{\frac{m}{q}}\sqrt{\frac{2\Delta x}{\vec{E}}} \tag{3.7}$$

The electric field is a constant value during capture, and the Δx is fixed from the physical spectrometer, leaving the TOF directly proportional to the square root of the mass-to-charge ratio:

$$\text{TOF}_{\text{ion}} \propto \sqrt{\frac{m}{q}} \tag{3.8}$$

This is extremely helpful for initial calibration in determining what the proper flight times for the recoils. A variant of this relationship is used via Excel to allow the researcher to uniquely identify the ionic fragments within a TOF spectrum, as seen back in Figure 2.1. Given the possible breakup fragments seen in Equation 3.2, the different recoils are separated by a single Hydrogen atom usually, a small mass difference from channel to channel. This closeness in TOF results in our PIPICO lines potentially being grouped together, posing a challenge for sorting hits to the proper channels via visual inspection. A way to combat this is with an extensive three-dimensional conservation of momentum algorithm, using each channel fragment masses as inputs, along with the fields within the spectrometer, to calculate the initial and final momenta for the fragments. This ensures the resulting hit corresponds with the correct channel by cross-referencing with our PIPICO and TOF plots.

Next, despite careful attention to calibration and simulation calculations, a number of other effects must be considered in the experimental setup. In a wildly complex experiment like COLTRIMS, measuring photoionization statistics, several nuances during

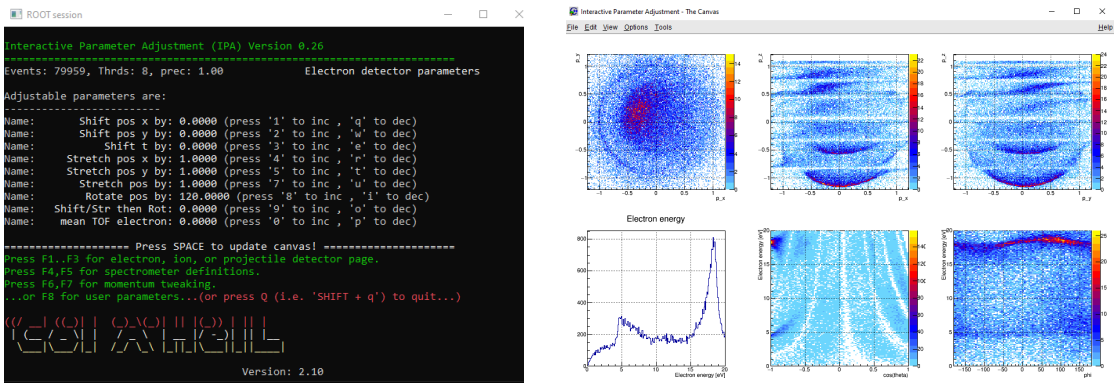

(a) Command Line Prompt for the IPA tool. (b) IPA framework for Momentum and Energy.

Figure 3.3: The Interactive Parameter Adjustment Tool allows for parsing of small amounts of incoming data whilst allowing for parameter calculations to overlay fits, allowing for on-the-fly calibration adjustments to the experimental setup.

the real world experiment will exist. Such as accuracy of power supplies that drive the electric and magnetic fields that may not be exactly equal to the readouts, all the way to pressure and flow differences in the jet nozzle may exist for example. To account for these real-world adjustments, our collaborators at the University of Nevada, Reno developed a software tool to account for this: the Interactive Parameter Adjustment, or IPA, tool. The IPA takes a small amount of data during acquisition of a specific channel and displays some of our calibration plots with limited statistics. Within the framework, plots of PIPICOs and TOF spectrum's are displayed with an interactive menu of adjustable parameters that will recalculate the displayed data. In this way, the experimentalist can adjust the parameters causing the skewed data, by modifying the electric and magnetic field strengths for example. The IPA framework calculates the TOF parabolas that form the PIPICOs via a PIPICO tool, seen in the figure above. With this tool, parameters such as particle mass, charge, field strength, and acceleration region to overlay onto the captured data. By

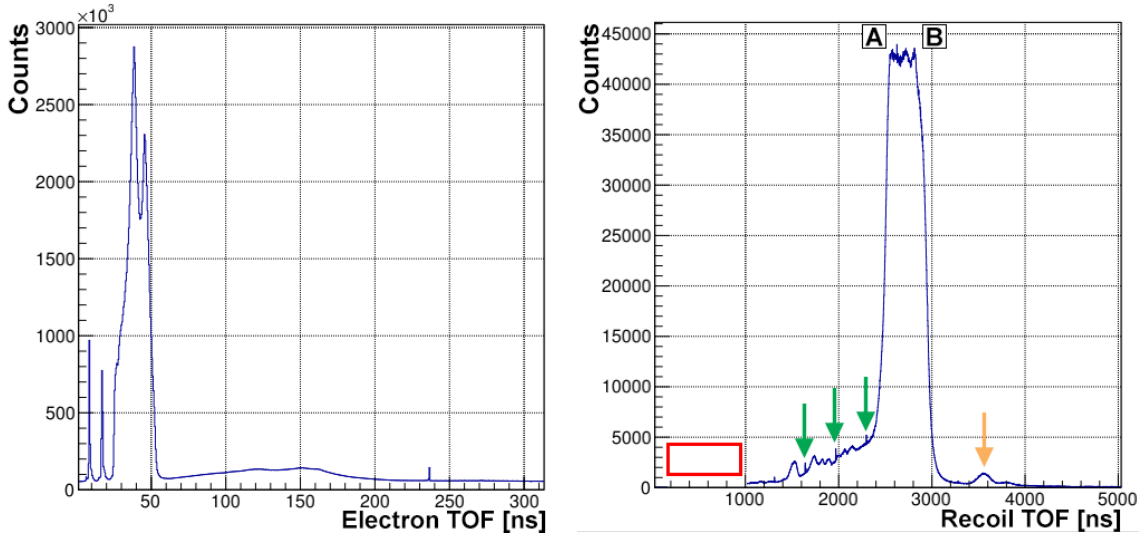

(a) Electron TOF Histogram

(b) Heavy Recoil TOF Histogram

Figure 3.4: Raw TOF Histograms for the electrons and recoils. The Electrons TOF plot stops at ≈ 326ns, which is the ALS Bunchmarker signal time. The Recoils TOF plot begins after 1000ns, with lower flight times for the lighter ions plotted separately (within the red box). The green arrows represent the ALS Bunchmarker, repeating every 326ns.

modifying the field strength, knowing the fragment mass and charge, we can see the theoretical calculation overlay onto the data and see a correctional factor for the electric field within the spectrometer. This information not only corrects for the data being captured, but also allows for insight on the accuracy of the experimental equipment when in use at the synchrotron.

Similarly to the DEA experiment, we rely on the time of flights for the particles. The ions can be related nicely to the mass and charge of the participle fragment, but the electrons are a bit trickier to ensure the proper photoelectrons from the breakup is recorded along side their companion recoils. The TOF of the electrons is *fixed* so they cannot be characterized from the mass/charge relationship that was so beneficial for the recoils. The

electric field stays fixed for the experiment, and should not change the electron TOF. The $\vec{B}$ field is parallel to the spectrometer, and as such also does not affect the TOF, but vastly complicates the momentum calculations, as seen in the 3.3.2 section. Thus, for the electron TOF we can define a condition based on the times, as long as they exist in occurrence with the recoils. A range is defined to account for slight anomalies within the experiment, and is checked against the recoils to produce a material condition:

$$\begin{aligned} \textbf{IF} \ (TOF_{e^-\,minimum} \ &\leq \ TOF_{e^-} \ \leq \ TOF_{e^-\,maximum}) \\ \textbf{AND} \ (TOF_{ion\ minimum} \ &\leq \ TOF_{ion} \ \leq \ TOF_{ion\ maximum}) \\ \textbf{THEN} \ \ event \ &= \ real \end{aligned}$$

This condition ensures that only electrons capturing during a certain window is captured along with the respective ion's TOF window, see Figure 3.4. Despite efforts to ensure a clean capture environment, noise existing from stray particles or Auger electrons are easily ionized and captured, as seen at the orange arrow in Figure 3.4, and can then be recognized as a false event within the TOF histogram and subsequently gated out. The electrons *TOF* is also verified via a *wiggles* run, which is a calibration method and plot done to both ensure proper $\vec{E}$ and $\vec{B}$ fields are present, as well as the true "time zero" signaling the arrival of the ALS bunchmarker signal. A *wiggles* run generates multiple cycles in the trajectory of the photoelectrons, which produces the "wiggles" in the spectrum, giving it the name to quickly identify the true time-sum. This is accomplished by de-tuning the electric field, allowing for the photo-electron's flight time to exceed the cyclotron time period, which was discussed back in Chapter 1 via Equation 1.11, which is equal to $\frac{2\pi m}{Bq}$. Additionally, the photon energy from the ALS is tuned to ensure the photo-electrons have

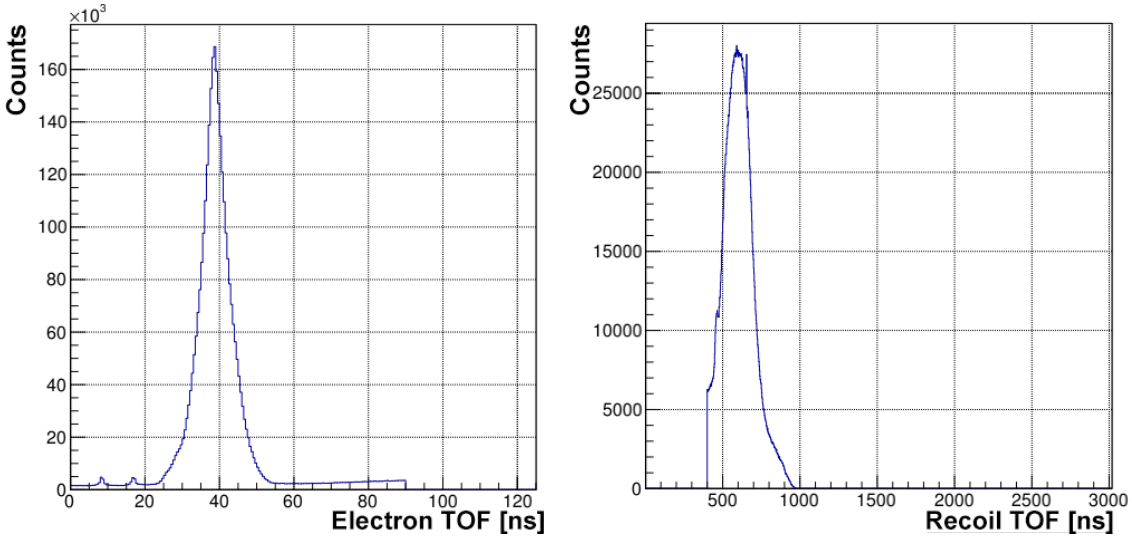

(a) Electron TOF Histogram (b) Light Recoil TOF Histogram

Figure 3.5: Specific ranges of TOF for both the electrons and light recoils. The lighter recoil arrives around 600ns, with electrons being around 40ns. Gates are placed around these spots along with position restrictions during presorting.

enough kinetic energy to complete a cycle and return back at the origin whilst traversing along the *TOF* direction towards the detector.

3.2 Synchrotron Source

This experiment was conducted on Beamline 9.0.1 at the Advanced Light Source (ALS), a 1.9 GeV synchrotron located at Lawrence Berkeley National Laboratory (LBNL). The ALS, shown in Figure 3.7 below, sits atop the Berkeley Hills, overlooking the San Francisco Bay, and is funded by the U.S. Department of Energy and managed by the University of California system. The ALS is a "third-generation" synchrotron, capable of producing some of the brightest sources of ultraviolet and soft X-ray light in the world.

Figure 3.6: The Advanced Light Source at Lawrence Berkeley National Laboratory, overlooking the East Bay into San Francisco, CA.[42]

The ALS has been operational since the early 1990's and features almost 40 user beamlines to conduct experiments, one of which was used to produce majority of the content in this thesis. A synchrotron produces the light by accelerating electrons in "bunches" to near the speed of light using a 1.9 GeV source, which equates to roughly 99.999994% the speed of light. The synchrotron operates by utilizing a storage ring, to accelerate the electron bunches to the desired energies. There are several technologies at play to deliver the soft X-Ray light to the end station such as bending magnets within the arc-shaped sections as well as undulators and wigglers within the straight portions of the storage ring. A typical beamline schematic, very similar to the one used on Beamline 9.0.1 used for

this experiment, is shown in Figure 3.8. On 9.0.1, a 10cm-period untulator is used, with energy ranges of 8eV up to 1,500eV to be selected by the user. To achieve this range of energies, an extremely high energy resolution monochromator with rotating grating was used, with the lowest energy gradating utilized, refining the energy to between 17eV and 80eV. A typical beam size is approximately $200\,\mu\mathrm{m}$ in the horizontal and $800\,\mu\mathrm{m}$ in the vertical, and is then modified with slits to adjust profile. All of our experiments operate in what is known as "2-Bunch" mode, with two electron punches orbiting the synchrotron ring. The 2-Bunch spacing period is $328.28\,\mathrm{ns}$, with a duty cycle of light pulses around 3Mhz. The light is then directed down a beam dump into the endstation, where the experimentalist can further tweak the light using optical devices such as mirrors, diffraction grating, monochromators and piazzo stages. The monochromator features two different diffraction gratings for further beam profiling, a 150 $\frac{\text{lines}}{\text{mm}}$ grating and 1200 $\frac{\text{lines}}{\text{mm}}$ grating.

The beam then passes through exit slits to further adjust the beam by modifying photon flux and conversely, energy resolution. For this particular experiment, the exit slits were set to $350\,\mu\mathrm{m}$ and the 150 $\frac{\text{lines}}{\text{mm}}$ grating was utilized to yield roughly 61eV linearly polarized photons, an energy above the threshold of the Ammonia molecule (40.34eV) to ensure photoionization.

3.3 Experimental Chamber

The photoionization experiment was carried out in a ground-up chamber designed and built in collaboration with the team at the University of Nevada, Reno. The inception

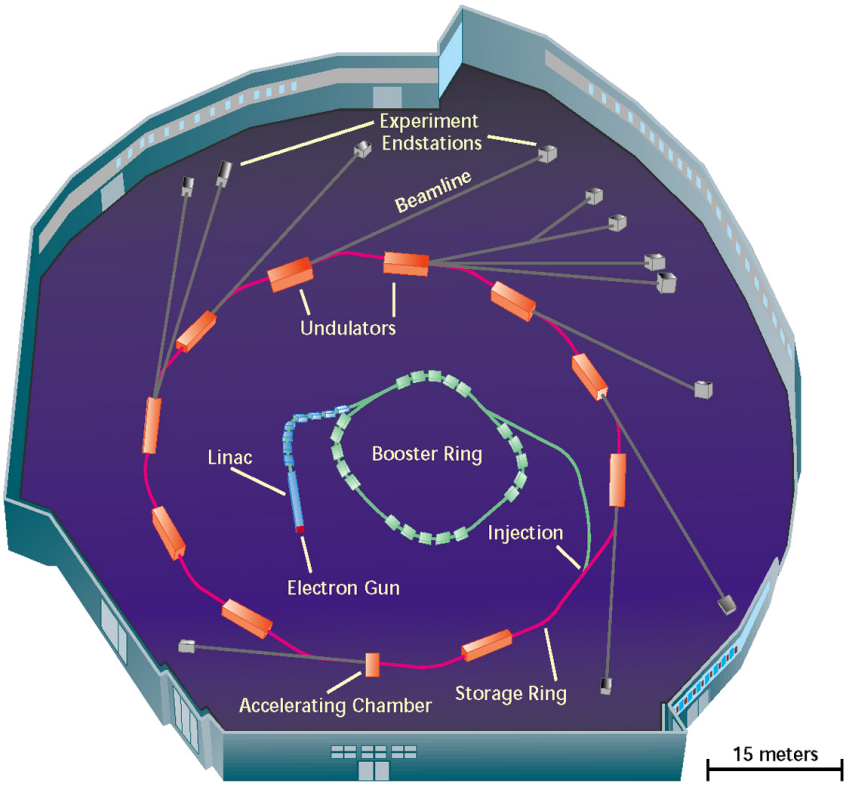

Figure 3.7: Schematic of the ALS floor, featuring the linear accelerator heading into the booster region before entering the storage ring.[42]

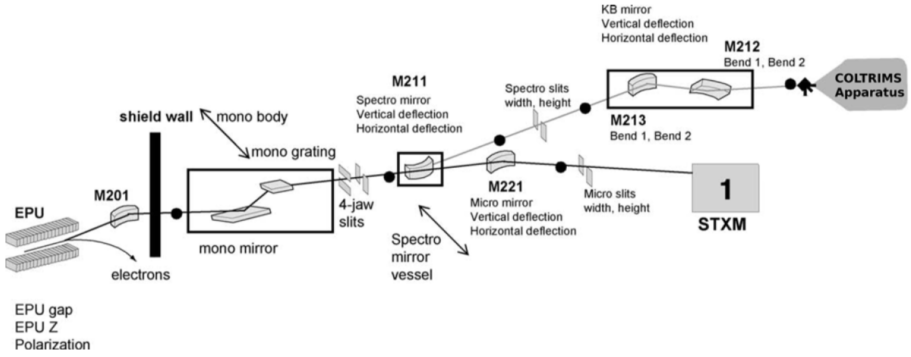

Figure 3.8: A typical Beamline schematic at the ALS coming off the storage ring, feeding into a COLTRIMS endstation.[39]

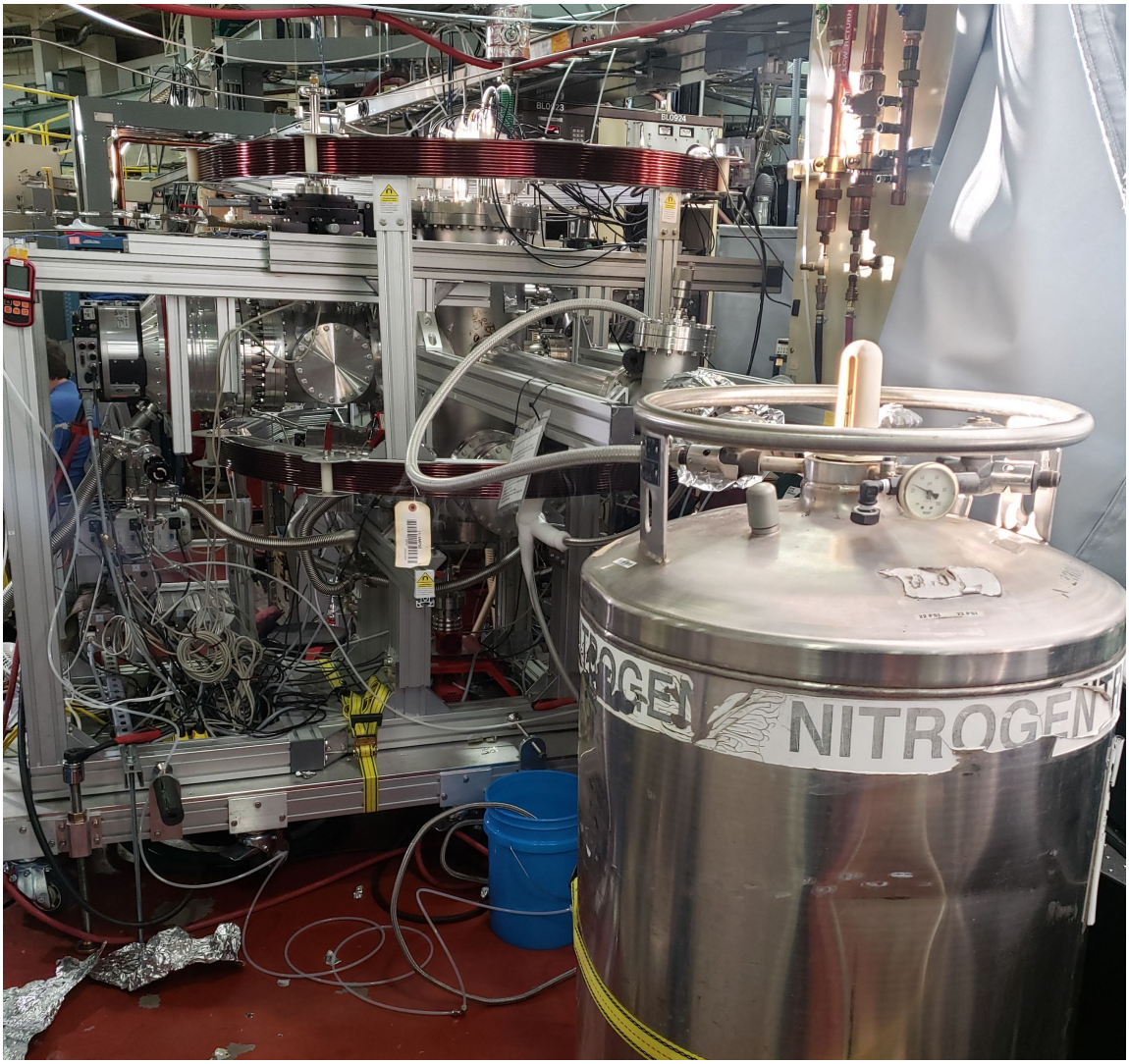

Figure 3.9: A photograph of the entire experimental chamber in-use at the ALS. Helmholtz-style coils in horizontal orientation encapsulate the vertical spectrometer housing, XUV photon source comes in perpendicular from behind the chamber. Liquid nitrogen dewar is onsite for cold-finger trap.

of the chamber came from the inspiration from our collaborators in Frankfurt, Germany at Goethe-Universitöt, Riedberg. The chamber is designed to be transported to various sites around the country, with the Advanced Light Source at LBNL being one of its primary

research locations. The chamber design will be broken up into several aspects, with detector and electronics, physical build and machining, and lastly, vacuum and jet systems. Although similar technology to the COLTRIMS chamber used for the DEA experiment in the previous chapters, there are key differences for this chamber, beginning with its initial design and configuration to be both portable and versatile for a wide range of collision physics. These differences will be the highlight of the following apparatus subsections to both explain the engineering and design challenges for photoionization experiments, as well as not to be redundant with the overlapping technology from the DEA experiment.

3.3.1 Spectrometer Array

The spectrometer array consists of two detectors, one for electrons and one for ions. This array is in the presence of both a magnetic field, as well as an electric field produced within the spectrometer region. The magnetic field is produced by large Helmholtz coils outside the chamber that were discussed in depth within Section 1.2.4. These coils produce a uniform field within the spectrometer region that runs parallel to the array, perpendicular to the accelerator plates. This allows for steering of the particles across the detector in a left-right orientation, allowing the electric field to accelerate and decelerate the particles towards the detector. Without the aid of the magnetic field, the particles would fly out of the spectrometer and fan away from the detectors. The magnetic field is tuned along with the electric field to ensure all particles reach the detector and are collected. Electrons that do not leave the interaction region parallel to the spectrometer are accelerated in a way

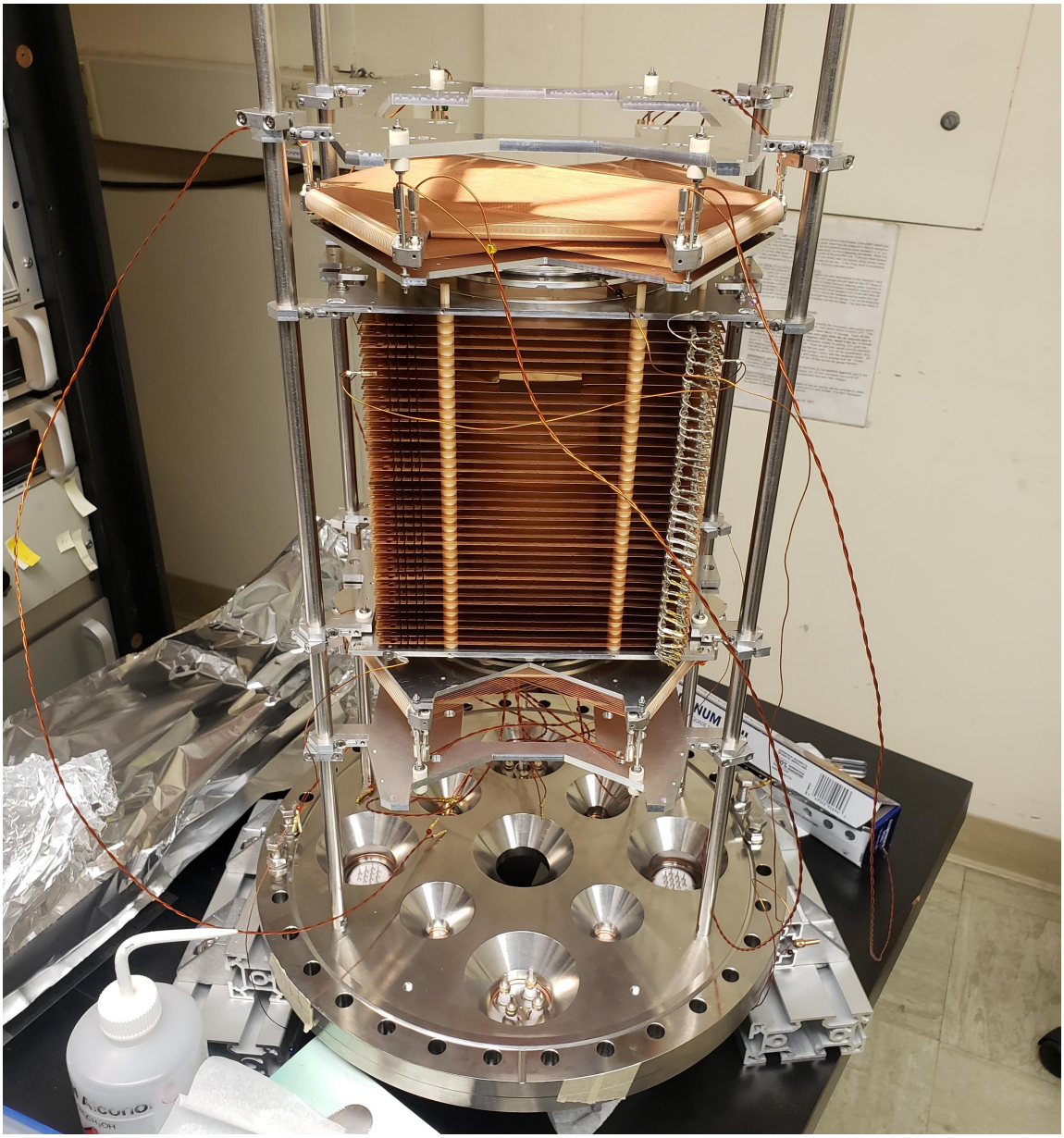

Figure 3.10: Inverted view of the spectrometer assembly. The anion Hexanode detector (bottom) captures the photoelectrons while the recoil ion Hexanode detector is on top. Also seen is the interaction region with the pusher plates for particle acceleration and drift. The entire assembly hangs off the twelve-inch flange (bottom) inside the chamber.

that follows the Lorentz force; in a helical trajectory as shown in the equation below:

$$\vec{F} = q[\vec{E} + (\vec{v} \times \vec{B})] \tag{3.9}$$

Since we ensure the magnetic field and electric field are parallel to each other, then their influence on the motion of charged particles can be treated separately. This is because the magnetic field induced Lorentz force is a vector product of the velocity along the electric field vector and the magnetic field vector, as seen in the derivation below. The magnetic force, F_B, contribution is not much to affect the acceleration of positive ions, but drives the much lighter electrons substantially. We can see this effect of this contribution to the Lorentz Force best within a cylindrical coordinate system (r, ϕ, z), with the axis of the spectrometer along the $\hat{z}$ axis. Thus, the electron follows some path along the spectrometer in the $\hat{z}$ axis, and can also fan out along the $\hat{r}$ axis:

$$\vec{v} = v_z\hat{z} + v_r\hat{r} \tag{3.10}$$

The magnetic field, B, acts along the axis of the spectrometer:

$$\vec{B} = B_z\hat{z} \tag{3.11}$$

The force felt by the electron of charge q due to the B field is F_B:

$$\vec{F}_B = -q(\vec{v} \times \vec{B}) \tag{3.12}$$

Which is a cross product between two vectors in cylindrical coordinates which results in:

$$\vec{F}_B = q \begin{bmatrix} \hat{r} & \hat{\phi} & \hat{z} \\ v_r & v_\phi & v_z \\ B_r & B_\phi & B_z \end{bmatrix} = \begin{bmatrix} \hat{r} & \hat{\phi} & \hat{z} \\ v_r & 0 & v_z \\ 0 & 0 & B_z \end{bmatrix} = 0 \cdot \hat{r} - v_{\mathrm{r}} B_{\mathrm{z}} \cdot \hat{\phi} + 0 \cdot \hat{z} = -v_{\mathrm{r}} B_{\mathrm{z}} \cdot \hat{\phi}$$

Here we see the F_B contribution in the $\hat{\phi}$ direction produces a velocity for the electrons also in the $\hat{\phi}$ axis. This also imparts a force along the $\hat{r}$ axis, which keeps the particles, specifically the lighter electrons, confined as they move to the detector. This is due to the $\vec{v} \times \vec{B}$ relationship from the Lorentz force and allows for the helical motion of the particles up to a gyroradius that is less than the detector maximum radius. Therefore, the particles enter a radial equilibrium from the $\vec{B}$ field's confinement, and a full 4π Solid angle (Ω) detector efficiency is achieved.

3.3.2 Particle Momentum

Now that we see forces acting on the particles, we must calculate the initial momentum of the particles, which was of great insight during the DEA experiment. The initial momentum is that immediately following ejection from the molecule, but before the electric and magnetic fields accelerate. By combining the two forces within the Lorentz force equation, we can break down the acceleration of the fragments:

$$\vec{F}_B = q(E_x \hat{x} + B_x v_z \hat{y} - B_x v_y \hat{z}) = m\vec{a} \tag{3.13}$$

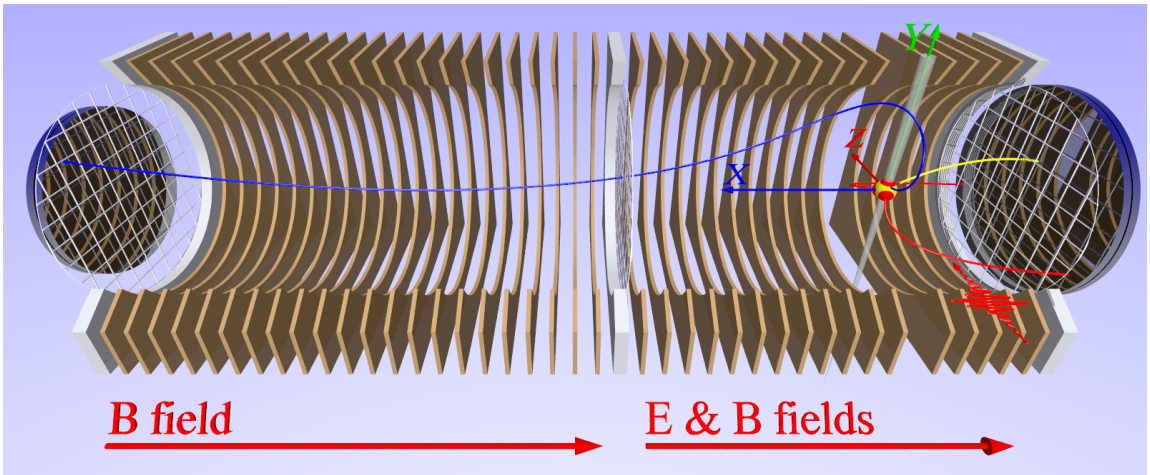

Figure 3.11: A side-view of the spectrometer, showing the paths of the fragments. The two ionic flight paths are represented in red and yellow, with the photoelectron shown in blue, going against the fields towards the electron detector. The spectrometer sits vertically in the COLTRIMS apparatus, with the electron detector at the top.

$$a_x\hat{x} = \frac{qE_x}{m}\hat{x}, \qquad a_y\hat{y} = \frac{qB_x}{m}v_z\hat{y}, \qquad a_z\hat{z} = \frac{qB_x}{m}v_y\hat{z} \tag{3.14}$$

Within Equation 3.14 it can be seen that if the fragment has an initial velocity in either the $\hat{y}$ or $\hat{z}$ direction, then it will be accelerated by the electric and magnetic fields, forming the helical trajectory discussed above. Now, to express the initial momentum, the time-dependent derivatives of the accelerators of Equation 3.14 can be calculated to glean the velocities:

$$\dot{v}_x\hat{x} = \frac{dv}{dt}\hat{x} = qE_x\hat{x} \tag{3.15}$$

$$\dot{v}_y\hat{y} = \frac{dv}{dt}\hat{x} = q\frac{B_y}{m}\hat{y} \tag{3.16}$$

$$\dot{v}_z\hat{y} = \frac{dv}{dt}\hat{x} = q\frac{B_z}{m}\hat{z} \tag{3.17}$$

Thus, the momentum of the fragments in terms of the time-of-flight, *TOF*, can be expressed along the direction of the acceleration region, in the *x-axis* via integrating Equation 3.15 with respect to time:

$$p_x = mv_x = m\int qE_x dt = \frac{m}{(TOF)}(\frac{qE_x}{2}(TOF)^2 + x) \tag{3.18}$$

Where *TOF* is the time of flight of the particle along the acceleration region, and *m* is the mass of the particular fragment. For the electrons following collisions, there is two acceleration regions and drift region. For the subsequent recoil ions, there is also two acceleration regions. Thus being able to calculate the forces at play and momenta for each fragment is pivotal in collecting accurate statistics. The perpendicular axes, *y* and *z*, are more tedious to calculate, and were calculating using a computer algebra system utilizing Newton's methods. These results are shown in Equations 3.19 and 3.20. The angular contribution for these two vectors indicate the helical trajectory we saw during the DEA experiment. This twisting is present but is again negligible due to the fragments being much heavier than the incoming photoelectron, resulting in a much lower initial velocity from the conservation of momentum. To visualize the path of the fragments, refer to Figure 3.11. These fragments consist of anion fragments similar to the DEA experiment, as well as ionic fragments known as "recoils" which then accelerate to their respective detector.

$$p_y = \frac{mw}{2}\left(y\,Cot\left(\frac{wt}{2}\right) - z\right) \tag{3.19}$$

$$p_z = \frac{mw}{2}\left(z\,Cot\left(\frac{wt}{2}\right) + y\right) \tag{3.20}$$

3.3.3 Signal Processing and Capture

Similar to the DEA experiment, timing is key when recording the molecular interactions. With a fixed timing grouping from the synchrotron source, it is important to adjust signal processing around this constant. As mentioned above, the ALS timing scheme operates on 2-Bunch mode, with packets arriving twice every rotation, or once every $328.28\,\mathrm{ns}$. Given this difference in the source timing scheme, it is worth while to address the differences in timing and signal processing and revisit the signal output of the detectors as a whole.

The pulse originates at t_0 = 0, and begins recording the time-of-flight for each of the particles. As with the single detector setup for DEA, the charged particles collide with the detector and trigger a cascade of electrons, changing the electrostatic potential of the MCP surface. This causes a drop and restore of voltage to the MCP via the power supplies, with this instantaneous current drop being measured as a pulse, indicating a time and position event. This time event is known as the t_{MCP}. In order to accurately record this time, a Delay Line Anode (DLA) is again used. Pulses travel in each direction of the twin DLA wire pair layers, with the travel velocity given by the following equation:

$$v_{signal} = \frac{length}{t_1 + t_2} \tag{3.21}$$

where "length" is the fixed length of the wire pair across the DLA, with t_1 and t_2 being the respective arrival times from each wire exiting the DLA. Next, we can calculate the position array across the detector itself for each wire, given that the signal velocity, v_{signal} is fixed:

$$x_1 = v_{signal} \cdot t_1 \tag{3.22}$$

$$x_2 = v_{signal} \cdot t_2 \tag{3.23}$$

Thus, when subtracted, we can find a location on the detector in "x" that identifies the fragment's position in that dimension.

$$x = v_{signal} \cdot (x_1 - x_2) \tag{3.24}$$

This same concept is implemented for the "y" direction, as well as for the second detector. All of these measured pulses, along with the trigger signal is fed into an array of digital signal processors, as highlighted in the figure. These MCP and DLA signals are passed through into Nuclear Instrumentation Module (NIM) signal processing units, to form digital pulses that are usable for the acquisition computer. Before reaching the TDC card, a CFD is again used to combat the fact that the pulse sizes from the DLA are not normalized. This introduces noise into the event and the possibly of discarding good events. The CFD solves this by taking the uneven pulses, splits them into two pulses, inverts one, delays it by a specific amount, and then recombines the two pulses back into one. Refer to Figure 1.16 for a diagram of this process. After the pulses pass into the TDC, the researcher is left with time and position data, as well as specific electric and magnetic field values. This

data allows for the full three-dimensional momentum and kinetic energy to be calculated, aiding in the reconstruction of the target molecule.

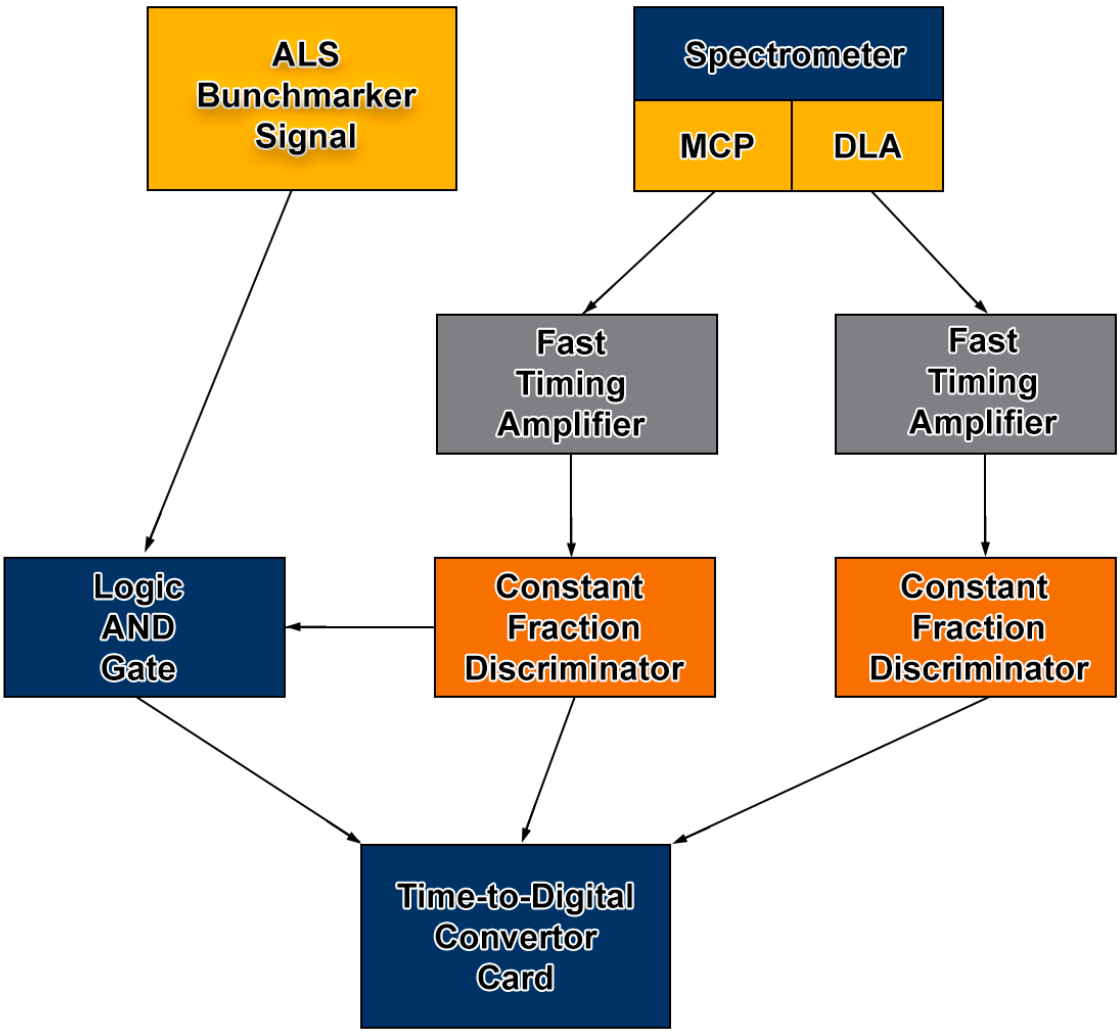

Figure 3.12: ALS Signal Processing Flowchart, showing the MCP and DLA pulses being modulated and referenced off the ALS Bunchmarker signal before being converted to a recorded event.

Chapter 4

NH_3 Molecule Analysis and Results

The chosen species for this experiment, Ammonia NH_3, helps to reveal the role and style of non-adiabatic transitions for select multi-body breakups experimentally. Previously, the focus of photoionization on Ammonia molecules was on the energies of the various states,[40] with little focus on non-adiabatic dynamics following ionization. This chapter will focus on preliminary findings of photoionization and dissociative dynamics of the various channels of neutral NH_3 molecules upon single-photon double ionization. This experiment was conducted using soft X-ray light with an energy level of 61.54eV, where the two photo-electrons and two cations were measured in coincidence using 3-D momentum imaging. For the ground state of Ammonia, the electron configuration is given as:

$$(1a_1)^2(2a_1)^2(1e)^4(3a_1)^2 \tag{4.1}$$

For our photon energy of 61.54eV following double photoionization, there are nine dication electronic states that are energetically accessible. Four of which belong to one of the two measured channels and will be of greater focus for the results of this experiment.

4.1 Calibration and Channel Selection

Following the discussion of the Ammonia molecule's breakup channels, we have focused on two specific channels: a two-body case involving a single Hydrogen anion, H^+, and a positively charged $NH_2{}^+$, coupled with two photo-electrons stemming from the double photoionization. The other channel, a three-body, features two Hydrogen anions, H^+ and H^+, as well as a neutral NH fragment, along with the two photo-electrons. It is worth noting the naming scheme of two-body and three-body for channel selection directly refer to the fragments of the Ammonia molecule, ignoring the presence of the dual photo-electrons although they are measured for momentum conservation and kinetic energy release (KER) results. These channels were discussed back in Chapter 3 via Equation 3.2,

which observed five different photoion-photoion coincidence features following double photoionization. Shown again below for the reader's aid:

$$\gamma + \mathrm{NH_3} \longrightarrow {\mathrm{NH_3}}^{2+*} + 2\,\mathrm{e}^-_\gamma \begin{cases} \rightarrow \mathbf{NH_2^+ + H^+ + 2\,e^-} & \text{(4.2a)} \\ \rightarrow \mathrm{NH^+ + H^+ + H + 2\,e^-} & \text{(4.2b)} \\ \rightarrow \mathrm{N^+ + H^+ + H_2 + 2\,e^-} & \text{(4.2c)} \\ \rightarrow \mathrm{NH^+ + H_2^+ + 2\,e^-} & \text{(4.2d)} \\ \rightarrow \mathbf{NH + H^+ + H^+ + 2\,e^-} & \text{(4.2e)} \end{cases}$$

The equations in bold, 4.2a and 4.2e, are the channels of focus for this portion of the thesis, namely the two-body and three-body channels discussed above. It is worth noting all breakup channels consists of dual photoelectrons, as the result the single-photon double-ionization (PDI) that occurred in the collision. These two anions are measured on the negative ion detector and brought together with the ion detector data during the recombination in post-capture analysis.

4.1.1 Measurement of Physical Properties

Before any histograms can be made pertaining to the molecular breakup, some physical quantities must be calculated from the raw signal data during acquisition. The first, and often the most important, is the vector momentum information for a specific channel. This is calculated partially automatically via LMF2ROOT, but also manually with custom

coding, see **Appendix C**. This involves using the fixed masses of the fragments, coupled with the *TOF* dataset, taking into account the helical trajectory. These vector momentum formula was discussed in the previous chapter beginning with Equation 3.18. Next, the kinetic energy of each particle can be calculated and passed on as a captured quantity for further analysis. This is done via fundamental physics, invoking the dot product of the two momentum vectors:

$$KE = \frac{\vec{p} \bullet \vec{p}}{2m} \tag{4.3}$$

The angle between the momentum vectors can be calculated with the Law of Cosines:

$$\vec{p_1} \bullet \vec{p_2} = |p_1||p_2| \cdot \cos(\theta) \tag{4.4}$$

With these somewhat trivial calculations out of the way, further analysis work can be done referring these physical quantities for more complex plotting such as recoil and polarization frames.

4.2 Results

Following the capture of this data, and proper calibration within LMF2ROOT, we can now analyze the results of the dataset. The three-dimensional momentum and angular distributions of the fragments were studied, as well as their energies and any interplay and symmetry between these parameters were carefully examined and cross-referenced to existing work. These results will be done in a preliminary state, presenting the information

currently known. Further work is required for a complete picture of this molecular process. That stated, we can progress into analyzing the channels stemming from the PDI process.

4.2.1 Channels

The two channels discussed above will be presented independently in this chapter, with particular focus spent on each. The two main channels of focus are the "three body case" and "two body case," with either a single proton or dual protons measured on the recoil ion detector.

Two Body Breakup

The first channel, tagged the two-body breakup, refers to the pathway seen in Equation 4.2a, and produces a single Hydrogen ion, H^+, along with a heavier $NH_2{}^+$ ion. These ions of unequal mass are easily distinguishable on a PIPICO plot due to the difference in the *time-of-flight*. This can be seen in Figure 4.1, with the two-body case in red highlighted with the most statistics. The heavier ion, namely the $NH_2{}^+$, arrives around 2500ns with the lighter proton arriving much sooner at around 500ns. This gives a direction for *TOF* gating when calculating momentum and energy figures for this channel. At the writing of this thesis, the two-body channel lacked the statistics found in the three-body breakup channel and was only aligned and momentum-calibrated for the current dataset.

Three Body Breakup

The second channel of focus, the three-body breakup, refers to the pathway seen in Equation 4.2e, and produces dual protons, H^+ and H^+, along with a neutral NH that we do

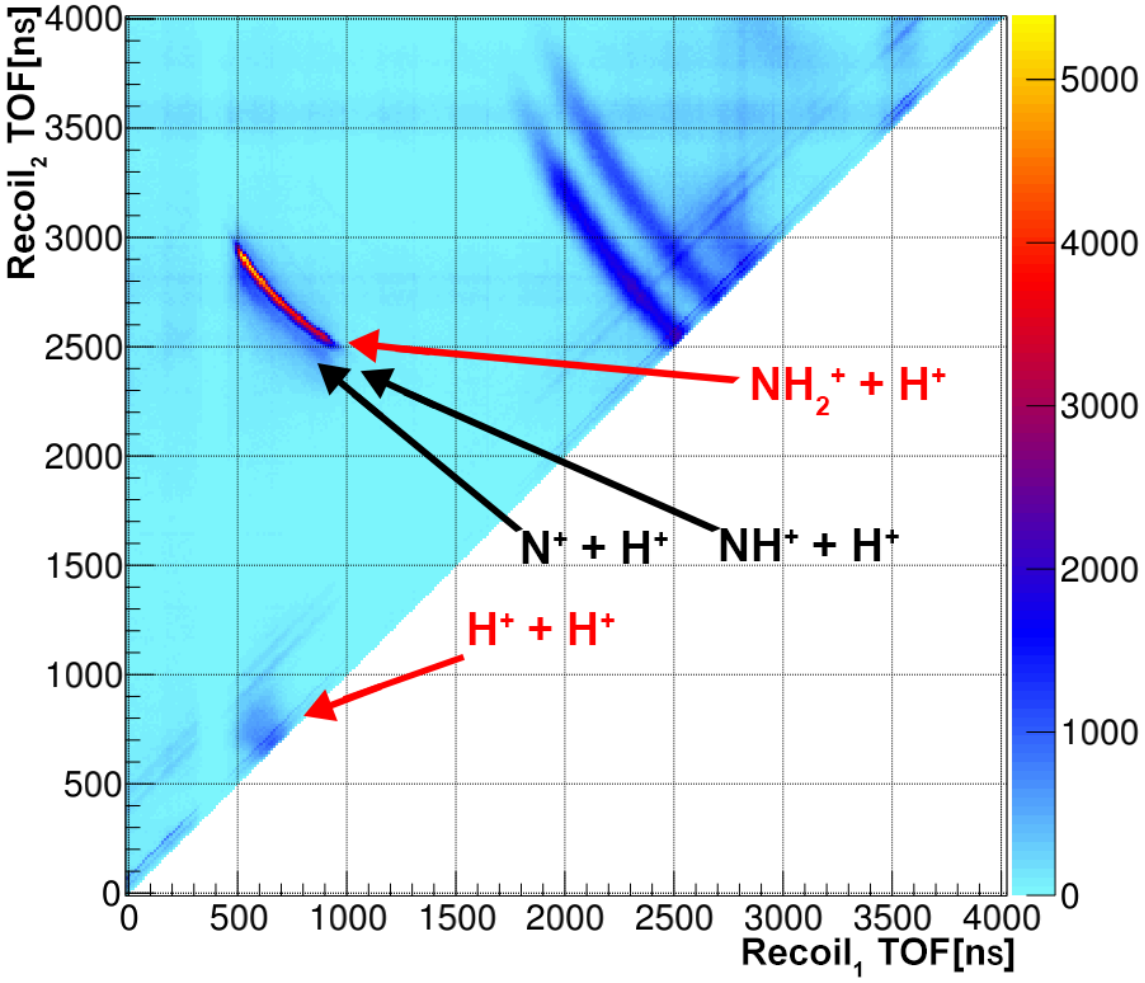

Figure 4.1: A high pass PIPICO with all visible channels present. Due to capture rate and yield, we are focusing on the two channels shown in red. Gates were placed around these *TOF's* to identify the specific channels in presorting.

not measure in the experiment. These identical protons will of course have identical *time-of-flight* values, and will show as a point spread rather than a fitted curve on the PIPICO. This channel yielded the most information in the theoretical report, as it produced four of the nine energetically accessible states following dissociation. To findings of these singlet and triplet states came from theoretical calculations first reported by one of our collaborators, Larsen *et al*[53,54] at the University of California, Berkeley, and identified the following dication states within this three-body breakup channel.

States

The four dication states found for the three-body channel consist of three singlets: $(1e^{-2})^1A_1$, $(2a_1^{-1}, 3a_1^{-1})^1A_1$, $(1e^{-2})^1E$, along with a triplet state: $(1e^{-2})^3A_2$. These four dications, along with their vertical energies, will be a driving force for matching our experimental energy plots for accuracy. Each state is based of C_{3v} symmetry, and below is a table of vertical and adiabatic limit energies for these states, as produced by Larsen *et al*.[53,54] Using the theoretical vertical energies from the above table, a histogram of

Table 4.1: Ammonia dication vertical energies at neutral NH_3 geometry and asymptotic three-body limits as reported by Larsen *et al*.

State	Vertical Energy (eV)	Adiabatic Limit Energy (eV)
$(1e^{-2})^3A_2$	8.64	0.96
$(1e^{-2})^1E$	9.94	0.52
$(1e^{-2})^1A_1$	11.94	2.69, 3.74*
$(2a_1^{-1}, 3a_1^{-1})^1A_1$	18.94	3.74

*Theoretical calculations suggest that two different possible asymptotic limits exist for this state.

proton energy difference verses electron energy sum was plotted, with state identification performed to align with the theory. This plot is constructed by taking the two recoil ion energy difference plotted along the dependant axis, verses the two photoelectrons summed together on the independent axis. This allows for clear energy island identifications, see Figure 4.2. Now armed with this cross-particle plot, similar state energy identifiers were overlaid to the specific dual photoelectron and dual proton histograms, see Figures 4.3 and 4.4. These energy plots are overlaid with the four dication states identified above. Given that the photoelectrons are indistinguishable, we see smooth features across the diagonally with state selected lines matching up nicely. For the recoil ion plot, we again are dealing with equal and indistinguishable particles, and when analysing the state selection, we see three of the dication states, namely $(1e^{-2})^3A_2$, (green), $(1e^{-2})^1A_1$, (purple), and $(2a_1^{-1}, 3a_1^{-1})^1A_1$, (orange) all exhibit equal energy sharing between protons, indicative of a direct breakup mechanism, and agrees with prior measurements.[53] However, the final state within this three-body channel, $(1e^{-2})^1E$, (teal), seems to exhibit extremely unequal energy sharing, with heavy emphasis on one proton over the other. This agrees with a sequential breakup mechanism; something first suggested in PDI of NH_3 to the $H^+ + H^+$ channel by M Stankiewicz *et al* but was unable to confirm.[55]

4.2.2 Ammonia Analysis Summery

The end goal of understanding this breakup path as well as the PDI of NH_3 lies within analysing and understanding the Molecular Frame Photoelectron Angular Distributions, or MFPADs, in three dimensions. This type of angular distribution require accurate orientation of the molecule and a high level of accuracy of the momentum data as well as angular

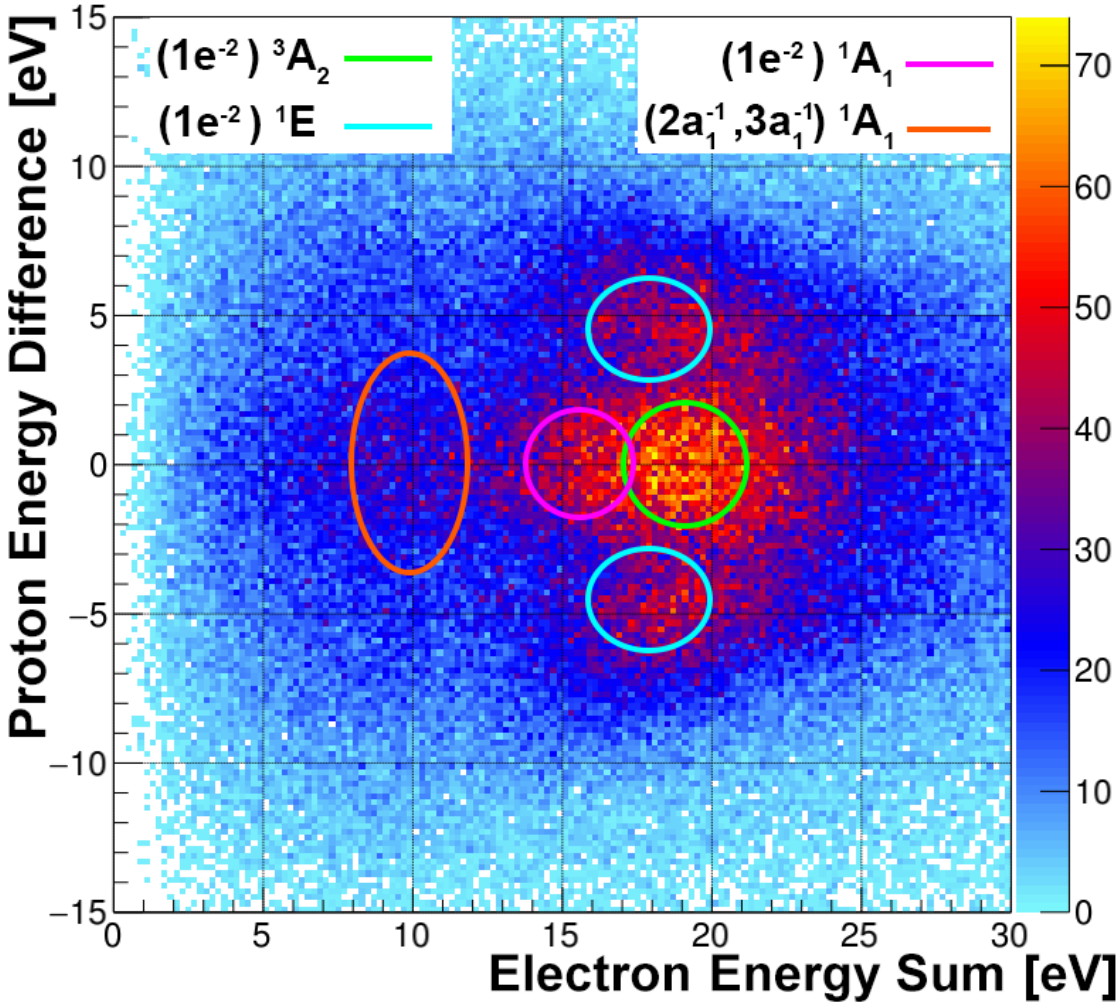

Figure 4.2: The yield of H^+ + H^+ following PDI of NH_3 as a function of the energy difference of the proton pair and the energy sum of the photoelectron pair. Although there is no physical meaning to the order in which the two protons are detected, the plot is not mirrored about the zero proton energy difference in an effort to display proper calibration and capture techniques.

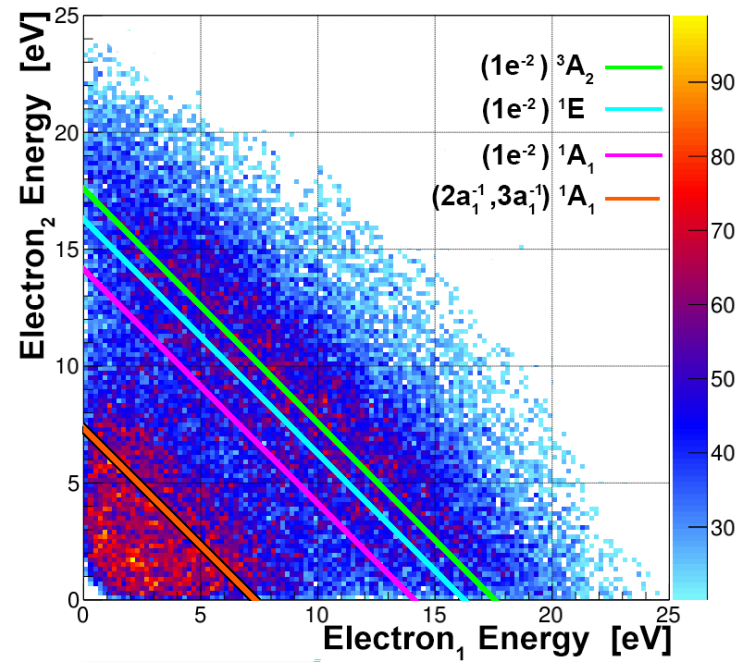

Figure 4.3: Electron-Electron Energy plot with dication states overlaid.

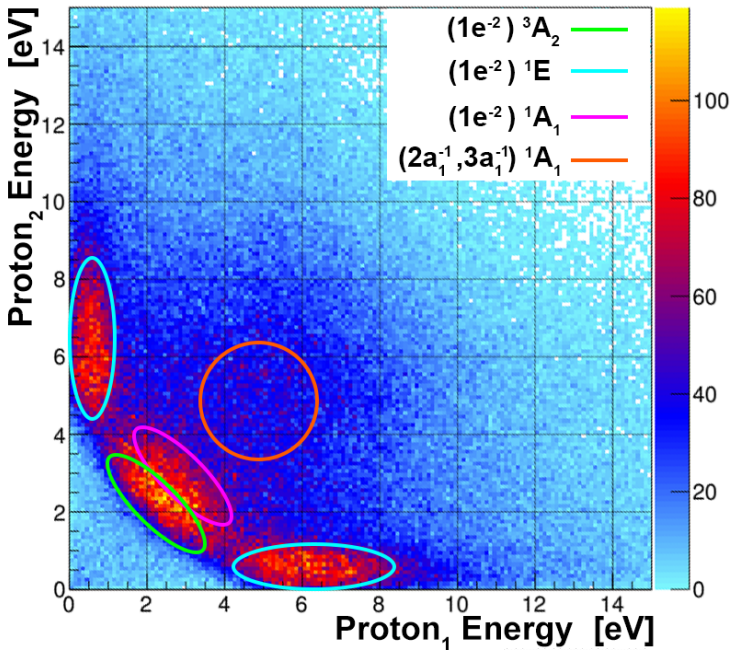

Figure 4.4: Proton-Proton Energy plot with dication states overlaid.

data of the fragments following dissociation. This makes COLTRIMS such an excellent tool for this type of research over velocity sliced imaging techniques, which was tried in prior experiments[55] and isolates the angular dependence in one plane, and does not capture the entire solid angle. COLTRIMS is capable of measuring 3D momentum vectors of each

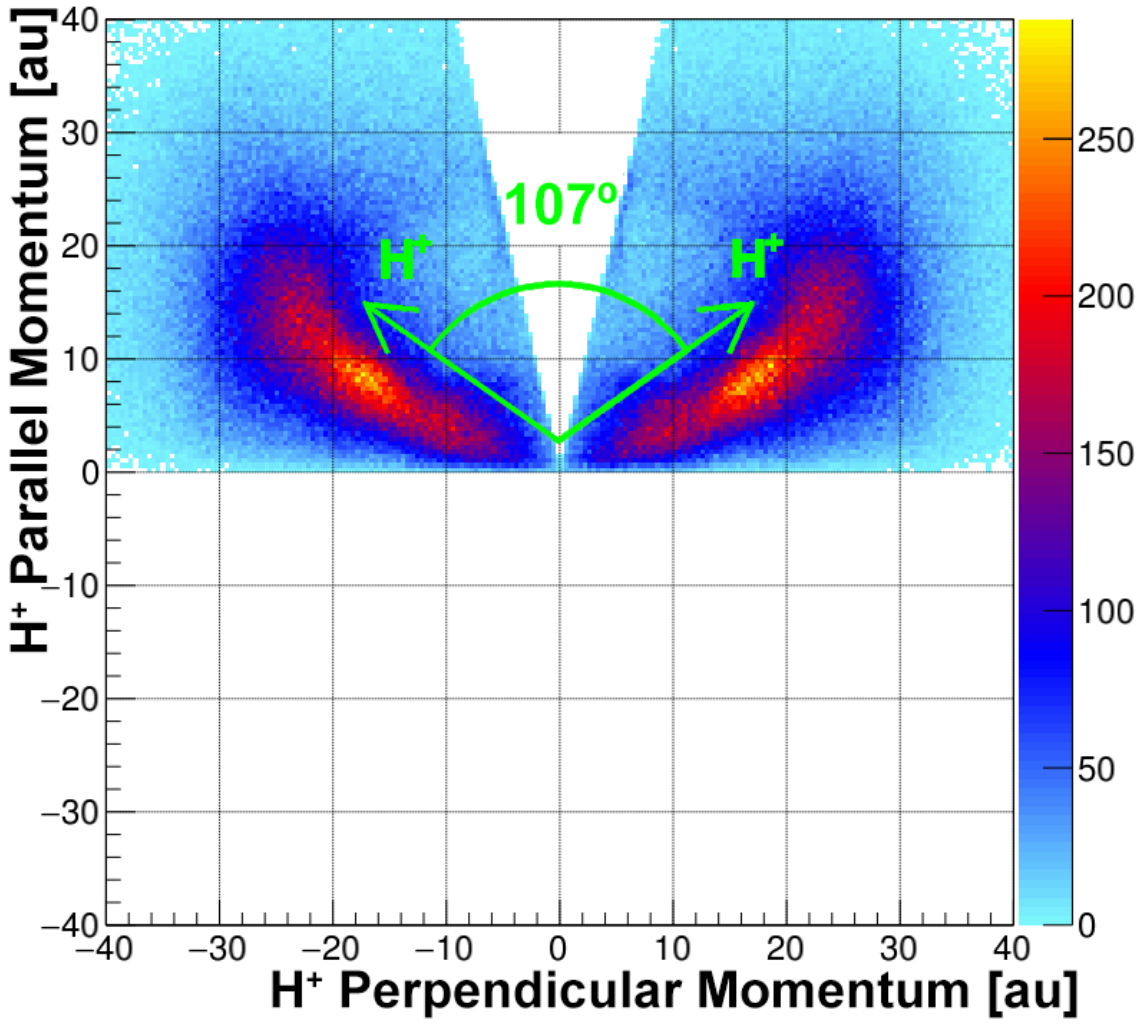

Figure 4.5: Ejected recoil ion momenta plotted in a parallel and perpendicular frame to the momentum sum. Gate were placed around the two islands for an additional level of background noise elimination.

and every charged particle created from the ionization event, allowing for electron correlation, a vastly important concept for molecular physics. A first step was to create body plots of the two protons; to ensure bond angle and properly define the vector components both perpendicular and parallel to the momentum sum. See Figure 4.5. Next, careful gating was used around both the proton energies as well as the two photoelectrons for state selection. Following the PDI process, it has been seen that for equal energy sharing, as is the case for the $(1e^{-2})^3A_2$, (green), $(1e^{-2})^1A_1$, (purple), and $(2a_1^{-1}, 3a_1^{-1})^1A_1$, (orange) states, along with holding the first detected electron fixed along the polarized vector, that extreme anisotropic behavior is observed.[53,57] However, for our three equal energy sharing states, we are seeing isotropic behavior for the emission angle between photoelectrons. This behavior has prevented further plotting of these states until the isotropic angular behavior is resolved. Nevertheless, histograms highlighting this response in order to provide information for future experimental development on this molecule. For an example, the $(2a_1^{-1}, 3a_1^{-1})^1A_1$ dication state is shown for the isotropic activity, with similar results exist for the other two states exhibiting equal energy sharing conditions. However, the forth state, corresponding to the identity *E* point group symmetry, exists unequal energy sharing and should display isotropic tendencies. This was seen in a similar momentum perpendicular verses parallel photoelectron plot. Additional work must be done along this channel as well as the two-body case before final results are indisputable.

A variation on the MFPAD is to construct a similar heatmap of the polarization axis in the molecular frame, identifying the orientation of the molecule relative to the light source at the time of dissociation. This was partially performed for the $(1e^{-2})^1E$ dication state, with preliminary results on the following page. Given the semi-success of the

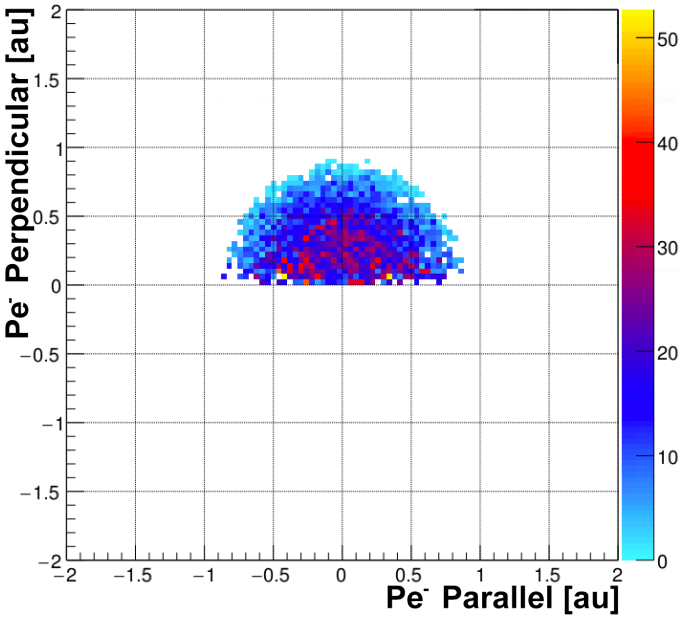

Figure 4.6: Highly isotropic momenta within the $(2a_1^{-1}, 3a_1^{-1})^1 A_1$ dication state with equal energy sharing. We expected anisotropic behavior with tendencies between $90°$ and $180°$ due to selection rules.

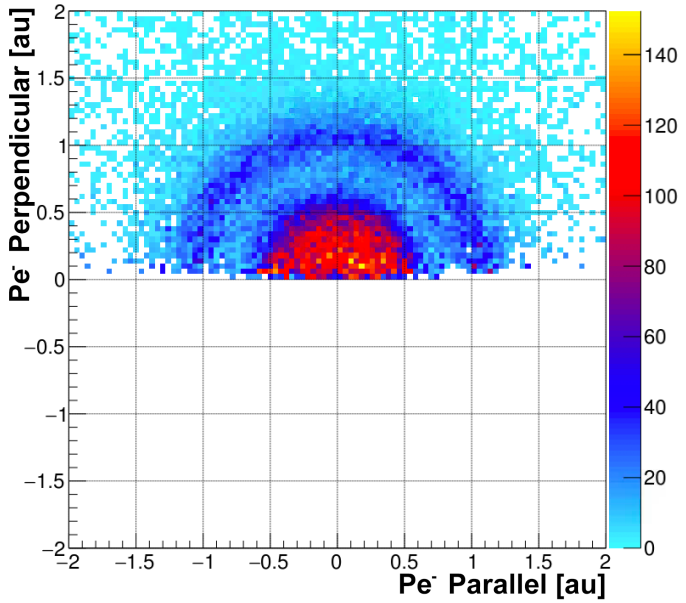

Figure 4.7: Highly isotropic momenta within the $(1e^{-2})^1 E$ dication state featuring unequal energy sharing, as expected.

identity ^1E state, we present preliminary MFPADs as raw outputs. According to previous theory and experimental measurements,,[48,53,54] relative angle between the electrons should be isotropic with peaks at 0° and 180°, along with a symmetric molecular frame photoelectron angular distribution. Currently, we see a striking asymmetry within the MFPADs, a discrepancy that is to be addressed before proceeding with analysis of this breakup channel. See Figure 4.8.

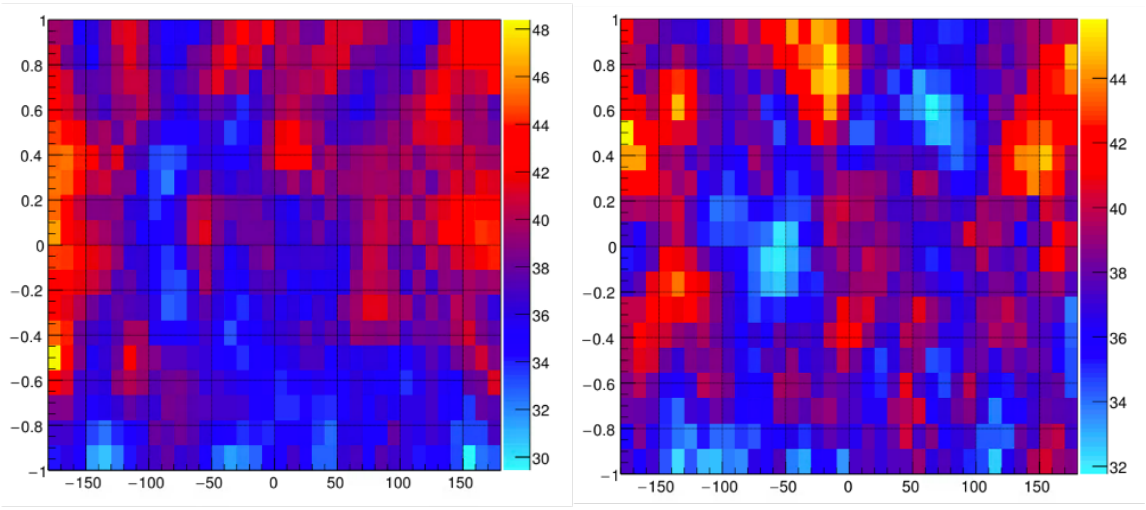

(a) First Electron

(b) Second Electron

(c) First Proton

(d) Second Proton

Figure 4.8: MFPADs of the electrons and protons for the $(1e^{-2})^1E$ state. Extreme asymmetry is present and currently does not align with previous experiments.

4.3 Future Work

Following the preliminary results for the above channels, specific care must be given for the next steps of analysis. For the three-body case, armed with an understanding of the dication states, the next steps are to revisit the three equal energy states and delve into the problem of isotropic emission angles. Once this is resolved, the group wishes to proceed along these four states and produce proper MFPADs for each dication state as well as KER verses proton-proton angle histograms, another indicator of a concerted dissociation pathway for the equal energy sharing and a sequential pathway for the single unequal identity state. This, coupled with extending the MFPAD work for the $(1e^{-2})^1E$ state will yield a complete resolution of the molecule following double photoionization and the corresponding recoil ion fragments. Along with our collaborators at Lawrence Berkeley National Laboratory, as well as theoretical support from the group at the University of California, Berkeley, we anticipate a resolution to the above issues with a more complete understanding regarding the PDI process in the NH_3 molecule for publication.

Bibliography

[1] L. G. Christophorou, R. N. Compton, and H. W. Dickson. Dissociative electron attachment to hydrogen halides and their deuterated analogs. *The Journal of Chemical Physics*, 48(5):1949–1955, 1968.

[2] L. G. Christophorou, J. K. Olthoff, and M. V. V. S. Rao. Electron interactions with CF_4. *Journal of Physical and Chemical Reference Data*, 25(5):1341–1388, 1996.

[3] Y. Le Coat, J.-P. Ziesel, and J.-P. Guillotin. Negative ion resonances in CF_4 probed by dissociative electron attachment *J. Phys. B: Atomic Molecular Optical Physics*, 27:(965), 1994.

[4] Vernon H. Dibeler and Fred L. Mohler. Dissociation of SF_6, CF_4, and SiF_4 by electron impact. *Journal of Research of the National Bureau of Standards*, 40(1):25, January 1948.

[5] F. H. Dorman. First differential ionization efficiency curves for fragment ions by electron impact. *The Journal of Chemical Physics*, 44(1):35–38, 1966.

[6] R. Dörner, V. Mergel, O. Jagutzki, L. Spielberger, J. Ullrich, R. Moshammer, and H. Schmidt-Bócking. *The European Physical Journal D.*, 66(2), 2012.

[7] F. A. Gianturco, R. R. Lucchese, and N. Sanna. Calculation of low-energy elastic cross sections for electron CF_4 scattering. *The Journal of Chemical Physics*, 100(9):6464–6471, 1994.

[8] Jiande Gu, Jing Wang, and Jerzy Leszczynski. Electron attachment-induced dna single strand breaks: $C_{3'}$-$O_{3'}$ σ-bond breaking of pyrimidine nucleotides predominates. *Journal of the American Chemical Society*, 128(29):9322–9323, 2006. PMID: 16848454.

[9] P.W. Harland and J.L. Franklin. Partitioning of excess energy in dissociative resonance capture processes. *Journal of Chemical Physics*, (61):1621, 1974.

[10] S. R. Hunter, J. G. Carter, and L. G. Christophorou. Electron attachment and ionization processes in CF_4, C_2F_6, C_3F_8, and $n-C_4F_{10}$. *The Journal of Chemical Physics*, 86(2):693–703, January 1987.

[11] CoboldPC 2011 R5.2. *RoentDek Handels GmbH*. Kelkheim, Germany. 2011.

[12] CRC Handbook of Chemistry and Physics. Cleveland, Ohio. CRC Press, 1977.

[13] E. Illenberger. Measurement of the translation excess energy in dissociative electron attachment processes. *Chemical Physics Letters*, 80(1):153-158, 1981.

[14] R. K. Jones. Absolute total cross sections for the scattering of low energy electrons by CCl_4, CCl_3F, CCl_2F_2, $CClF_3$, and CF_4. *The Journal of Chemical Physics*, 84(2):813–819, 1986.

[15] G. Khorsandgolchin, L. Sanche, P. Cloutier, and J. R. Wagner. Strand breaks induced by very low energy electrons: Product analysis and mechanistic insight into the reaction with TpT. *Journal of the American Chemical Society*, 141(26):10315–10323, 2019.

[16] K.A.G. Macneil and J.C.J. Thynne. The formation of negative ions by electron impact on silicon tetrafluoride and carbon tetrafluoride. *International Journal of Mass Spectrometry and Ion Physics*, 3(6):455 – 464, 1970.

[17] C. E. Melton. Cross sections and interpretation of dissociative attachment reactions producing OH^-, O^-, and H^- in H_2O. *The Journal of Chemical Physics*, 57(10):4218–4225, 1972.

[18] P. M. Mendes, S. Jacke, K. Critchley, J. Plaza, Y. Chen, K. Nikitin, R. E. Palmer, J. A. Preece, S. D. Evans, and D. Fitzmaurice. Gold nanoparticle patterning of silicon wafers using chemical e-beam lithography. *Langmuir*, 20(9):3766–3768, 2004.

[19] A. Moradmand, D. S. Slaughter, A. L. Landers, and M. Fogle. Dissociative-electron-attachment dynamics near the 8eV Feshbach resonance of CO_2. *Physical Review A*, 88(2), August 2013.

[20] A. Moradmand, J. Williams, A. Landers, and M. Fogle. Momentum-imaging apparatus for the study of dissociative electron attachment dynamics. *Rev. Sci. Instrum*, 84(033104), 2013.

[21] W.L. Morgan. Electron collision data for plasma chemistry modeling. *Fundamentals of Plasma Chemistry. Series: Advances In Atomic, Molecular, and Optical Physics.*, 43:79-110, Academic Press, 2000.

[22] F. H. Ómarsson, N. J. Mason, E. Krishnakumar, and O. Ingólfsson. Dissociative electron attachment to CF_4 probed by velocity slice imaging. *The European Physical Journal D.*, 66(2), 2012.

[23] F. H. Ómarsson, E. Szymańska, N. J. Mason, E. Krishnakumar, and O. Ingólfsson. Velocity slice imaging study on dissociative electron attachment to CF_4. *The European Physical Journal D.*, 68(101), 2014,

[24] F. H. Ómarsson, E. Szymanska, N. J. Mason, E. Krishnakumar, and O. Ingólfsson. Quantum superposition of target and product states in reactive electron scattering from CF_4 revealed through velocity slice imaging. *Physical Review Letters*, 111:063201, 2013.

[25] H.-U. Scheunemann, M. Heni, E. Illenberger, H. Baumgärtel, and B. Bungenges. Dissociative attachment and ion pair formation in CF_4, CHF_3, CH_2F_2, and CH_3F under low energy (0 – 20eV) electron impact. *The Journal of Chemical Physics.*, 86(321), 1982.

[26] G. J. Schulz. Excitation and negative ions in H_2O. *The Journal of Chemical Physics*, 33(6):1661-1665, 1960.

[27] S Trajmar and R I Hall. Dissociative electron attachment in H_2O and D_2O: energy and angular distribution of *h*-and *d*-fragments. *Journal of Physics B: Atomic and Molecular Physics*, 7(16):458-461, 1974.

[28] J. Ullrich, R. Moshammer, A. Dorn, R. Dörner, L.P.H. Schmidt, and H. Schmidt-BÖcking. Recoil-ion and electron momentum spectroscopy: reaction-microscopes. *Reports on Progress in Physics.*, 66(1463), 2003.

[29] H. F. Winters and M. Inokuti. Total dissociation cross section of CF_4 and other fluoroalkanes for electron impact. *Physical Review A.*, 25:1420-1430, 1982.

[30] L. Xia, X.-J. Zeng, H.-K. Li, B. Wu, and S. X. Tain. Orientation effect in the low-energy electron attachment to the apolar carbon tetrafluoride molecule *Angew. Chem. Int. Ed.*, 52(1013), 2013.

[31] B. Wu, L. Xia, H. K. Li, X. J. Zeng, and S. X. Tian. Positive/negative ion velocity mapping apparatus for electron-molecule reactions *Rev. Sci. Instrum*. 83(1):013108, 2012.

[32] F. H. Read. Angular distributions for resonant scattering of electrons by molecules. *J. Phys. B: Atomic Molecular Optical Physics*. 893(1) 1968

[33] R.M. Fristrom, *Flame Structure and Processes*, Oxford Univ. Press, New York, 1995.

[34] M. Tronc, F. Fiquet-Fayard, C. Schermann, and R. I. Hall. Angular distributions of O^- from dissociative electron attachment to N_2O between 1.9 to 2.9eV. *J. Phys. B: Atomic Molecular Optical Physics*. 10:459, 1977.

[35] S. Şentürk. "Enlarged Ionization Region and Wiley-McLaren Type Geometry." *Mathematical & Computational Applications* 10:133-138, 2005.

[36] R. Döner, V. Mergel, O. Jagutzki, L. Spielberger, J. Ullrich, R. Moshammer, and H. Schmidt-Böcking. Cold target recoil ion momentum spectroscopy: a momentum microscope to view atomic collision dynamics. *Physics Reports*, 330(23):82–145, 2000.

[37] D. Nandi, V. S. Prabhudesai, E. Krishnakumar, and A. Chatterjee, Velocity slice imaging for dissociative electron attachment. *Rev. Sci. Instrum*. 76:053107, 2005.

[38] A. Moradmand. 2013, 'Imaging Electron-Driven Dynamics in Dissociative Electron Attachment to Gas Molecules', Ph.D Thesis, Auburn University, Auburn.

[39] J. B. Williams. 2011, 'Imaging Polyatomic Molecules in Three Dimensions Using Molecular Frame Photoelectron Angular Distributions', Ph.D Thesis, Auburn University, Auburn.

[40] W. J. Griffiths and F. M. Harris. An experimental determination of the energy of the first triplet doubly-ionized state of ammonia. *Rapid Communications in Mass Spectrometry*, 4(10):366-368, 1990.

[41] R. Wehlitz. Double photoionization of hydrocarbons and aromatic molecules. *J. Phys. B: Atomic Molecular Optical Physics*, 49:222004, 2016.

[42] Advanced Light Source at LBL. URL https://als.lbl.gov/.

[43] *MCP Delay Line Detector Manual (Version 11.0.2102.1)*, RoentDek Handels GmbH, Frankfurt, Germany, 2017.

[44] J. L. Wiza. Microchannel plate detectors. *Nuclear Instruments and Methods in Physics Research*, 162(3):587-601, 1979.

[45] A. Czasch, T. Jahnke, and M. Shoeffler, "LMF2ROOT Version 1.6" (2008–2013).

[46] V. Mergel, M. Achler, R. Dörner, K. Khayyat, T. Kambara, Y. Awaya, V. Zoran, B. Nyström, L. Spielberger, J. H. McGuire, J. Feagin, J. Berakdar, Y. Azuma, and H. Schmidt-Böcking, Helicity dependence of the photon-induced three-body coulomb fragmentation of helium investigated by cold target recoil ion momentum spectroscopy. *Physical Review Letters.*. 80:5301, 1998.

[47] C. W. McCurdy, D. A. Horner, T. N. Rescigno, and F. Martìn, Theoretical treatment of double photoionization of helium using a *B*-spline implementation of exterior complex scaling. *Phys. Rev. A* 69:032707, 2004.

[48] A. E. Orel, T.N. Rescigno, Photoionization of ammonia. *Chemical Physics Letters*, 269(3):222-226, 1997.

[49] W. Vanroose, F. Martìn, T. N. Rescigno, and C. W. McCurdy. Nonperturbative theory of double photoionization of the hydrogen molecule. *Phys. Rev. A*, 70(5):050703, 2004.

[50] F. L. Yip, T. N. Rescigno, C. W. McCurdy, and F. Martìın, Fully differential single-photon double ionization of neon and argon. *Physical Review Letters*, 110:173001, 2013.

[51] T. Weber, A. Czasch, O. Jagutzki, A. Müller, V. Mergel, A. Kheifets, J. Feagin, E. Rotenberg, G. Meigs, M. H. Prior, S. Daveau, A. L. Landers, C. L. Cocke, T.

Osipov, H. Schmidt-Böcking, and R. Dörner. Fully differential cross sections for photo-double-ionization of D_2^-. *Physical Review Letters*, 92:163001, 2004.

[52] W. Vanroose, D. A. Horner, F. Martìın, T. N. Rescigno, and C. W. McCurdy. Double photoionization of aligned molecular hydrogen. *Phys. Rev. A.* 74:052702, 2006.

[53] K. A. Larsen, T. N. Rescigno, Z. L. Streeter, W. Iskandar, S. Heck, A. Gatton, E. G. Champenois, T. Severt, R. A. Strom, B. Jochim, D. Reedy, D. Call, R. Moshammer, R. Dörner, A. L. Landers, J. B. Williams, C. W. McCurdy, R. R. Lucchese, I. Ben-Itzhak, D. S. Slaughter and Th. Weber. Mechanisms and dynamics of the $NH_2^+ + H^+$ and $NH^+ + H^+ + H$ fragmentation channels upon single-photon double ionization of NH_3. *J. Phys. B: Atomic Molecular Optical Physics*, 53:244003, 2020.

[54] K. A. Larsen, T. N. Rescigno, Z. L. Streeter, W. Iskandar, S. Heck, A. Gatton, E. G. Champenois, T. Severt, R. A. Strom, B. Jochim, D. Reedy, D. Call, R. Moshammer, R. Dörner, A. L. Landers, J. B. Williams, C. W. McCurdy, R. R. Lucchese, I. Ben-Itzhak, D. S. Slaughter and Th. Weber. Photoelectron and fragmentation dynamics of the $H^+ + H^+$ dissociative channel in NH_3 following direct single-photon double ionization. *Physics Review Research*, 2:043056, 2020.

[55] M. Stankiewicz, P. A. Hatherly, L. J. Frasinski, K. Codling, and D. N. P. Holland. The double photoionisation of NH_3 using the triple coincidence (PEPIPICO) technique. *J. Phys. B: Atomic Molecular Optical Physics*, 22:21, 1989.

[56] K. Codling, L. J. Frasinski, P. A. Hatherly, M. Stankiewicz, and F. P. Larkins. The double photoionization/fragmentation of CF_4 in the threshold region (35-80eV). *J. Phys. B: Atomic Molecular Optical Physics*, 24:951, 1991.

[57] H. Bruning, R. Dörner, C. L. Cocke, M. H. Prior, B. Krässig, A. S. Kheifets, I. Bray, A. Bräuning-Demian, K. Carnes, S. Dreuil, V. Mergel, P. Richard, J. Ullrich, and H. Schmidt-Böcking. Absolute triple differential cross sections for photo-double ionization of helium - experiment and theory. *J. Phys. B: Atomic Molecular Optical Physics*, 31:5149, 1998.

Appendices

Appendix A

Co-Authored Works

Listed below are a series of co-authored works that were performed in tandem during the author's doctoral tenure. Each report utilized a similar experimental apparatus while exploring similar molecular structures (CF_4, NH_3 and H_2). Although not specific material for the dissertation, the author made contributions to the research and publication of the following reports. These articles stemmed from efforts led by our collaborators at Lawrence Berkeley National Laboratory and Kansas State University in collaboration with the group at Auburn University. These efforts were implemented to support the understanding of the sub-genre and extend the work outside the scope of this thesis. A special note is to be made to the following two reports by Larsen *et al*[53,54] involving the PDI of NH_3. These two experimental studies complemented the author's efforts to measure the final electron momentum distributions and served as confirmation for the scientific findings found within the photoionization portion of this thesis.

Appendix B

Dissociative Electron Attachment Analysis Code for CF_4

Listing B.1: C++ Analysis Code for Presorter and Histograms for Carbon Tetrafluoride

```
1  #include "OS_Version.h"
2  #include "TCanvas.h"
3  #include "TH1D.h"
4  #include "TH2D.h"
5  #include "TApplication.h"
6  #include "TFile.h"
7  #include "TTree.h"
8  #include "TNtupleD.h"
9  #include <math.h>
10 #include "rootstuff.h"
11 #include "Histo.h"
12 #include "TF1.h"
13 #include "TMinuit.h"
14 #include "functions.h"
15 #include "Ueberstruct.h"
```

```
16
17 #define Power(x, y)     (pow((double) (x), (double) (y)))
18
19 int analysis(__int64 eventcounter, double  parameter[],
      TTree * Data, Ueberstruct * Ueber)
20
21 {
22
23     Histo * Hist = Ueber->Hist;
24     Ueber->start_new_root_file = false;
25
26     int plot=0;                                    //plot
         identifier
27     double sumx=0,sumy=0;
28     double r1x=0,r1y=0,r1tof=0;
29     double px[2]={0,0},py[2]={0,0},pt[2]={0,0},KE[2]={0,0},
         KER[2]={0,0};
30     double pr[2]={0,0},ptheta[2]={0,0},pphi[2]={0,0};
31     double pmag[2]={0,0};
32     const double amu = 1.660538e-27;
33     const double SItoAUmom = 1.992851565e-24;
34     const double echarge = 1.60217646e-19;
35     const double pi = acos(-1.0);
36
37     double NTupleData[6];
38     bool WriteNTuple = false;
39
40     if(eventcounter == 0) {
41         Ueber->EntriesInFile = 0;
42         Ueber->eventswritten = 0;
43     }
44
45     if(Ueber->EntriesInFile == 0) {
46
47         Data->SetBranchAddress("r1x",&r1x);
48         Data->SetBranchAddress("r1y",&r1y);
49         Data->SetBranchAddress("r1tof",&r1tof);
50         Data->SetBranchAddress("timesum_x",&sumx);
```

```
51          Data->SetBranchAddress("timesum_y",&sumy);
52      }
53
54      Data->GetEntry(Ueber->EntriesInFile);
55
56      if(Ueber->EntriesInFile < Data->GetEntries()-1) {
57          ++Ueber->EntriesInFile;
58      } else {
59          Ueber->EntriesInFile = 0;
60      }
61      std::string fileName;
62
63  //calculating momenta
64      double tofF[2] = {4300, 5600};
65      bool fragmentF = ((r1tof < tofF[1]) && (r1tof > tofF
            [0]));
66      double tofCF3[2] = {17000,25000};
67      bool fragmentCF3 = ((r1tof < tofCF3[1]) && (r1tof >
            tofCF3[0]));
68      int mass[2] = {19,69};
69      double massRatio = 69./19.;
70      double tofOffset = 0;
71      r1tof = r1tof + tofOffset;
72
73      int index = 2;  //used to label fragments.  value[0] is
            F-, value[1] is CF3-
74
75      if(fragmentF){
76      r1x -= 3;
77      r1y -= 12.5;
78      r1tof -= 70;
79      index = 0;
80  px[index] = (mass[index]*amu*r1x*(0.001)/(r1tof*pow
        (10.0,-9.0)))/SItoAUmom;
81  py[index] = (mass[index]*amu*r1y*(0.001)/(r1tof*pow
        (10.0,-9.0)))/SItoAUmom;
```

```
82  pt[index] = 1376.486220403173 - 0.5001535796096956*r1tof +
       0.000056998175850975*Power(r1tof,2) - 2.4891900890560533
       e-9*Power(r1tof,3);
83  KE[index] = (px[index]*px[index] + py[index]*py[index] + pt
       [index]*pt[index])*27.211/(2*mass[index]*1836.152672);
84  KER[index] = KE[index] *(1 + (1/massRatio));
85  pmag[index] = sqrt(px[index]*px[index]+ py[index]*py[index]
        + pt[index]*pt[index]);
86  pr[index] = pmag[index];
87  pphi[index] = atan2(pt[index], px[index]);
88  ptheta[index] = acos(py[index]/pr[index]);
89      }
90
91      if(fragmentCF3){
92          index = 1;
93  px[index] = (mass[index]*amu*r1x*(0.001)/(r1tof*pow
       (10.0,-9.0)))/SItoAUmom;
94  py[index] = (mass[index]*amu*r1y*(0.001)/(r1tof*pow
       (10.0,-9.0)))/SItoAUmom;
95  pt[index] = 1669.6323230326143 - 0.15983516732773959*r1tof
       + 5.040328389257488e-6*Power(r1tof,2) -
       5.947963164635438e-11*Power(r1tof,3);
96  KE[index] = (px[index]*px[index] + py[index]*py[index] + pt
       [index]*pt[index])*27.211/(2*mass[index]*1836.152672);
97  KER[index] = KE[index] *(1 + massRatio);
98  pmag[index] = sqrt(px[index]*px[index]+ py[index]*py[index]
        + pt[index]*pt[index]);
99  pr[index] = pmag[index];
100 pphi[index] = atan2(pt[index], px[index]);
101 ptheta[index] = acos(py[index]/pr[index]);
102         }
103
104         //Simple Plots
105     int g = 5;
106     char fName[100];
107     fileName = "raw";
108     strcpy(fName, fileName.c_str());
109
```

```
110     Hist->fill1(++g,"TOF",r1tof,1.0,"TOF",1000,0,tofCF3[1],
            "TOF",fName);
111     Hist->fill2(++g,"Pos Y vs X",r1x,r1y,1.,"Pos Y"
            ,100,-45,45.,"Pos X",100,-45.,45.,"Pos Y",fName);
112     Hist->fill2(++g,"Fish X",r1tof,r1x,1.,"Fish X",100,tofF
            [0],tofCF3[1],"TOF",100,-45.,45.,"Pos X",fName);
113     Hist->fill2(++g,"Fish Y",r1tof,r1y,1.,"Fish Y",100,tofF
            [0],tofCF3[1],"TOF",100,-45.,45.,"Pos Y",fName);
114
115         //Zoom Plots
116     if (fragmentF){
117     int g = 105;
118
119     fileName = "F- Zoom";
120     strcpy(fName, fileName.c_str());
121
122     Hist->fill1(++g,"TOF",r1tof,1.0,"TOF",1000,tofF[0],tofF
            [1],"TOF",fName);
123     Hist->fill1(++g,"px",px[index],1.0,"px",1000,-150,150,"
            TOF",fName);
124     Hist->fill1(++g,"py",py[index],1.0,"py",1000,-150,150,"
            TOF",fName);
125     Hist->fill1(++g,"pt",pt[index],1.0,"pt",1000,-150,150,"
            TOF",fName);
126
127     Hist->fill2(++g,"Pos Y vs X",r1x,r1y,1.,"Pos Y"
            ,100,-45,45.,"Pos X",100,-45.,45.,"Pos Y",fName);
128     Hist->fill2(++g,"Fish X",r1tof,r1x,1.,"Fish X",100,tofF
            [0],tofF[1],"TOF",100,-45.,45.,"Pos X",fName);
129     Hist->fill2(++g,"Fish Y",r1tof,r1y,1.,"Fish Y",100,tofF
            [0],tofF[1],"TOF",100,-45.,45.,"Pos Y",fName);
130     Hist->fill2(++g,"Py vs Px",px[index],py[index],1.,"Py
            vs Px",100,-150,150,"Px",100,-150,150,"Py",fName);
131     Hist->fill2(++g,"Pt vs Px",px[index],pt[index],1.,"Py
            vs Px",100,-150,150,"Px",100,-150,150,"Pt",fName);
132     Hist->fill2(++g,"Pt vs Py",py[index],pt[index],1.,"Py
            vs Px",100,-150,150,"Py",100,-150,150,"Pt",fName);
```

```
133         Hist->fill1(++g,"KE",KE[index],1.0,"KE",1000,-1,5,"KE",
                fName);
134         Hist->fill1(++g,"KER",KER[index],1.0,"KER",1000,-1,25,"
                KER",fName);
135
136         }
137
138         if (fragmentCF3){
139
140         int g = 205;
141         fileName = "CF3- Zoom";
142         strcpy(fName, fileName.c_str());
143
144         Hist->fill1(++g,"TOF",r1tof,1.0,"TOF",1000,tofCF3[0],
                tofCF3[1],"TOF",fName);
145         Hist->fill1(++g,"px",px[index],1.0,"px",1000,-150,150,"
                TOF",fName);
146         Hist->fill1(++g,"py",py[index],1.0,"py",1000,-150,150,"
                TOF",fName);
147         Hist->fill1(++g,"pt",pt[index],1.0,"pt",1000,-150,150,"
                TOF",fName);
148
149         Hist->fill2(++g,"Pos Y vs X",r1x,r1y,1.,"Pos Y"
                ,100,-45,45.,"Pos X",100,-45.,45.,"Pos Y",fName);
150         Hist->fill2(++g,"Fish X",r1tof,r1x,1.,"Fish X",100,
                tofCF3[0],tofCF3[1],"TOF",100,-45.,45.,"Pos X",fName
                );
151         Hist->fill2(++g,"Fish Y",r1tof,r1y,1.,"Fish Y",100,
                tofCF3[0],tofCF3[1],"TOF",100,-45.,45.,"Pos Y",fName
                );
152         Hist->fill2(++g,"Py vs Px",px[index],py[index],1.,"Py
                vs Px",100,-150,150,"Px",100,-150,150,"Py",fName);
153         Hist->fill2(++g,"Pt vs Px",px[index],pt[index],1.,"Pt
                vs Px",100,-150,150,"Px",100,-150,150,"Pt",fName);
154         Hist->fill2(++g,"Pt vs Py",py[index],pt[index],1.,"Pt
                vs Py",100,-150,150,"Py",100,-150,150,"Pt",fName);
155         Hist->fill1(++g,"KE",KE[index],1.0,"KE",1000,-1,5,"KE",
                fName);
```

```
156       Hist->fill1(++g,"KER",KER[index],1.0,"KER",1000,-1,25,"
              KER",fName);
157
158       }
159
160       //momenta corrections
161
162   //    px[0] += -13.0;
163   //    py[0] += -41.0;
164   //    pt[0] += 8.0;
165       pt[0] *= 1.32;
166
167       px[1] += -4.8;
168       py[1] += -7.3;
169       pt[1] += 11.0;
170
171       if(fragmentF){
172           index = 0;
173   KE[index] = (px[index]*px[index] + py[index]*py[index] + pt
          [index]*pt[index])*27.211/(2*mass[index]*1836.152672);
174   KER[index] = KE[index] *(1 + (1/massRatio));
175   pmag[index] = sqrt(px[index]*px[index]+ py[index]*py[index]
          + pt[index]*pt[index]);
176   pr[index] = pmag[index];
177   pphi[index] = atan2(pt[index], px[index]);
178   ptheta[index] = acos(py[index]/pr[index]);
179       }
180
181       if(fragmentCF3){
182           index = 1;
183   KE[index] = (px[index]*px[index] + py[index]*py[index] + pt
          [index]*pt[index])*27.211/(2*mass[index]*1836.152672);
184   KER[index] = KE[index] *(1 + massRatio);
185   pmag[index] = sqrt(px[index]*px[index]+ py[index]*py[index]
          + pt[index]*pt[index]);
186   pr[index] = pmag[index];
187   pphi[index] = atan2(pt[index], px[index]);
188   ptheta[index] = acos(py[index]/pr[index]);
```

```
189             }
190
191             //pmag gates
192         bool momLarge[2] = {true,true};//{(pmag[0] > 35.), (
                pmag[1] > 30.)};
193         bool momSmall[2] = {(pmag[0] < 100.), (pmag[1] < 100.)
                };
194         bool momGood[2] = {true,true};//{momSmall[0] &&
                momLarge[0], momSmall[1] && momLarge[1]};
195
196         if(fragmentF && momGood[0]){
197             g = 305;
198
199             fileName = "F- momentum adjusted";
200             strcpy(fName, fileName.c_str());
201
202         Hist->fill1(++g,"TOF",r1tof,1.0,"TOF",1000,tofF[0],tofF
                [1],"TOF",fName);
203         Hist->fill1(++g,"px",px[index],1.0,"px",1000,-150,150,"
                TOF",fName);
204         Hist->fill1(++g,"py",py[index],1.0,"py",1000,-150,150,"
                TOF",fName);
205         Hist->fill1(++g,"pt",pt[index],1.0,"pt",1000,-150,150,"
                TOF",fName);
206
207         Hist->fill2(++g,"Pos Y vs X",r1x,r1y,1.,"Pos Y"
                ,100,-45,45.,"Pos X",100,-45.,45.,"Pos Y",fName);
208         Hist->fill2(++g,"Fish X",r1tof,r1x,1.,"Fish X",100,tofF
                [0],tofF[1],"TOF",100,-45.,45.,"Pos X",fName);
209         Hist->fill2(++g,"Fish Y",r1tof,r1y,1.,"Fish Y",100,tofF
                [0],tofF[1],"TOF",100,-45.,45.,"Pos Y",fName);
210         Hist->fill2(++g,"Py vs Px",px[index],py[index],1.,"Py
                vs Px",100,-150,150,"Px",100,-150,150,"Py",fName);
211         Hist->fill2(++g,"Pt vs Px",px[index],pt[index],1.,"Py
                vs Px",100,-150,150,"Px",100,-150,150,"Pt",fName);
212         Hist->fill2(++g,"Pt vs Py",py[index],pt[index],1.,"Py
                vs Px",100,-150,150,"Py",100,-150,150,"Pt",fName);
```

```
213         Hist->fill1(++g,"KE",KE[index],1.0,"KE",1000,-1,5,"KE",
                fName);
214         Hist->fill1(++g,"KER",KER[index],1.0,"KER",1000,-1,25,"
                KER",fName);
215
216         }
217
218         if(fragmentCF3 && momGood[1]){
219              g = 405;
220              fileName = "CF3- momentum adjusted";
221              strcpy(fName, fileName.c_str());
222
223         Hist->fill1(++g,"TOF",r1tof,1.0,"TOF",1000,tofF[0],tofF
                [1],"TOF",fName);
224         Hist->fill1(++g,"px",px[index],1.0,"px",1000,-150,150,"
                TOF",fName);
225         Hist->fill1(++g,"py",py[index],1.0,"py",1000,-150,150,"
                TOF",fName);
226         Hist->fill1(++g,"pt",pt[index],1.0,"pt",1000,-150,150,"
                TOF",fName);
227
228         Hist->fill2(++g,"Pos Y vs X",r1x,r1y,1.,"Pos Y"
                ,100,-45,45.,"Pos X",100,-45.,45.,"Pos Y",fName);
229         Hist->fill2(++g,"Fish X",r1tof,r1x,1.,"Fish X",100,tofF
                [0],tofF[1],"TOF",100,-45.,45.,"Pos X",fName);
230         Hist->fill2(++g,"Fish Y",r1tof,r1y,1.,"Fish Y",100,tofF
                [0],tofF[1],"TOF",100,-45.,45.,"Pos Y",fName);
231         Hist->fill2(++g,"Py vs Px",px[index],py[index],1.,"Py
                vs Px",100,-150,150,"Px",100,-150,150,"Py",fName);
232         Hist->fill2(++g,"Pt vs Px",px[index],pt[index],1.,"Py
                vs Px",100,-150,150,"Px",100,-150,150,"Pt",fName);
233         Hist->fill2(++g,"Pt vs Py",py[index],pt[index],1.,"Py
                vs Px",100,-150,150,"Py",100,-150,150,"Pt",fName);
234         Hist->fill1(++g,"KE",KE[index],1.0,"KE",1000,-1,5,"KE",
                fName);
235         Hist->fill1(++g,"KER",KER[index],1.0,"KER",1000,-1,25,"
                KER",fName);
236         }
```

```
237
238     //collar gates on momentum
239
240     double halfAngleSmall = 2.5;
241     double halfAngleMedium = 5.0;
242     double halfAngleBig = 10.0;
243
244     bool yCollarSmall[2] = {((asin(py[0]/pmag[0])*180./pi <
            halfAngleSmall) && (asin(py[0]/pmag[0])*180./pi > -
           halfAngleSmall)), ((asin(py[1]/pmag[1])*180./pi <
           halfAngleSmall) && (asin(py[1]/pmag[1])*180./pi > -
           halfAngleSmall))};
245     bool xCollarSmall[2] = {((asin(px[0]/pmag[0])*180./pi <
            halfAngleSmall) && (asin(px[0]/pmag[0])*180./pi > -
           halfAngleSmall)), ((asin(px[1]/pmag[1])*180./pi <
           halfAngleSmall) && (asin(px[1]/pmag[1])*180./pi > -
           halfAngleSmall))};
246     bool tCollarSmall[2] = {((asin(pt[0]/pmag[0])*180./pi <
            halfAngleSmall) && (asin(pt[0]/pmag[0])*180./pi > -
           halfAngleSmall)), ((asin(pt[1]/pmag[1])*180./pi <
           halfAngleSmall) && (asin(pt[1]/pmag[1])*180./pi > -
           halfAngleSmall))};
247
248     bool yCollarMedium[2] = {((asin(py[0]/pmag[0])*180./pi
          < halfAngleMedium) && (asin(py[0]/pmag[0])*180./pi >
            -halfAngleMedium)), ((asin(py[1]/pmag[1])*180./pi <
            halfAngleMedium) && (asin(py[1]/pmag[1])*180./pi >
          -halfAngleMedium))};
249     bool xCollarMedium[2] = {((asin(px[0]/pmag[0])*180./pi
          < halfAngleMedium) && (asin(px[0]/pmag[0])*180./pi >
            -halfAngleMedium)), ((asin(px[1]/pmag[1])*180./pi <
            halfAngleMedium) && (asin(px[1]/pmag[1])*180./pi >
          -halfAngleMedium))};
250     bool tCollarMedium[2] = {((asin(pt[0]/pmag[0])*180./pi
          < halfAngleMedium) && (asin(pt[0]/pmag[0])*180./pi >
            -halfAngleMedium)), ((asin(pt[1]/pmag[1])*180./pi <
            halfAngleMedium) && (asin(pt[1]/pmag[1])*180./pi >
          -halfAngleMedium))};
```

```
251
252       bool yCollarBig[2] = {((asin(py[0]/pmag[0])*180./pi <
              halfAngleBig) && (asin(py[0]/pmag[0])*180./pi > -
              halfAngleBig)), ((asin(py[1]/pmag[1])*180./pi <
              halfAngleBig) && (asin(py[1]/pmag[1])*180./pi > -
              halfAngleBig))} ;
253       bool xCollarBig[2] = {((asin(px[0]/pmag[0])*180./pi <
              halfAngleBig) && (asin(px[0]/pmag[0])*180./pi > -
              halfAngleBig)), ((asin(px[1]/pmag[1])*180./pi <
              halfAngleBig) && (asin(px[1]/pmag[1])*180./pi > -
              halfAngleBig))} ;
254       bool tCollarBig[2] = {((asin(pt[0]/pmag[0])*180./pi <
              halfAngleBig) && (asin(pt[0]/pmag[0])*180./pi > -
              halfAngleBig)), ((asin(pt[1]/pmag[1])*180./pi <
              halfAngleBig) && (asin(pt[1]/pmag[1])*180./pi > -
              halfAngleBig))} ;
255
256       if(fragmentF && xCollarSmall[0] && momGood[0]){
257            g = 505;
258            fileName = "CollarGates/F-/xCollar";
259            strcpy(fName, fileName.c_str());
260            Hist->fill1(++g,"fragment verification",r1tof,1.0,"
                  fragment verification",1000,tofF[0],tofCF3[1],"
                  TOF",fName);
261            Hist->fill2(++g,"Pt vs Py",py[index],pt[index],1.,"
                  Pt vs Py",100,-150,150,"Py",100,-150,150,"Pt",
                  fName);
262            Hist->fill1(++g,"KE",KE[index],1.0,"KE",1000,-1,5,"
                  KE",fName);
263            Hist->fill1(++g,"KER",KER[index],1.0,"KER"
                  ,1000,-1,25,"KER",fName);
264            Hist->fill1(++g,"pmag",pmag[index],1.0,"pmag"
                  ,1000,-5,150,"pmag",fName);
265       }
266
267       if(fragmentF && yCollarMedium[0] && momGood[0]){
268            g = 605;
269            fileName = "CollarGates/F-/yCollar";
```

```
270             strcpy(fName, fileName.c_str());
271
272             Hist->fill1(++g,"fragment verification",r1tof,1.0,"
                    fragment verification",1000,tofF[0],tofCF3[1],"
                    TOF",fName);
273             Hist->fill2(++g,"Pt vs Px",px[index],pt[index],1.,"
                    Pt vs Px",100,-100,100,"Px",100,-100,100,"Pt",
                    fName);
274             Hist->fill1(++g,"KE",KE[index],1.0,"KE",1000,0,3,"
                    KE",fName);
275             Hist->fill1(++g,"KER",KER[index],1.0,"KER"
                    ,1000,0,15,"KER",fName);
276             Hist->fill1(++g,"pmag",pmag[index],1.0,"pmag"
                    ,1000,0,150,"pmag",fName);
277
278         }
279         if(fragmentF && tCollarSmall[0] && momGood[0]){
280             g = 705;
281             fileName = "CollarGates/F-/tCollar";
282             strcpy(fName, fileName.c_str());
283             Hist->fill1(++g,"fragment verification",r1tof,1.0,"
                    fragment verification",1000,tofF[0],tofCF3[1],"
                    TOF",fName);
284             Hist->fill2(++g,"Py vs Px",px[index],py[index],1.,"
                    Py vs Px",100,-150,150,"Px",100,-150,150,"Py",
                    fName);
285             Hist->fill1(++g,"KE",KE[index],1.0,"KE",1000,-1,5,"
                    KE",fName);
286             Hist->fill1(++g,"KER",KER[index],1.0,"KER"
                    ,1000,-1,25,"KER",fName);
287             Hist->fill1(++g,"pmag",pmag[index],1.0,"pmag"
                    ,1000,-5,150,"pmag",fName);
288         }
289         if(fragmentF && (abs(py[0]) < 5)  && momGood[0]){
290             g = 725;
291             fileName = "CollarGates/F-/ySlicedCenter";
292             strcpy(fName, fileName.c_str());
```

```
293             Hist->fill1(++g,"fragment verification",r1tof,1.0,"
                    fragment verification",1000,tofF[0],tofCF3[1],"
                    TOF",fName);
294             Hist->fill2(++g,"Pt vs Px",px[index],pt[index],1.,"
                    Pt vs Px",100,-100,100,"Px",100,-100,100,"Pt",
                    fName);
295             Hist->fill1(++g,"KE",KE[index],1.0,"KE",1000,-1,5,"
                    KE",fName);
296             Hist->fill1(++g,"KER",KER[index],1.0,"KER"
                    ,1000,-1,25,"KER",fName);
297             Hist->fill1(++g,"pmag",pmag[index],1.0,"pmag"
                    ,1000,-5,150,"pmag",fName);
298         }
299         if(fragmentCF3 && xCollarSmall[1] && momGood[1]){
300             g = 805;
301             fileName = "CollarGates/CF3-/xCollar";
302             strcpy(fName, fileName.c_str());
303             Hist->fill1(++g,"fragment verification",r1tof,1.0,"
                    fragment verification",1000,tofF[0],tofCF3[1],"
                    TOF",fName);
304             Hist->fill2(++g,"Pt vs Py",py[index],pt[index],1.,"
                    Pt vs Py",100,-150,150,"Py",100,-150,150,"Pt",
                    fName);
305             Hist->fill1(++g,"KE",KE[index],1.0,"KE",1000,-1,5,"
                    KE",fName);
306             Hist->fill1(++g,"KER",KER[index],1.0,"KER"
                    ,1000,-1,25,"KER",fName);
307             Hist->fill1(++g,"pmag",pmag[index],1.0,"pmag"
                    ,1000,-5,150,"pmag",fName);
308         }
309         if(fragmentCF3 && yCollarSmall[1] && momGood[1]){
310             g = 905;
311             fileName = "CollarGates/CF3-/yCollarSmall";
312             strcpy(fName, fileName.c_str());
313 
314             Hist->fill1(++g,"fragment verification",r1tof,1.0,"
                    fragment verification",1000,tofF[0],tofCF3[1],"
                    TOF",fName);
```

```
315             Hist->fill2(++g,"Pt vs Px",px[index],pt[index],1.,"
                    Pt vs Px",100,-150,150,"Px",100,-150,150,"Pt",
                    fName);
316             Hist->fill1(++g,"KE",KE[index],1.0,"KE",1000,-1,5,"
                    KE",fName);
317             Hist->fill1(++g,"KER",KER[index],1.0,"KER"
                    ,1000,-1,25,"KER",fName);
318             Hist->fill1(++g,"pmag",pmag[index],1.0,"pmag"
                    ,1000,-5,150,"pmag",fName);
319         }
320         if(fragmentCF3 && yCollarMedium[1] && momGood[1]){
321             g = 925;
322             fileName = "CollarGates/CF3-/yCollarMedium";
323             strcpy(fName, fileName.c_str());
324 
325             Hist->fill1(++g,"fragment verification",r1tof,1.0,"
                    fragment verification",1000,tofF[0],tofCF3[1],"
                    TOF",fName);
326             Hist->fill2(++g,"Pt vs Px",px[index],pt[index],1.,"
                    Pt vs Px",100,-150,150,"Px",100,-150,150,"Pt",
                    fName);
327             Hist->fill1(++g,"KE",KE[index],1.0,"KE",1000,-1,5,"
                    KE",fName);
328             Hist->fill1(++g,"KER",KER[index],1.0,"KER"
                    ,1000,-1,25,"KER",fName);
329             Hist->fill1(++g,"pmag",pmag[index],1.0,"pmag"
                    ,1000,-5,150,"pmag",fName);
330         }
331         if(fragmentCF3 && yCollarBig[1] && momGood[1]){
332             g = 945;
333             fileName = "CollarGates/CF3-/yCollarBig";
334             strcpy(fName, fileName.c_str());
335 
336             Hist->fill1(++g,"fragment verification",r1tof,1.0,"
                    fragment verification",1000,tofF[0],tofCF3[1],"
                    TOF",fName);
```

```
337             Hist->fill2(++g,"Pt vs Px",px[index],pt[index],1.,"
                    Pt vs Px",100,-150,150,"Px",100,-150,150,"Pt",
                    fName);
338             Hist->fill1(++g,"KE",KE[index],1.0,"KE",1000,-1,5,"
                    KE",fName);
339             Hist->fill1(++g,"KER",KER[index],1.0,"KER"
                    ,1000,-1,25,"KER",fName);
340             Hist->fill1(++g,"pmag",pmag[index],1.0,"pmag"
                    ,1000,-5,150,"pmag",fName);
341         }
342         if(fragmentCF3 && tCollarSmall[1] && momGood[1]){
343             g = 1005;
344             fileName = "CollarGates/CF3-/tCollar";
345             strcpy(fName, fileName.c_str());
346             Hist->fill1(++g,"fragment verification",r1tof,1.0,"
                    fragment verification",1000,tofF[0],tofCF3[1],"
                    TOF",fName);
347             Hist->fill2(++g,"Py vs Px",px[index],py[index],1.,"
                    Py vs Px",100,-150,150,"Px",100,-150,150,"Py",
                    fName);
348             Hist->fill1(++g,"KE",KE[index],1.0,"KE",1000,-1,5,"
                    KE",fName);
349             Hist->fill1(++g,"KER",KER[index],1.0,"KER"
                    ,1000,-1,25,"KER",fName);
350             Hist->fill1(++g,"pmag",pmag[index],1.0,"pmag"
                    ,1000,-5,150,"pmag",fName);
351         }
352             //turn on Pmag gate
353         momGood[0] = (momSmall[0] && momLarge[0]);
354         momGood[1] = (momSmall[1] && momLarge[1]);
355
356         if(fragmentF && momGood[0]){
357             g = 1105;
358             fileName = "F- momentum adjusted/P Mag Gate";
359             strcpy(fName, fileName.c_str());
360
```

```
361         Hist->fill1(++g,"fragment verification",r1tof,1.0,"
                fragment verification",1000,tofF[0],tofCF3[1],"TOF",
                fName);
362         Hist->fill2(++g,"Py vs Px",px[index],py[index],1.,"Py
                vs Px",100,-100,100,"Px",100,-100,100,"Py",fName);
363         Hist->fill2(++g,"Pt vs Px",px[index],pt[index],1.,"Py
                vs Px",100,-100,100,"Px",100,-100,100,"Pt",fName);
364         Hist->fill2(++g,"Pt vs Py",py[index],pt[index],1.,"Py
                vs Px",100,-100,100,"Py",100,-100,100,"Pt",fName);
365         Hist->fill1(++g,"KE",KE[index],1.0,"KE",1000,-1,5,"KE",
                fName);
366         Hist->fill1(++g,"KER",KER[index],1.0,"KER",1000,-1,25,"
                KER",fName);
367         Hist->fill1(++g,"pmag",pmag[index],1.0,"pmag"
                ,1000,-5,150,"pmag",fName);
368
369         }
370
371         if(fragmentCF3 && momGood[1]){
372             g = 1205;
373             fileName = "CF3- momentum adjusted/P Mag Gate";
374             strcpy(fName, fileName.c_str());
375
376         Hist->fill1(++g,"fragment verification",r1tof,1.0,"
                fragment verification",1000,tofF[0],tofCF3[1],"TOF",
                fName);
377         Hist->fill2(++g,"Py vs Px",px[index],py[index],1.,"Py
                vs Px",100,-100,100,"Px",100,-100,100,"Py",fName);
378         Hist->fill2(++g,"Pt vs Px",px[index],pt[index],1.,"Pt
                vs Px",100,-100,100,"Px",100,-100,100,"Pt",fName);
379         Hist->fill2(++g,"Pt vs Py",py[index],pt[index],1.,"Pt
                vs Py",100,-100,100,"Py",100,-100,100,"Pt",fName);
380         Hist->fill1(++g,"KE",KE[index],1.0,"KE",1000,-1,5,"KE",
                fName);
381         Hist->fill1(++g,"KER",KER[index],1.0,"KER",1000,-1,25,"
                KER",fName);
382         Hist->fill1(++g,"pmag",pmag[index],1.0,"pmag"
                ,1000,-5,150,"pmag",fName);
```

```
383         }
384
385         //collar gates on momentum
386
387         if(fragmentF && xCollarSmall[0] && momGood[0]){
388             g = 1305;
389             fileName = "CollarGates/F-/xCollar/P Mag Gate";
390             strcpy(fName, fileName.c_str());
391             Hist->fill1(++g,"fragment verification",r1tof,1.0,"
                    fragment verification",1000,tofF[0],tofCF3[1],"
                    TOF",fName);
392             Hist->fill2(++g,"Pt vs Py",py[index],pt[index],1.,"
                    Pt vs Py",100,-150,150,"Py",100,-150,150,"Pt",
                    fName);
393             Hist->fill1(++g,"KE",KE[index],1.0,"KE",1000,-1,5,"
                    KE",fName);
394             Hist->fill1(++g,"KER",KER[index],1.0,"KER"
                    ,1000,-1,25,"KER",fName);
395             Hist->fill1(++g,"pmag",pmag[index],1.0,"pmag"
                    ,1000,-5,150,"pmag",fName);
396         }
397
398         if(fragmentF && yCollarSmall[0] && momGood[0]){
399             g = 1405;
400             fileName = "CollarGates/F-/yCollar/P Mag Gate";
401             strcpy(fName, fileName.c_str());
402             Hist->fill1(++g,"fragment verification",r1tof,1.0,"
                    fragment verification",1000,tofF[0],tofCF3[1],"
                    TOF",fName);
403             Hist->fill2(++g,"Pt vs Px",px[index],pt[index],1.,"
                    Pt vs Px",100,-150,150,"Px",100,-150,150,"Pt",
                    fName);
404             Hist->fill1(++g,"KE",KE[index],1.0,"KE",1000,-1,5,"
                    KE",fName);
405             Hist->fill1(++g,"KER",KER[index],1.0,"KER"
                    ,1000,-1,25,"KER",fName);
406             Hist->fill1(++g,"pmag",pmag[index],1.0,"pmag"
                    ,1000,-5,150,"pmag",fName);
```

```
407
408         }
409         if(fragmentF && tCollarSmall[0] && momGood[0]){
410             g = 1505;
411             fileName = "CollarGates/F-/tCollar/P Mag Gate";
412             strcpy(fName, fileName.c_str());
413             Hist->fill1(++g,"fragment verification",r1tof,1.0,"
                    fragment verification",1000,tofF[0],tofCF3[1],"
                    TOF",fName);
414             Hist->fill2(++g,"Py vs Px",px[index],py[index],1.,"
                    Py vs Px",100,-150,150,"Px",100,-150,150,"Py",
                    fName);
415             Hist->fill1(++g,"KE",KE[index],1.0,"KE",1000,-1,5,"
                    KE",fName);
416             Hist->fill1(++g,"KER",KER[index],1.0,"KER"
                    ,1000,-1,25,"KER",fName);
417             Hist->fill1(++g,"pmag",pmag[index],1.0,"pmag"
                    ,1000,-5,150,"pmag",fName);
418         }
419         if(fragmentCF3 && xCollarSmall[1] && momGood[1]){
420             g = 1605;
421             fileName = "CollarGates/CF3-/xCollar/P Mag Gate";
422             strcpy(fName, fileName.c_str());
423             Hist->fill1(++g,"fragment verification",r1tof,1.0,"
                    fragment verification",1000,tofF[0],tofCF3[1],"
                    TOF",fName);
424             Hist->fill2(++g,"Pt vs Py",py[index],pt[index],1.,"
                    Pt vs Py",100,-150,150,"Py",100,-150,150,"Pt",
                    fName);
425             Hist->fill1(++g,"KE",KE[index],1.0,"KE",1000,-1,5,"
                    KE",fName);
426             Hist->fill1(++g,"KER",KER[index],1.0,"KER"
                    ,1000,-1,25,"KER",fName);
427             Hist->fill1(++g,"pmag",pmag[index],1.0,"pmag"
                    ,1000,-5,150,"pmag",fName);
428         }
429         if(fragmentCF3 && yCollarSmall[1] && momGood[1]){
430             g = 1705;
```

```
431             fileName = "CollarGates/CF3-/yCollar/P Mag Gate";
432             strcpy(fName, fileName.c_str());
433             Hist->fill1(++g,"fragment verification",r1tof,1.0,"
                    fragment verification",1000,tofF[0],tofCF3[1],"
                    TOF",fName);
434             Hist->fill2(++g,"Pt vs Px",px[index],pt[index],1.,"
                    Pt vs Px",100,-150,150,"Px",100,-150,150,"Pt",
                    fName);
435             Hist->fill1(++g,"KE",KE[index],1.0,"KE",1000,-1,5,"
                    KE",fName);
436             Hist->fill1(++g,"KER",KER[index],1.0,"KER"
                    ,1000,-1,25,"KER",fName);
437             Hist->fill1(++g,"pmag",pmag[index],1.0,"pmag"
                    ,1000,-5,150,"pmag",fName);
438         }
439         if(fragmentCF3 && tCollarSmall[1] && momGood[1]){
440             g = 1805;
441             fileName = "CollarGates/CF3-/tCollar/P Mag Gate";
442             strcpy(fName, fileName.c_str());
443             Hist->fill1(++g,"fragment verification",r1tof,1.0,"
                    fragment verification",1000,tofF[0],tofCF3[1],"
                    TOF",fName);
444             Hist->fill2(++g,"Py vs Px",px[index],py[index],1.,"
                    Py vs Px",100,-150,150,"Px",100,-150,150,"Py",
                    fName);
445             Hist->fill1(++g,"KE",KE[index],1.0,"KE",1000,-1,5,"
                    KE",fName);
446             Hist->fill1(++g,"KER",KER[index],1.0,"KER"
                    ,1000,-1,25,"KER",fName);
447             Hist->fill1(++g,"pmag",pmag[index],1.0,"pmag"
                    ,1000,-5,150,"pmag",fName);
448         }
449             double coneValue = 0.95;
450
451         bool xConeUp     = px[1]/pmag[1] > coneValue;
452         bool xConeDown = px[1]/pmag[1] < -coneValue;
453         bool yConeUp     = py[1]/pmag[1] > coneValue;
454         bool yConeDown = py[1]/pmag[1] < -coneValue;
```

```
455     bool tConeUp      = pt[1]/pmag[1] > coneValue;
456     bool tConeDown = pt[1]/pmag[1] < -coneValue;
457     bool yConeSmall[2] = {(((py[0]/pmag[0]) < -coneValue)
           || ((py[0]/pmag[0]) > coneValue)), (((py[1]/pmag[1])
           < -coneValue) || ((py[1]/pmag[1]) > coneValue))} ;
458     bool xConeSmall[2] = {(((px[0]/pmag[0]) < -coneValue)
           || ((px[0]/pmag[0]) > coneValue)), (((px[1]/pmag[1])
           < -coneValue) || ((px[1]/pmag[1]) > coneValue))} ;
459     bool tConeSmall[2] = {(((pt[0]/pmag[0]) < -coneValue)
           || ((pt[0]/pmag[0]) > coneValue)), (((pt[1]/pmag[1])
           < -coneValue) || ((pt[1]/pmag[1]) > coneValue))} ;
460
461     if(fragmentCF3 && (yConeDown || tConeUp)){
462         g = 1905;
463         fileName = "ConeGates/CF3-/yDown + tUp";
464         strcpy(fName, fileName.c_str());
465         Hist->fill1(++g,"TOF",r1tof,1.0,"TOF"
               ,1000,11000,16000,"TOF",fName);
466         Hist->fill1(++g,"KE",KE[index],1.0,"KE",1000,-1,5,"
              KE",fName);
467         Hist->fill1(++g,"KER",KER[index],1.0,"KER"
               ,1000,-1,25,"KER",fName);
468         Hist->fill1(++g,"px",px[index],1.0,"px"
               ,1000,-100,100,"px",fName);
469         Hist->fill2(++g,"Py vs Px",px[index],py[index],1.,"
              Py vs Px",100,-150,150,"Px",100,-150,150,"Py",
              fName);
470         Hist->fill2(++g,"Pt vs Px",px[index],pt[index],1.,"
              Pt vs Px",100,-150,150,"Px",100,-150,150,"Pt",
              fName);
471         Hist->fill2(++g,"Pt vs Py",py[index],pt[index],1.,"
              Pt vs Py",100,-150,150,"Py",100,-150,150,"Pt",
              fName);
472     }
473     if(fragmentCF3 && yConeDown){
474         g = 1950;
475         fileName = "ConeGates/CF3-/yConeDown";
476         strcpy(fName, fileName.c_str());
```

```
477             Hist->fill1(++g,"TOF",r1tof,1.0,"TOF"
                    ,1000,11000,16000,"TOF",fName);
478             Hist->fill1(++g,"KE",(px[index]*px[index] + py[
                    index]*py[index] + pt[index]*pt[index])
                    *27.211/(2*mass[index]*1836.152672),1.0,"KE"
                    ,1000,-1,5,"KE",fName);
479             Hist->fill1(++g,"KER",KER[index],1.0,"KER"
                    ,1000,-1,25,"KER",fName);
480             Hist->fill1(++g,"px",px[index],1.0,"px"
                    ,1000,-100,100,"px",fName);
481             Hist->fill2(++g,"Py vs Px",px[index],py[index],1.,"
                    Py vs Px",100,-150,150,"Px",100,-150,150,"Py",
                    fName);
482             Hist->fill2(++g,"Pt vs Px",px[index],pt[index],1.,"
                    Pt vs Px",100,-150,150,"Px",100,-150,150,"Pt",
                    fName);
483             Hist->fill2(++g,"Pt vs Py",py[index],pt[index],1.,"
                    Pt vs Py",100,-150,150,"Py",100,-150,150,"Pt",
                    fName);
484         }
485             if(fragmentCF3 && yConeUp){
486             g = 2005;
487             fileName = "ConeGates/CF3-/yConeUp";
488             strcpy(fName, fileName.c_str());
489             Hist->fill1(++g,"TOF",r1tof,1.0,"TOF"
                    ,1000,11000,16000,"TOF",fName);
490             Hist->fill1(++g,"KE",(px[index]*px[index] + py[
                    index]*py[index] + pt[index]*pt[index])
                    *27.211/(2*mass[index]*1836.152672),1.0,"KE"
                    ,1000,-1,5,"KE",fName);
491             Hist->fill1(++g,"KER",KER[index],1.0,"KER"
                    ,1000,-1,25,"KER",fName);
492             Hist->fill1(++g,"px",px[index],1.0,"px"
                    ,1000,-100,100,"px",fName);
493             Hist->fill2(++g,"Py vs Px",px[index],py[index],1.,"
                    Py vs Px",100,-150,150,"Px",100,-150,150,"Py",
                    fName);
```

```
494             Hist->fill2(++g,"Pt vs Px",px[index],pt[index],1.,"
                    Pt vs Px",100,-150,150,"Px",100,-150,150,"Pt",
                    fName);
495             Hist->fill2(++g,"Pt vs Py",py[index],pt[index],1.,"
                    Pt vs Py",100,-150,150,"Py",100,-150,150,"Pt",
                    fName);
496         }
497         if(fragmentCF3 && xConeDown){
498             g = 2055;
499             fileName = "ConeGates/CF3-/xConeDown";
500             strcpy(fName, fileName.c_str());
501             Hist->fill1(++g,"TOF",r1tof,1.0,"TOF"
                    ,1000,11000,16000,"TOF",fName);
502             Hist->fill1(++g,"KE",(px[index]*px[index] + py[
                    index]*py[index] + pt[index]*pt[index])
                    *27.211/(2*mass[index]*1836.152672),1.0,"KE"
                    ,1000,-1,5,"KE",fName);
503
504             Hist->fill1(++g,"px",px[index],1.0,"px"
                    ,1000,-100,100,"px",fName);
505             Hist->fill2(++g,"Py vs Px",px[index],py[index],1.,"
                    Py vs Px",100,-150,150,"Px",100,-150,150,"Py",
                    fName);
506             Hist->fill2(++g,"Pt vs Px",px[index],pt[index],1.,"
                    Pt vs Px",100,-150,150,"Px",100,-150,150,"Pt",
                    fName);
507             Hist->fill2(++g,"Pt vs Py",py[index],pt[index],1.,"
                    Pt vs Py",100,-150,150,"Py",100,-150,150,"Pt",
                    fName);
508         }
509         if(fragmentCF3 && xConeUp){
510             g = 2105;
511             fileName = "ConeGates/CF3-/xConeUp";
512             strcpy(fName, fileName.c_str());
513             Hist->fill1(++g,"TOF",r1tof,1.0,"TOF"
                    ,1000,11000,16000,"TOF",fName);
```

```
514             Hist->fill1(++g,"KE",(px[index]*px[index] + py[
                    index]*py[index] + pt[index]*pt[index])
                    *27.211/(2*mass[index]*1836.152672),1.0,"KE"
                    ,1000,-1,5,"KE",fName);
515             Hist->fill1(++g,"KER",KER[index],1.0,"KER"
                    ,1000,-1,25,"KER",fName);
516             Hist->fill1(++g,"px",px[index],1.0,"px"
                    ,1000,-100,100,"px",fName);
517             Hist->fill2(++g,"Py vs Px",px[index],py[index],1.,"
                    Py vs Px",100,-150,150,"Px",100,-150,150,"Py",
                    fName);
518             Hist->fill2(++g,"Pt vs Px",px[index],pt[index],1.,"
                    Pt vs Px",100,-150,150,"Px",100,-150,150,"Pt",
                    fName);
519             Hist->fill2(++g,"Pt vs Py",py[index],pt[index],1.,"
                    Pt vs Py",100,-150,150,"Py",100,-150,150,"Pt",
                    fName);
520         }
521         if(fragmentCF3 && tConeDown){
522             g = 2155;
523             fileName = "ConeGates/CF3-/tConeDown";
524             strcpy(fName, fileName.c_str());
525             Hist->fill1(++g,"TOF",r1tof,1.0,"TOF"
                    ,1000,11000,16000,"TOF",fName);
526             Hist->fill1(++g,"KE",(px[index]*px[index] + py[
                    index]*py[index] + pt[index]*pt[index])
                    *27.211/(2*mass[index]*1836.152672),1.0,"KE"
                    ,1000,-1,5,"KE",fName);
527             Hist->fill1(++g,"KER",KER[index],1.0,"KER"
                    ,1000,-1,25,"KER",fName);
528             Hist->fill1(++g,"px",px[index],1.0,"px"
                    ,1000,-100,100,"px",fName);
529             Hist->fill2(++g,"Py vs Px",px[index],py[index],1.,"
                    Py vs Px",100,-150,150,"Px",100,-150,150,"Py",
                    fName);
530             Hist->fill2(++g,"Pt vs Px",px[index],pt[index],1.,"
                    Pt vs Px",100,-150,150,"Px",100,-150,150,"Pt",
                    fName);
```

```
531             Hist->fill2(++g,"Pt vs Py",py[index],pt[index],1.,"
                    Pt vs Py",100,-150,150,"Py",100,-150,150,"Pt",
                    fName);
532         }
533         if(fragmentCF3 && tConeUp){
534             g = 2205;
535             fileName = "ConeGates/CF3-/tConeUp";
536             strcpy(fName, fileName.c_str());
537             Hist->fill1(++g,"TOF",r1tof,1.0,"TOF"
                    ,1000,11000,16000,"TOF",fName);
538             Hist->fill1(++g,"KE",(px[index]*px[index] + py[
                    index]*py[index] + pt[index]*pt[index])
                    *27.211/(2*mass[index]*1836.152672),1.0,"KE"
                    ,1000,-1,5,"KE",fName);
539             Hist->fill1(++g,"KER",KER[index],1.0,"KER"
                    ,1000,-1,25,"KER",fName);
540             Hist->fill1(++g,"px",px[index],1.0,"px"
                    ,1000,-100,100,"px",fName);
541             Hist->fill2(++g,"Py vs Px",px[index],py[index],1.,"
                    Py vs Px",100,-150,150,"Px",100,-150,150,"Py",
                    fName);
542             Hist->fill2(++g,"Pt vs Px",px[index],pt[index],1.,"
                    Pt vs Px",100,-150,150,"Px",100,-150,150,"Pt",
                    fName);
543             Hist->fill2(++g,"Pt vs Py",py[index],pt[index],1.,"
                    Pt vs Py",100,-150,150,"Py",100,-150,150,"Pt",
                    fName);
544         }
545
546                     if(fragmentCF3 && ((180./pi)*atan2(sqrt(py[
                            index]*py[index] + pt[index]*pt[index])
                            ,(-px[index])) < 35.)// && (pmag[index]
                            > 45.) && (pmag[index] < 100.)
547             ){
548             g = 2225;
549             fileName = "LobeGates/ForwardLobe";
550             strcpy(fName, fileName.c_str());
551
```

```
552             Hist->fill1(++g,"fragment verification",r1tof,1.0,"
                    fragment verification",1000,tofF[0],tofCF3[1],"
                    TOF",fName);
553             Hist->fill2(++g,"Pt vs Px",px[index],pt[index],1.,"
                    Pt vs Px",100,-150,150,"Px",100,-150,150,"Pt",
                    fName);
554             Hist->fill1(++g,"KE",KE[index],1.0,"KE",1000,-1,5,"
                    KE",fName);
555             Hist->fill1(++g,"KER",KER[index],1.0,"KER"
                    ,1000,-1,25,"KER",fName);
556             Hist->fill1(++g,"pmag",pmag[index],1.0,"pmag"
                    ,1000,-5,150,"pmag",fName);
557             Hist->fill1(++g,"phi angle",(180/pi)*pphi[index
                    ],1.0,"angle",1000,-180,180,"angle",fName);
558             Hist->fill1(++g,"theta angle",(180/pi)*ptheta[index
                    ],1.0,"angle",1000,-180,180,"angle",fName);
559
560             }
561
562
563                 if(fragmentCF3 && ((180./pi)*atan(sqrt(py[index
                        ]*py[index] + pt[index]*pt[index])/(-px[
                        index])) > 30.)// && (pmag[index] > 45.) &&
                        (pmag[index] < 100.)
564                 && ((180./pi)*atan(sqrt(py[index]*py[index] +
                        pt[index]*pt[index])/(-px[index])) < 90.)
565             ){
566             g = 2235;
567             fileName = "LobeGates/Ring 1";
568             strcpy(fName, fileName.c_str());
569
570             Hist->fill1(++g,"fragment verification",r1tof,1.0,"
                    fragment verification",1000,tofF[0],tofCF3[1],"
                    TOF",fName);
571             Hist->fill2(++g,"Pt vs Px",px[index],pt[index],1.,"
                    Pt vs Px",100,-150,150,"Px",100,-150,150,"Pt",
                    fName);
```

```
572             Hist->fill1(++g,"KE",KE[index],1.0,"KE",1000,-1,5,"
                    KE",fName);
573             Hist->fill1(++g,"KER",KER[index],1.0,"KER"
                    ,1000,-1,25,"KER",fName);
574             Hist->fill1(++g,"pmag",pmag[index],1.0,"pmag"
                    ,1000,-5,150,"pmag",fName);
575             Hist->fill1(++g,"phi angle",(180/pi)*pphi[index
                    ],1.0,"angle",1000,-180,180,"angle",fName);
576             Hist->fill1(++g,"theta angle",(180/pi)*ptheta[index
                    ],1.0,"angle",1000,-180,180,"angle",fName);
577
578             }
579
580                 if(fragmentCF3 && ((180./pi)*atan2(sqrt(py[
                        index]*py[index] + pt[index]*pt[index]),(-px
                        [index])) > 90.)// && (pmag[index] > 45.) &&
                         (pmag[index] < 100.)
581                 && ((180./pi)*atan2(sqrt(py[index]*py[index] +
                        pt[index]*pt[index]),(-px[index])) < 150.)
582             ){
583             g = 2245;
584             fileName = "LobeGates/Ring 2";
585             strcpy(fName, fileName.c_str());
586
587             Hist->fill1(++g,"fragment verification",r1tof,1.0,"
                    fragment verification",1000,tofF[0],tofCF3[1],"
                    TOF",fName);
588             Hist->fill2(++g,"Pt vs Px",px[index],pt[index],1.,"
                    Pt vs Px",100,-150,150,"Px",100,-150,150,"Pt",
                    fName);
589             Hist->fill1(++g,"KE",KE[index],1.0,"KE",1000,-1,5,"
                    KE",fName);
590             Hist->fill1(++g,"KER",KER[index],1.0,"KER"
                    ,1000,-1,25,"KER",fName);
591             Hist->fill1(++g,"pmag",pmag[index],1.0,"pmag"
                    ,1000,-5,150,"pmag",fName);
592             Hist->fill1(++g,"phi angle",(180/pi)*pphi[index
                    ],1.0,"angle",1000,-180,180,"angle",fName);
```

```
593             Hist->fill1(++g,"theta angle",(180/pi)*ptheta[index
                    ],1.0,"angle",1000,-180,180,"angle",fName);
594
595             }
596
597         if(WriteNTuple && (fragmentCF3 || fragmentF)) {
598             NTupleData[0] = double(r1x);
599             NTupleData[1] = double(r1y);
600             NTupleData[2] = double(r1tof);
601             NTupleData[3] = double(sumx);
602             NTupleData[4] = double(sumy);
603
604             Hist->NTupleD(0,"Data","H20BESSY08","r1x:r1y:r1tof:
                    sumx:sumy", 32000, NTupleData);
605             Ueber->eventswritten++;
606         }
607
608         if(parameter[57]>0.5) {
609             unsigned __int64 max_events = (unsigned __int64)(
                    parameter[56]+0.1);
610             if(Ueber->eventswritten > (__int64)max_events &&
                    max_events > 0) {
611                 Ueber->start_new_root_file = true;
612                 Ueber->eventswritten = 0;
613                 Hist->Reset();
614             }
615         }
616
617         return 0;
618 }
```

Appendix C

Double Photoionization Analysis Code for NH_3

Listing C.1: C++ Analysis Code for Presorter and Histograms for Ammonia following PDI

```
1  #include "OS_Version.h"
2  #include "CH_Histograms.h"
3  #include <algorithm>
4
5  namespace CH
6  {
7      void histograms_class::plot_polyatomic(reaction_struct
           *cur_reaction, polyatomic_class * big_mol,
           electron_class ** e, int ehit, double *scan_val)
8      {
9          if(!big_mol->valid)
10             return;
11
12         histo_handler *Hist = this->Hist_ions;
```

```
13          range_class *rg = cur_reaction->rng;
14          int rgti = RA_ION;
15          int rgtp = RA_POLYATOMIC;
16          int rgte = RA_ELECTRON;
17
18          // histogram index stuff
19          int hmax = HISTS_PER_CHANNEL; // overall number of
              ColAHelL histograms per reaction/channel
20          int hoff = hmax*16*(int)cur_reaction->reac_num;
21
22          // limit to 16 hits..
23          if(ehit>16)
24              ehit=16;
25
26          char reaction_dir[360];
27          char x_axis_title[80];
28          char y_axis_title[80];
29
30          char rootdir[360];
31          char ndir[360];
32          char alldir[360];
33          char tdir[360];
34
35          if(this->use_master_folder) {
36              strcpy(reaction_dir,this->CH_master_folder);
37              strcat(reaction_dir,cur_reaction->name);
38          } else
39              strcpy(reaction_dir,cur_reaction->name);

40
41          strcpy(rootdir,reaction_dir);
42
43          double rtof_sum1 = 0.;
44          double rtof_sum2 = 0.;
45
46          for(int i=0; i<big_mol->number_of_ions;i++) {
47              strcpy(ndir,rootdir);
```

```
48          sprintf(tdir,"/ion%i_m%i_q%i", i+1, int(big_mol
               ->ion[i]->raw.m+0.001), int(big_mol->ion[i
               ]->raw.q + 0.001));
49          strcat(ndir,tdir);
50          strcpy(tdir,ndir);
51
52          Hist->fill(hoff+hmax*i+0,"ion_energy",big_mol->
               ion[i]->energy(),1.,"ion energy",rg->
               get_bins(rgti+i,ENERGY),rg->get_from(rgti+i,
               ENERGY),rg->get_to(rgti+i,ENERGY),"ion
               energy [eV]",strcat(ndir,"/energy"));
53          Hist->fill(hoff+hmax*i+1,"phi_vs_ion_energy",
               big_mol->ion[i]->raw.phi,big_mol->ion[i]->
               energy(),1.,"ion energy vs. phi on detector"
               ,rg->get_bins(rgti+i,PHILAB),rg->get_from(
               rgti+i,PHILAB),rg->get_to(rgti+i,PHILAB),"
               phi [deg]",rg->get_bins(rgti+i,ENERGY),rg->
               get_from(rgti+i,ENERGY),rg->get_to(rgti+i,
               ENERGY),"ion energy [eV]",ndir);
54          Hist->fill(hoff+hmax*i+2,"ctheta_vs_ion_energy"
               ,big_mol->ion[i]->mom.Cos_Theta(),big_mol->
               ion[i]->energy(),1.,"ion energy vs. cos(
               theta_z)",rg->get_bins(rgti+i,CTELAB),rg->
               get_from(rgti+i,CTELAB),rg->get_to(rgti+i,
               CTELAB),"ctheta",rg->get_bins(rgti+i,ENERGY)
               ,rg->get_from(rgti+i,ENERGY),rg->get_to(rgti
               +i,ENERGY),"ion energy [eV]",ndir);
55
56          strcpy(ndir,tdir);
57          Hist->fill(hoff+hmax*i+3,"px_vs_py",big_mol->
               ion[i]->mom.x,big_mol->ion[i]->mom.y,1.,"p_x
                vs. p_y",rg->get_bins(rgti+i,PX),rg->
               get_from(rgti+i,PX),rg->get_to(rgti+i,PX),"
               p_x [a.u.]",rg->get_bins(rgti+i,PY),rg->
               get_from(rgti+i,PY),rg->get_to(rgti+i,PY),"
               p_y [a.u.]",strcat(ndir,"/momenta"));
```

```
58          Hist->fill(hoff+hmax*i+4,"px_vs_pz",big_mol->
                ion[i]->mom.x,big_mol->ion[i]->mom.z,1.,"p_x
                 vs. p_z",rg->get_bins(rgti+i,PX),rg->
                get_from(rgti+i,PX),rg->get_to(rgti+i,PX),"
                p_x [a.u.]",rg->get_bins(rgti+i,PZ),rg->
                get_from(rgti+i,PZ),rg->get_to(rgti+i,PZ),"
                p_z [a.u.]",ndir);
59          Hist->fill(hoff+hmax*i+5,"py_vs_pz",big_mol->
                ion[i]->mom.y,big_mol->ion[i]->mom.z,1.,"p_y
                 vs. p_z",rg->get_bins(rgti+i,PY),rg->
                get_from(rgti+i,PY),rg->get_to(rgti+i,PY),"
                p_y [a.u.]",rg->get_bins(rgti+i,PZ),rg->
                get_from(rgti+i,PZ),rg->get_to(rgti+i,PZ),"
                p_z [a.u.]",ndir);
60          Hist->fill(hoff+hmax*i+6,"p_mag",big_mol->ion[i
                ]->mom.Mag(),1.,"|p|",rg->get_bins(rgti+i,P)
                ,rg->get_from(rgti+i,P),rg->get_to(rgti+i,P)
                ,"|p| [a.u.]",ndir);
61
62          strcpy(ndir,tdir);
63          Hist->fill(hoff+hmax*i+7,"phi",big_mol->ion[i
                ]->mom.Phi_deg(),1.,"phi in the labframe",rg
                ->get_bins(rgti+i,PHILAB),rg->get_from(rgti+
                i,PHILAB),rg->get_to(rgti+i,PHILAB),"phi [
                deg]",strcat(ndir,"/angles_labframe"));
64          Hist->fill(hoff+hmax*i+8,"ctheta",big_mol->ion[
                i]->mom.Cos_Theta(),1.,"cos(theta) in the
                labframe",rg->get_bins(rgti+i,CTELAB),rg->
                get_from(rgti+i,CTELAB),rg->get_to(rgti+i,
                CTELAB),"cos(theta)",ndir);
65
66          strcpy(ndir,tdir);
67          Hist->fill(hoff+hmax*i+9,"position",big_mol->
                ion[i]->raw.data.x,big_mol->ion[i]->raw.data
                .y,1.,"position",400,-1.*rdet_size,rdet_size
                ,"x [mm]",400,-1.*rdet_size,rdet_size,"y [mm
                ]",strcat(ndir,"/raw"));
```

```
68          Hist->fill(hoff+hmax*i+10,"tof",big_mol->ion[i
                ]->raw.data.tof,1.,"time-of-flight",rg->
                get_bins(rgti+i,TOF),rg->get_from(rgti+i,TOF
                ),rg->get_to(rgti+i,TOF),"tof [ns]",ndir);
69          Hist->fill(hoff+hmax*i+11,"wiggle",big_mol->ion
                [i]->raw.data.tof,(sqrt(big_mol->ion[i]->raw
                .data.x*big_mol->ion[i]->raw.data.x+big_mol
                ->ion[i]->raw.data.y*big_mol->ion[i]->raw.
                data.y)),1.,"wiggles",rg->get_bins(rgti+i,
                TOF),rg->get_from(rgti+i,TOF),rg->get_to(
                rgti+i,TOF),"tof [ns]",200,-1.,rdet_size,"r
                [mm]",ndir);
70          Hist->fill(hoff+hmax*i+12,"fish_x",big_mol->ion
                [i]->raw.data.tof,big_mol->ion[i]->raw.data.
                x,1.,"x-fish",rg->get_bins(rgti+i,TOF),rg->
                get_from(rgti+i,TOF),rg->get_to(rgti+i,TOF),
                "tof [ns]",200,-1.*rdet_size,rdet_size,"x [
                mm]",ndir);
71          Hist->fill(hoff+hmax*i+13,"fish_y",big_mol->ion
                [i]->raw.data.tof,big_mol->ion[i]->raw.data.
                y,1.,"y-fish",rg->get_bins(rgti+i,TOF),rg->
                get_from(rgti+i,TOF),rg->get_to(rgti+i,TOF),
                "tof [ns]",200,-1.*rdet_size,rdet_size,"y [
                mm]",ndir);
72          if ( fabs(big_mol->ion[i]->raw.data.y)<10. )
73            Hist->fill(hoff+hmax*i+14,"fish_filet_x",
                  big_mol->ion[i]->raw.data.tof,big_mol->
                  ion[i]->raw.data.x,1.,"x-fish filet",rg
                  ->get_bins(rgti+i,TOF),rg->get_from(rgti
                  +i,TOF),rg->get_to(rgti+i,TOF),"tof [ns]
                  ",200,-1.*rdet_size,rdet_size,"x [mm]",
                  ndir);
74          if ( fabs(big_mol->ion[i]->raw.data.x)<10. )
```

```
75                  Hist->fill(hoff+hmax*i+15,"fish_filet_y",
                        big_mol->ion[i]->raw.data.tof,big_mol->
                        ion[i]->raw.data.y,1.,"y-fish filet",rg
                        ->get_bins(rgti+i,TOF),rg->get_from(rgti
                        +i,TOF),rg->get_to(rgti+i,TOF),"tof [ns]
                        ",200,-1.*rdet_size,rdet_size,"y [mm]",
                        ndir);
76
77              if(i<(big_mol->number_of_ions-0.01)/2)
78                  rtof_sum1 += big_mol->ion[i]->raw.data.tof;
79              else
80                  rtof_sum2 += big_mol->ion[i]->raw.data.tof;
81          }
82
83          // fill standard polyatomic coincidence histograms
84          strcpy(ndir,rootdir);
85          sprintf(tdir,"/polyatomic");
86          strcat(ndir,tdir);
87          strcpy(tdir,ndir);
88
89          if (cur_reaction->use_ion_matrix == 1) {
90              for (int i=0; i<16; i++) {
91                  for (int j=0; j<16; j++) //goes through
                        each ion species
92                  {
93                      if (big_mol->ion_matrix[i][j] == 1) //
                            if hit tof is within the bounds of
                            the ion species
94                          Hist->fill2(hoff+hmax+20,"PIM",i,j
                                ,1.,"Ion matrix",16,0,16,"Hit
                                number",16,0,16,"ion species",
                                ndir);
95                  }
96              }
97              Hist->fill(hoff+hmax+21,"pzsum_[0]",big_mol->
                    value_to_sort[0],1.,"sum_momentum"
                    ,400,0.,100.,"momentum (a.u.)",ndir);
```

```
98              Hist->fill(hoff+hmax+22,"pzsum_[1]",big_mol->
                    value_to_sort[1],1.,"sum_momentum"
                    ,400,0.,100.,"momentum (a.u.)",ndir);
99          }
100
101         Hist->fill(hoff+hmax+23,"KER",big_mol->KER(),1.,"
                kinetic energy release",rg->get_bins(rgtp,
                P_KINER),rg->get_from(rgtp,P_KINER)/2,rg->get_to
                (rgtp,P_KINER),"KER [eV]",ndir);
102
103         Hist->fill(hoff+hmax+24,"p_sumx_vs_p_sumy_coarse",
                big_mol->mom_cm.x,big_mol->mom_cm.y,1.,"center
                of mass momentum x vs y",5*rg->get_bins(rgtp,
                P_PCMX),5*rg->get_from(rgtp,P_PCMX),5*rg->get_to
                (rgtp,P_PCMX),"p_cmx [a.u.]",5*rg->get_bins(rgtp
                ,P_PCMY),5*rg->get_from(rgtp,P_PCMY),5*rg->
                get_to(rgtp,P_PCMY),"p_cmx [a.u.]",ndir);
104         Hist->fill(hoff+hmax+25,"p_sumx_vs_p_sumz_coarse",
                big_mol->mom_cm.x,big_mol->mom_cm.z,1.,"center
                of mass momentum x vs z",5*rg->get_bins(rgtp,
                P_PCMX),5*rg->get_from(rgtp,P_PCMX),5*rg->get_to
                (rgtp,P_PCMX),"p_cmx [a.u.]",5*rg->get_bins(rgtp
                ,P_PCMZ),5*rg->get_from(rgtp,P_PCMZ),5*rg->
                get_to(rgtp,P_PCMZ),"p_cmz [a.u.]",ndir);
105         Hist->fill(hoff+hmax+26,"p_sumy_vs_p_sumz_coarse",
                big_mol->mom_cm.y,big_mol->mom_cm.z,1.,"center
                of mass momentum y vs z",5*rg->get_bins(rgtp,
                P_PCMY),5*rg->get_from(rgtp,P_PCMY),5*rg->get_to
                (rgtp,P_PCMY),"p_cmy [a.u.]",5*rg->get_bins(rgtp
                ,P_PCMZ),5*rg->get_from(rgtp,P_PCMZ),5*rg->
                get_to(rgtp,P_PCMZ),"p_cmz [a.u.]",ndir);
106         Hist->fill(hoff+hmax+27,"p_sumx_vs_p_sumy",big_mol
            ->mom_cm.x,big_mol->mom_cm.y,1.,"center of mass
            momentum x vs y",rg->get_bins(rgtp,P_PCMX),rg->
            get_from(rgtp,P_PCMX),rg->get_to(rgtp,P_PCMX),"
            p_cmx [a.u.]",rg->get_bins(rgtp,P_PCMY),rg->
            get_from(rgtp,P_PCMY),rg->get_to(rgtp,P_PCMY),"
            p_cmx [a.u.]",ndir);
```

```
107         Hist->fill(hoff+hmax+28,"p_sumx_vs_p_sumz",big_mol
              ->mom_cm.x,big_mol->mom_cm.z,1.,"center of mass
              momentum x vs z",rg->get_bins(rgtp,P_PCMX),rg->
              get_from(rgtp,P_PCMX),rg->get_to(rgtp,P_PCMX),"
              p_cmx [a.u.]",rg->get_bins(rgtp,P_PCMZ),rg->
              get_from(rgtp,P_PCMZ),rg->get_to(rgtp,P_PCMZ),"
              p_cmz [a.u.]",ndir);
108         Hist->fill(hoff+hmax+29,"p_sumy_vs_p_sumz",big_mol
              ->mom_cm.y,big_mol->mom_cm.z,1.,"center of mass
              momentum y vs z",rg->get_bins(rgtp,P_PCMY),rg->
              get_from(rgtp,P_PCMY),rg->get_to(rgtp,P_PCMY),"
              p_cmy [a.u.]",rg->get_bins(rgtp,P_PCMZ),rg->
              get_from(rgtp,P_PCMZ),rg->get_to(rgtp,P_PCMZ),"
              p_cmz [a.u.]",ndir);
109
110         Hist->fill(hoff+hmax+30,"p_sum_magnitude",big_mol->
              mom_cm.Mag(),1.,"p_sum_magnitude",rg->get_bins(
              rgtp,P_PCM),rg->get_from(rgtp,P_PCM),rg->get_to(
              rgtp,P_PCM),"sum momentum [a.u.]",ndir);
111         if (big_mol->number_of_ions > 2) {
112           // Create Dalitz plot with the ions provided by
                the Dalitz array
113           sprintf(x_axis_title,"(|p|_%i - |p|_%i)/sqrt(3)
                ",int(big_mol->ion[cur_reaction->
                Dalitz_array[1]]->raw.m+0.01),int(big_mol->
                ion[cur_reaction->Dalitz_array[2]]->raw.m
                +0.01));
114           sprintf(y_axis_title,"|p|_%i - 1/3",int(big_mol
                ->ion[cur_reaction->Dalitz_array[0]]->raw.m
                +0.01));
```

```
115             Hist->fill(hoff+hmax+32,"Dalitz_plot",(big_mol
                    ->ion[cur_reaction->Dalitz_array[1]]->mom.
                    Mag() - big_mol->ion[cur_reaction->
                    Dalitz_array[2]]->mom.Mag())/(big_mol->
                    momentum_magnitude_sum*sqrt(3.)),big_mol->
                    ion[cur_reaction->Dalitz_array[0]]->mom.Mag
                    ()/big_mol->momentum_magnitude_sum -
                    1./3.,1.,"Dalitz plot for momenta"
                    ,100,-0.5,0.5,x_axis_title,100,-0.5,0.5,
                    y_axis_title,ndir);
116
117             // Create Newton plot with the ions provided by
                     the Newton array
118             Coordinate_System Nframe = Coordinate_System(
                    big_mol->ion[cur_reaction->Newton_array
                    [0]]->mom, big_mol->ion[cur_reaction->
                    Newton_array[1]]->mom);
119             CH_vector NFrame_mom[3];
120             for (int i = 0; i<3; i++)
121             {
122                 NFrame_mom[i] = Nframe.project_vector(
                        big_mol->ion[cur_reaction->Newton_array[
                        i]]->mom);
123             }
124             Hist->fill(hoff+hmax+33,"Newton_plot",
                    NFrame_mom[1].z/big_mol->ion[cur_reaction->
                    Newton_array[0]]->mom.Mag(),NFrame_mom[1].x/
                    big_mol->ion[cur_reaction->Newton_array
                    [0]]->mom.Mag(),1.,"Newton plot"
                    ,80,-2.5,1.5,"pz normalized",120,-3.0,3.0,"
                    py normalized",ndir);
125             Hist->fill(hoff+hmax+33,"Newton_plot",
                    NFrame_mom[2].z/big_mol->ion[cur_reaction->
                    Newton_array[0]]->mom.Mag(),NFrame_mom[2].x/
                    big_mol->ion[cur_reaction->Newton_array
                    [0]]->mom.Mag(),1.,"Newton plot"
                    ,80,-2.5,1.5,"pz normalized",120,-3.0,3.0,"
                    py normalized",ndir);
```

```
126
127             int MFbins = max(rg->get_bins(rgti+cur_reaction
                    ->Newton_array[1],P),rg->get_bins(rgti+
                    cur_reaction->Newton_array[2],P));
128             double MFto = max(rg->get_to(rgti+cur_reaction
                    ->Newton_array[1],P),rg->get_to(rgti+
                    cur_reaction->Newton_array[2],P));
129
130             Hist->fill(hoff+hmax+34,"Ion_Molframe",
                    NFrame_mom[1].z,NFrame_mom[1].x,1.,"Ions
                    Molframe",MFbins,-240.0,240,"pz [a.u.]",
                    MFbins,-MFto,MFto,"py [a.u.]",ndir);
131             Hist->fill(hoff+hmax+34,"Ion_Molframe",
                    NFrame_mom[2].z,NFrame_mom[2].x,1.,"Ions
                    Molframe",MFbins,-240.0,240,"pz [a.u.]",
                    MFbins,-MFto,MFto,"py [a.u.]",ndir);
132
133             Hist->fill(hoff+hmax+35,"Ion_Molframe_vs_p",
                    NFrame_mom[1].z,NFrame_mom[1].x,NFrame_mom
                    [0].Mag(),1.,"Ions Molframe",MFbins,-MFto,
                    MFto,"pz [a.u.]",MFbins,-MFto,MFto,"py [a.u
                    .]",rg->get_bins(rgti+cur_reaction->
                    Newton_array[0],P),rg->get_from(rgti+
                    cur_reaction->Newton_array[0],P),rg->get_to(
                    rgti+cur_reaction->Newton_array[0],P),"|
                    p_Ion0| [a.u.]",ndir);
134             Hist->fill(hoff+hmax+35,"Ion_Molframe_vs_p",
                    NFrame_mom[2].z,NFrame_mom[2].x,NFrame_mom
                    [0].Mag(),1.,"Ions Molframe",MFbins,-MFto,
                    MFto,"pz [a.u.]",MFbins,-MFto,MFto,"py [a.u
                    .]",rg->get_bins(rgti+cur_reaction->
                    Newton_array[0],P),rg->get_from(rgti+
                    cur_reaction->Newton_array[0],P),rg->get_to(
                    rgti+cur_reaction->Newton_array[0],P),"|
                    p_Ion0| [a.u.]",ndir);
135
```

```
136             double BondAngle = big_mol->ion[cur_reaction->
                    Newton_array[0]]->mom.Angle_deg(big_mol->ion
                    [cur_reaction->Newton_array[1]]->mom);
137             Hist->fill(hoff+hmax+36,"Bond_angle_vs_KER",
                    BondAngle, big_mol->KER(),1.,""
                    ,72,0.0,180.0,"theta [deg]",rg->get_bins(
                    rgtp,P_KINER),rg->get_from(rgtp,P_KINER),rg
                    ->get_to(rgtp,P_KINER),"KER [eV]",ndir);
138             Hist->fill(hoff+hmax+37,"cos(Bond_angle)_vs_KER
                    ",cos(BondAngle/180.*PI), big_mol->KER()
                    ,1.0,"",36,-1.0,1.0,"cos(theta)",rg->
                    get_bins(rgtp,P_KINER),rg->get_from(rgtp,
                    P_KINER),rg->get_to(rgtp,P_KINER),"KER [eV]"
                    ,ndir);
139
140             Coordinate_System mf = Coordinate_System(
                    big_mol->ion[0]->mom.Norm() + big_mol->ion
                    [1]->mom.Norm(), big_mol->ion[0]->mom.Norm()
                     - big_mol->ion[1]->mom.Norm());
141             CH_vector i1_MF;
142             i1_MF = mf.project_vector(big_mol->ion[0]->mom)
                    ;
143             CH_vector i2_MF;
144             i2_MF = mf.project_vector(big_mol->ion[1]->mom)
                    ;
145             Hist->fill(hoff+hmax+38,"Ion_3D-Molframe",i1_MF
                    .Phi_deg(),i1_MF.Cos_Theta(),1.,"Molecular
                    frame angular distribution (Ion Position)"
                    ,36,-180.,180.,"Phi",24,-1.0,1.0,"cos(theta)
                    ",ndir);
146             Hist->fill(hoff+hmax+38,"Ion_3D-Molframe",i2_MF
                    .Phi_deg(),i2_MF.Cos_Theta(),1.,"Molecular
                    frame angular distribution (Ion Position)"
                    ,36,-180.,180.,"Phi",24,-1.0,1.0,"cos(theta)
                    ",ndir);
147
148         // ion/electron coincidences
149         strcpy(alldir,rootdir);
```

```
150         strcat(alldir,"/polyatomic_coincidence/all_hits");
151
152         for(int i=0;i<(int)ehit;i++) {
153             strcpy(ndir,rootdir);
154             sprintf(tdir,"/polyatomic_coincidence/elec_hit_
                  %i",i);
155             strcat(ndir,tdir);
156 //          strcpy(tdir,ndir);
157
158             if(e[i]->valid) {
159                 Hist->fill(hoff+hmax*i+40,"
                      KER_vs_electron_energy",big_mol->KER(),e
                      [i]->energy(),1.,"kinetic energy release
                       vs electron energy",rg->get_bins(rgtp,
                      P_KINER),rg->get_from(rgtp,P_KINER),rg->
                      get_to(rgtp,P_KINER),"KER [eV]",rg->
                      get_bins(rgte+i,ENERGY),rg->get_from(
                      rgte+i,ENERGY),rg->get_to(rgte+i,ENERGY)
                      ,"electron energy [eV]",ndir);
160
161                 Coordinate_System mf = Coordinate_System(
                      big_mol->ion[0]->mom, big_mol->ion[1]->
                      mom);
162                 CH_vector e_MF;
163                 e_MF = mf.project_vector(e[i]->mom);
164                 Hist->fill(hoff+hmax*i+41,"MFPAD3D",e_MF.
                      Phi_deg(),e_MF.Cos_Theta(),1.,"molecular
                       frame angular distribution"
                      ,36,-180.,180.,"Phi",24,-1.0,1.0,"cos(
                      theta)",ndir);
165             }
166
167             // Merge all electrons in one plot
168             if(e[i]->valid) {
```

```
169                     Hist->fill(hoff+hmax+42,"
                            KER_vs_electron_energy",big_mol->KER(),e
                            [i]->energy(),1.,"kinetic energy release
                             vs electron energy",rg->get_bins(rgtp,
                            P_KINER),rg->get_from(rgtp,P_KINER),rg->
                            get_to(rgtp,P_KINER),"KER [eV]",rg->
                            get_bins(rgte+i,ENERGY),rg->get_from(
                            rgte+i,ENERGY),rg->get_to(rgte+i,ENERGY)
                            ,"electron energy [eV]",alldir);
170                 }
171             }
172
173         }
174 }
```